

VIBRATION ASSISTED DRILLING OF ALUMINUM 6061-T6

VIBRATION ASSISTED DRILLING OF ALUMINUM 6061-T6

BY

SIMON, SHUET FUNG, CHANG

A Thesis

Submitted to the School of Graduate Studies

in Partial Fulfillment of the Requirements

For the Degree

Doctor of Philosophy

McMaster University

March 2010

DOCTOR OF PHILOSOPHY

(Mechanical Engineering)

McMaster University

Hamilton, Ontario

TITLE: Vibration Assisted Drilling of Aluminum 6061-T6

AUTHOR: Simon, Shuet Fung, Chang, M.A.Sc. (Mech. Eng)

McMaster University

SUPERVISOR: Dr. G. M. Bone

NUMBER OF PAGES: xvii, 126

## ABSTRACT

Burr formation is a frequent problem in metal cutting. Burrs, which are defined as undesired projections of material resulting from plastic deformation, affect the precision of machined components and can negatively affect the assembly process. One common burr is the exit burr that forms when drilling ductile materials such as aluminum alloy. Deburring, the process of removing burrs, can account for up to 30% of the total production cost. If the burr size can be reduced, the deburring effort can also be reduced or even eliminated, resulting in an improvement in productivity and an increase in profit.

There are different methods to reduce burr formation in drilling. One method is known as vibration assisted drilling. Vibration assisted drilling has been reported as an effective method to reduce burr height without reducing the material removal rate or permanently altering the mechanical behavior of the workpiece material. Other reported benefits of vibration assisted drilling include improvement of tool life and better machined surface quality. However, it has been reported that poor choice of vibration conditions (frequency and amplitude) can increase burr height. No accurate analytical model exists in the current literature that can predict the exit burr height for vibration assisted drilling. To predict exit burr height, a model capable of predicting thrust force accurately is important because higher thrust force produces larger exit burr. Clearly there is a need to develop these models.

This thesis presents the development of analytical models for predicting thrust force and exit burr height for vibration assisted drilling of aluminum 6061-T6. The

developed models incorporate all significant characteristics of vibration assisted drilling to achieve accurate predictions. Drilling experiments were performed over a range of cutting and vibration conditions. The experimental results demonstrate that the developed thrust force model improves the accuracy by up to 45% in comparison to the existing vibration assisted drilling models. The developed burr height model accurately predicts the exit burr height for vibration assisted drilling, with an averaged deviation of 10% from the experimental results. The developed models are also applicable to conventional drilling. Comparing with the existing drilling models, the new models improve the accuracy of thrust force and burr height predictions by 6 and 36% respectively. A fast analytical method has also been developed that predicts the favourable vibration conditions that minimize burr height. The predictions obtained using this method are consistent with the experimental results. Drilling experiments for combined frequency vibration assisted drilling were also performed over a range of vibration conditions. The experimental results demonstrate that combining two different favourable vibration conditions together produces greater mean thrust force reduction than using a single frequency vibration assistance.

## ACKNOWLEDGEMENTS

Thank God my Lord for His guidance and providence throughout these years.

I would like to express my gratitude to my supervisor Dr. G. Bone for his grateful guidance and support throughout the duration of this research. His valuable advices and support contributed significantly to the success of this work.

I would also like to express my appreciations to Dr. Elbestawi for his support; to Dr. Veldhuis and Dr. Swartz for their guidance and suggestions in my research directions; to Dr. Koshy and Dr. Eugene for their assistances in metal cutting theories.

My appreciations are also extended to Warren Renold and Jim McLaren, who had provided tremendous support and guidance in operating and setting up the machines and performing experiments.

I wish to thank my parents, who have given me tremendous support throughout the duration of this research. Finally, special thanks to all of my colleagues, who have always been supportive and encouraging.

## TABLE OF CONTENTS

<b>CHAPTER 1 - INTRODUCTION.....</b>	<b>1</b>
1.1    INTRODUCTION .....	1
<b>CHAPTER 2 - LITERATURE REVIEW .....</b>	<b>7</b>
2.1    INTRODUCTION .....	7
2.2    DRILLING PROCESS MODELING .....	7
2.3    DRILLING BURR FORMATION .....	14
2.4    BURR MODELING IN DRILLING .....	17
2.5    VIBRATION ASSISTED MACHINING .....	19
2.5.1    LFVA MACHINING.....	20
2.5.2    HFVA MACHINING .....	22
2.5.3    CFVA MACHINING.....	25
2.5.4    TWO DEGREE VIBRATION ASSISTED MACHINING.....	26
2.5.5    VAD MODEL.....	28
2.6    CONCLUSIONS.....	32
<b>CHAPTER 3 - THRUST FORCE MODELING FOR VAD .....</b>	<b>36</b>
3.1    INTRODUCTION .....	36
3.2    THRUST FORCE MODEL FOR CONVENTIONAL DRILLING.....	36
3.2.1    INTRODUCTION .....	36
3.2.2    CUTTING MODEL FOR THE CUTTING LIPS OF A DRILL.....	39
3.3    THRUST FORCE MODELING FOR VAD .....	45

3.3.1	EFFECTIVE UNCUT CHIP THICKNESS AND CUTTING ANGLES FOR VAD .....	45
3.3.2	PLOWING FORCE ESTIMATION.....	49
3.3.3	STRAIN RATE-DEPENDENT SHEAR STRENGTH MODEL.....	55
3.3.4	TOTAL THRUST FORCE FOR VAD.....	56
3.4	CONCLUSIONS.....	59
<b>CHAPTER 4 - BURR HEIGHT MODELING FOR VAD .....</b>		<b>61</b>
4.1	INTRODUCTION .....	61
4.2	EXIT BURR HEIGHT MODEL FOR VAD.....	62
4.2.1	EXIT BURR IN DRILLING .....	62
4.2.2	DETERMINING THE CRITICAL MATERIAL THICKNESS USING KIM AND DORNFELD'S MODEL.....	64
4.2.3	PROPOSED BURR HEIGHT MODEL .....	74
4.3	PREDICTING THE FAVOURABLE VIBRATION FREQUENCY .....	76
4.4	CONCLUSIONS.....	81
<b>CHAPTER 5 EXPERIMENTAL STUDY FOR VAD.....</b>		<b>83</b>
5.1	INTRODUCTION .....	83
5.2	EXPERIMENTAL SETUP.....	83
5.3	MODEL CALIBRATION.....	89
5.4	THRUST FORCE MODEL PREDICTION AND EXPERIMENTAL RESULTS .....	92

5.5	BURR HEIGHT MODEL PREDICTION AND EXPERIMENTAL RESULTS	97
5.6	PREDICTING THE FAVOURABLE VIBRATION FREQUENCY	102
5.7	CONCLUSION	103
<b>CHAPTER 6 - COMBINED FREQUENCY VIBRATION ASSISTED DRILLING</b>		<b>105</b>
6.1	INTRODUCTION	105
6.2	CFVAD EXPERIMENTS	105
6.3	CONCLUSIONS	109
<b>CHAPTER 7- CONCLUSIONS AND RECOMMENDATIONS</b>		<b>111</b>
7.1	INTRODUCTION	111
7.2	CONCLUSIONS	112
7.3	RECOMMENDATIONS FOR FUTURE WORK	114
<b>REFERENCE</b>		<b>115</b>
<b>APPENDIX A</b>		<b>124</b>

## LIST OF FIGURES

Figure 1.1.1: Definition of different burr type.....	3
Figure 1.1.2: Exit burr in drilling.....	4
Figure 2.2.1: Basic geometry of a drill tip.....	8
Figure 2.2.2: Tool wedge model.....	9
Figure 2.2.3: Cutting geometry on the cutting lip reported in Elhachimi <i>et al.</i> [13].....	12
Figure 2.2.4: Cutting geometry on the chisel edge reported in Elhachimi <i>et al.</i> [13].....	13
Figure 2.3.1: Negative shear angle and negative shear plane.....	15
Figure 2.3.2: Burr fractured.....	15
Figure 2.3.3: Different types of burrs formed in drilling.....	16
Figure 2.3.4: Burr formation in drilling.....	17
Figure 2.4.1: Finite element model of drilling burr formation (Dornfeld [18]).....	18
Figure 2.5.1: Principal of elliptical vibration cutting (Moriwaki and Shamoto [37]).....	27
Figure 3.2.1. Schematic of the tool wedge model.....	37
Figure 3.2.2. Cutting regions of a drill.....	38
Figure 3.2.3. Cutting lips of a drill divided into elements (only one of the two lips is shown).....	39
Figure 3.2.4. Cutting geometry of a particular element on a cutting lip.....	40
Figure 3.2.5. End view of a drill showing its element on one of the cutting lips.....	41
Figure 3.3.1. Rotational angle of a cutting lip of a drill.....	47
Figure 3.3.2. Geometry involved in determining the axial uncut chip thickness.....	48
Figure 3.3.3. Example of determining $z_{\max}(\theta)$ .....	49

Figure 3.3.4. Formation of plowing force for an element in VAD.....	51
Figure 3.3.5. Geometry of drill elements and segments. ....	53
Figure 3.3.6. Geometry of the $k^{th}$ segment.....	54
Figure 3.3.7. Schematic of cutting forces during downward (a) and upward (b) strokes of the tool. ....	58
Figure 4.2.1. Formation of an exit burr as the tool approaches the exit surface.....	63
Figure 4.2.2. Burr formation mechanism.....	68
Figure 4.2.3. Typical measurement of drilling thrust force (taken from [22]). ....	69
Figure 4.2.4. Deformation of material under the drill.....	70
Figure 4.2.5. Final burr formation. ....	73
Figure 4.3.1. Comparison between actual and approximated relationship between $\gamma_{nd}$ and $\eta_d$ .....	77
Figure 4.3.2: Example of an approximated axial displacement of the drill.....	78
Figure 5.2.1. Vibration workpiece holder.....	84
Figure 5.2.2. Polarity switching drive circuit. ....	85
Figure 5.2.3. Measurement of burr height. ....	87
Figure 5.2.4. Some examples of the machined workpiece. ....	88
Figure 5.3.1. Mean thrust force vs vibration frequency for tests 1–6 before calibration..	90
Figure 5.3.2. Mean thrust force vs vibration frequency for tests 1–6 after calibration with Johnson-Cook model. ....	91
Figure 5.3.3. Mean thrust force vs vibration frequency for tests 1– 6 for force model calibrated with Johnson-Cook model and indentation force.....	92

Figure 5.4.1. Simulations and experimental thrust force results for tests 7–12.....	94
Figure 5.4.2. Simulations and experimental thrust force results for tests 13–18.....	94
Figure 5.4.3. Simulations and experimental thrust force results for tests 19–24.....	95
Figure 5.4.4. Different thrust force simulation results for tests 7–12.....	96
Figure 5.4.5. Different thrust force simulation results for tests 13–18.....	96
Figure 5.4.6. Different thrust force simulation results for tests 19–24.....	97
Figure 5.5.1. Simulations and experimental burr height results for tests 7–12.....	99
Figure 5.5.2. Simulations and experimental burr height results for tests 13–18.....	99
Figure 5.5.3. Simulations and experimental burr height results for tests 19–24.....	100
Figure 5.5.4. Different burr height simulation results of tests 7–12.....	101
Figure 5.5.5. Different burr height simulation results of tests 13–18.....	101
Figure 5.5.6. Different burr height simulation results of tests 19–24.....	102
Figure 6.2.1: Mean thrust force vs. high frequency vibration component for 45 CFVAD experiments.....	107
Figure 6.2.2: Burr height vs. high frequency vibration component for 45 CFVAD experiments.....	109

## LIST OF TABLES

Table 5.2.1. Mechanical specifications of the VAD hardware.....	84
Table 5.2.2. Cutting and vibration conditions of the performed experiments.....	87
Table 5.3.1. Mean thrust force measurement for tests 1–6.....	89
Table 5.3.2. Model prediction of the mean strain and strain rate for tests 1–6.....	91
Table 5.4.1. Comparison between model prediction and experimental measurements....	93
Table 5.5.1. Comparison between model prediction and experimental measurements....	97
Table 5.6.1. Prediction of $\bar{\eta}_d^*$ and $f^*$ .....	103
Table 6.2.1: CFVAD experimental results for the chosen vibration conditions.....	106

## LIST OF SYMBOLS

$A$	Vibration amplitude (mm)
$D$	Drill diameter (mm)
$E$	Elastic modulus (Pa)
$f$	Vibration frequency (Hz)
$f_{sp}$	Specific plowing force (N)
$f^*$	Favourable vibration frequency (Hz)
$F$	Feed (mm/rev)
$F_C, F_P$	Principal cutting forces (N)
$\bar{F}_{th}$	Mean thrust force (N)
$\bar{F}_{th}^+$	Average positive portion of thrust force (N)
$F_{l,T}, F_{l,C}$	Principal cutting forces on each cutting lip (N)
$F_{pt}, F_{px}$	Principal plowing forces (N)
$H$	Burr height (mm)
$h$	Uncut chip thickness (mm)
$h_c$	Chip thickness (mm)
$h_f$	Axial uncut chip thickness for VAD (mm)
$h_l$	Effective uncut chip thickness (mm)
$M$	Number of elements on each cutting lip
$M_b$	Required bending moment (Nm)

$n$	Spindle speed (rev/s)
$N$	Total number of segments
$p$	Half point angle
$P_{Total}$	Total thrust force (N)
$r_i$	Distance between element and drill centre (mm)
$S^*, S$	Cross-sectional area before and after unloading (mm <sup>2</sup> )
$t$	Time (s)
$t_c$	Critical material thickness (mm)
$T$	Vibration period (s)
$T_k$	Axial location of segment $k$ (mm)
$V$	Volume (mm <sup>3</sup> )
$V_{axial}$	Axial velocity of the drill (mm/s)
$\bar{V}$	Magnitude of cutting velocity (mm/s)
$w$	Width of cut (mm)
$W$	Web thickness (mm)
$W_t$	Work done on the workpiece per vibration cycle (N.m)
$W_{t,i}$	Work done per vibration cycle by the $i^{\text{th}}$ element (N.m)
$\bar{W}_{t,i}$	Normalized work done (N.m/mm)
$z(t)$	Axial displacement of the drill (mm)
$\dot{z}(t)$	Axial velocity of the drill (mm/s)

$z(\theta)$	Axial displacement of the drill with respect to rotational angle (mm)
$z_{MAX}(\theta)$	Maximum depth of material under the drill (mm)
$\bar{z}_0$	Resultant axial drill displacement after one vibration cycle (mm)
$\beta_0$	Helix angle of the drill
$\gamma$	Rake angle
$\gamma_{nd}$	Dynamic rake angle
$\Delta d_k$	Plowing depth of segment $k$ (mm)
$\Delta l_i$	Length of each segment (mm)
$\Delta P_i$	Thrust force of the $i^{\text{th}}$ element (N)
$\Delta V_i$	Displaced volume ( $\text{mm}^3$ )
$\Delta w$	Width of each element (mm)
$\Delta W_b$	Work required for bending (N.m)
$\Delta W_d$	Work required for plastic deformation (N.m)
$\Delta W_e$	Work required for elongation (N.m)
$\Delta W_t$	Work done by cutting force in feed direction (N.m)
$\Delta W_{Total}$	Total work done by thrust force and deformation (N.m)
$\Delta \theta$	Change in angle of the deforming disk
$\varepsilon$	Strain
$\dot{\varepsilon}$	Strain rate

$\varepsilon_p, \varepsilon_f$	Plastic and fracture strain
$\varepsilon_T, \varepsilon_e$	Total and elastic strain
$\varepsilon_{ab}, \varepsilon_{ab}(r)$	Strain along $ab$
$\eta_d$	Dynamic feed angle
$\bar{\eta}_d^*$	$\eta_d$ that minimizes $\bar{W}_{t,i}$
$\theta$	Rotational angle
$\lambda$	Friction Angle
$\lambda_{nd}$	Dynamic friction angle
$\mu_c$	Mean coefficient of friction of tool-chip interface
$\nu$	Poisson ratio
$\nu_s$	Shear thickness (mm)
$\xi$	Flank clearance angle
$\sigma_Y$	Yield strength (MPa)
$\tau$	Shear strength (MPa)
$\tau_i$	Shear strength (strain-rate dependent) (MPa)
$\phi$	Shear angle
$\phi_{nd}$	Dynamic shear angle
%R.A.	% reduction of area

## **LIST OF ACRONYMS**

CFVAD	Combined Frequency Vibration Assisted Drilling
HFVA	High Frequency Vibration Assisted
HFVAD	High Frequency Vibration Assisted Drilling
LFVA	Low Frequency Vibration Assisted
LFVAD	Low Frequency Vibration Assisted Drilling
VAD	Vibration Assisted Drilling

## CHAPTER 1

### 1.1 INTRODUCTION

Burr formation in drilling has always been a challenge to industry. Burrs are commonly defined as undesired projections of materials resulting from plastic deformation as the cutting tool approaches an edge. One example is a roll over burr. As the tool approaches the exit edge of the workpiece, because the remaining material in front of the tool along the cutting path is not rigid enough to withstand the cutting force, plastic deformation occurs and a burr forms. In other words, burr formation begins when the energy required for the tool to cut the material is more than that needed for the tool to plastically deform the workpiece. The allowable burr sizes vary with different applications. As the required precision and surface quality of components increase, the associated post-processing effort such as deburring also increases. It has been reported that deburring typically accounts for up to 30% of total production cost [1]. This number includes automated deburring and manual deburring. In some applications, deburring can be very difficult, especially in difficult to access areas, such as the inner surface of a hollow tube. If the machining process can be altered to reduce burr size, the associated deburring effort can be reduced or even eliminated.

In order to reduce burr size, it is important to understand the mechanism of burr formation. In general, there are five different types of burrs: Poisson burr, entrance burr,

rollover burr, tear burr, and cut-off burr (also known as fracture burr). A Poisson burr results from the plastic deformation that occurs when a material is being compressed, as shown in Figure 1.1.1(a). This type of burr is commonly found in turning, where the tool is pressed against the work material in the feed direction. An entrance burr may form when the tool first engages the work material and plastically deforms it (Figure 1.1.1(b)). A rollover burr occurs at the edge or exit surface of the material, where the material is being plastically deformed instead of being sheared (Figure 1.1.1(c)). When a material is being torn instead of being sheared, plastic deformation occurs in the tearing zone, resulting in tear burr. A cut-off burr results from fracturing of material instead of shearing. Note that this type of burr is not the result of plastic deformation. This thesis is concerned with drilling burr formation on the exit surface of the work material (termed an “exit burr”, see Figure 1.1.2). This type of burr is the combination of a rollover burr and a tear burr, with the rollover burr being dominant. Details about exit burr formation in drilling will be discussed in chapter 2.

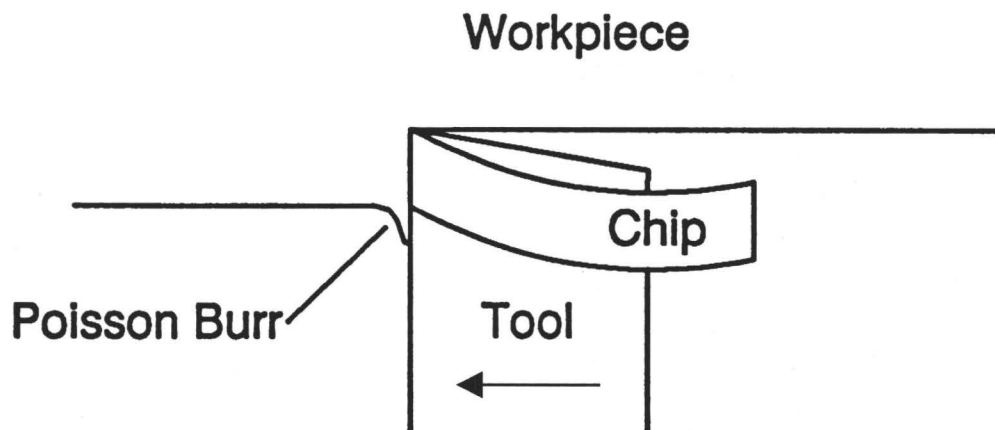


Figure 1.1.1 Burr types. (a): Poisson burr.

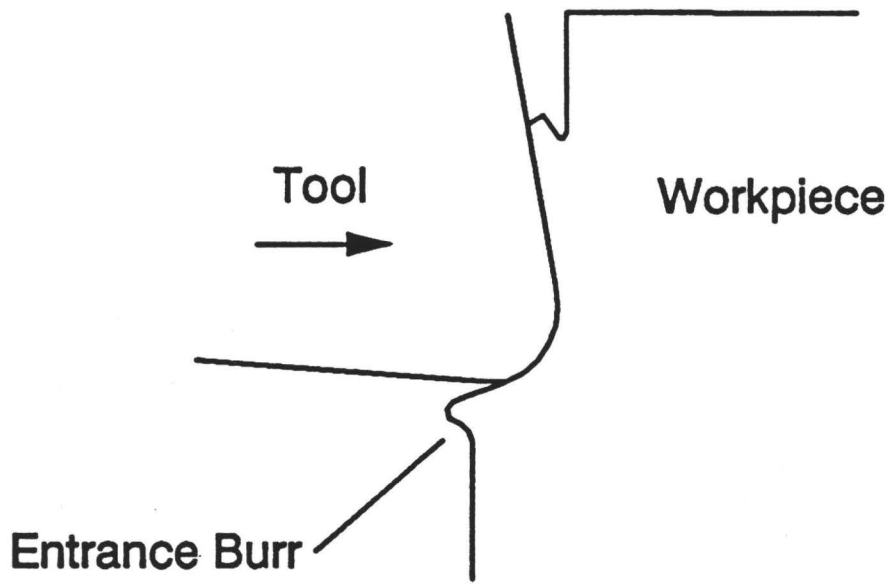


Figure 1.1.1 (b): Entrance burr.

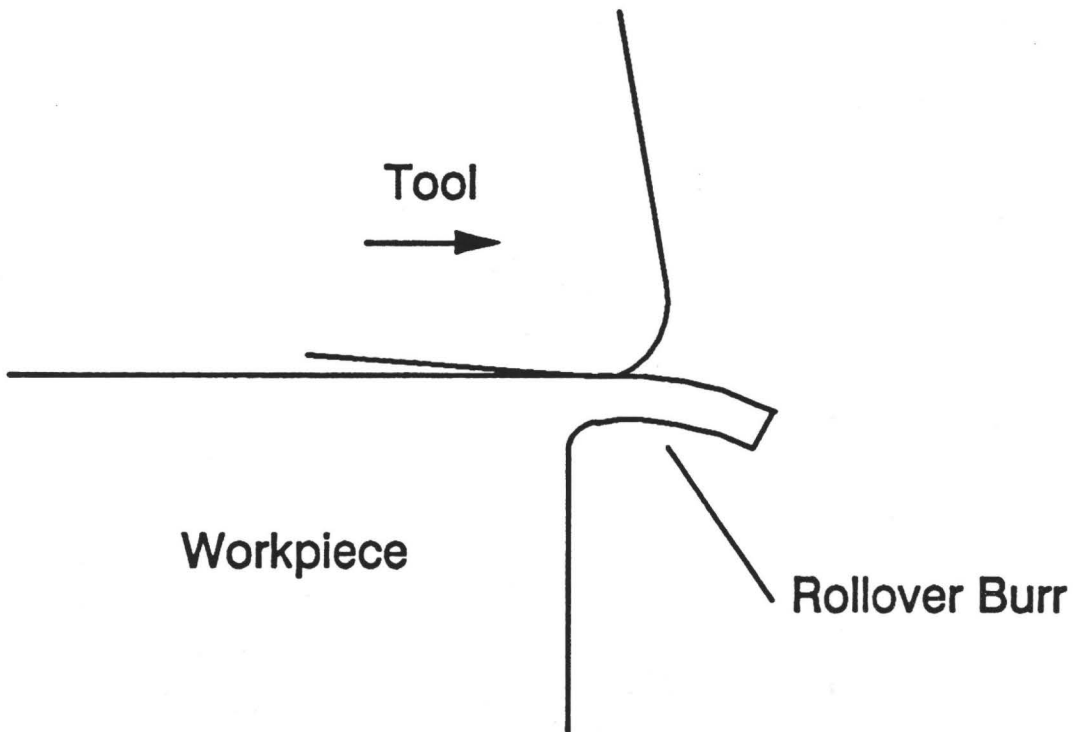
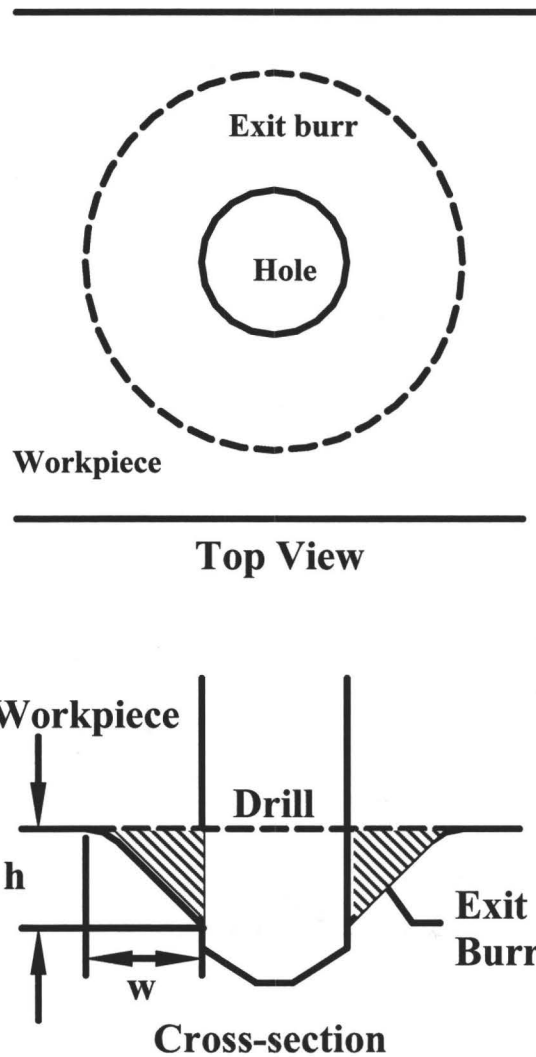


Figure 1.1.1 (c): Rollover burr.



**Figure 1.1.2: Exit burr in drilling.**

There are different methods to reduce exit burr size in drilling. These include reducing the drill feed when the tool approaches the exit surface of the work material, altering the drill geometry, using suitable coolant and lubricant, using suitable tool coating, and using a backup material on the exit surface. However, reducing drill feed means reducing the material removal rate and is thus not desirable. Altering drill geometry often increases production cost because special geometry drills are not

commonly available. Using coolant and lubricant can reduce burr size only to a certain extent. It is also not environmentally friendly, and the disposal cost increases the production cost. Using backup material may not be practical in many applications.

Another known burr reduction method is laser assisted machining, where materials are pre-heated using a laser [2]. This method permanently alters the physical properties of the work materials, and is difficult to apply in deep hole drilling.

A recent and promising method is known as vibration assisted drilling (VAD). The principal of this technique is to apply vibration in the drill feed direction. The vibration frequency and amplitude typically range from 1000 Hz - 200 kHz and 0.002-0.015 mm, respectively [3-6]. VAD has been widely used in machining brittle materials, such as fibre-reinforced plastics [4]. Recent developments have proven that this technique is beneficial in reducing burr formation in metal removal processes. However, the vibration frequency and amplitude plays a significant role for burr reduction. With suitable vibration conditions, burr size can be reduced. However, a poor choice of vibration conditions can result in increased burr size. At the current time no analytical methods exist in the published literature for determining the favourable vibration conditions.

Burr formation begins when the energy required for cutting is larger than that for plastic deformation. The cutting energy is proportional to cutting force, and therefore to predict burr formation predicting cutting force accurately is important. Analytical models predicting cutting forces are widely established for conventional drilling, but not for VAD. There have been various attempts to predict cutting forces for VAD by analyzing

the instantaneous uncut chip thickness. These will be reviewed in Chapter 2. However, variation of instantaneous uncut chip thickness is only one of the many characteristics of VAD. Therefore, there is a need for a more comprehensive cutting force model for VAD.

This thesis concerns thrust force and burr height prediction for VAD of aluminum 6061-T6. This material and similar alloys are widely used for construction of aircraft structures, where many holes need to be drilled. Reducing the deburring effort can reduce total production cost, and therefore it is important to have an accurate burr height prediction model. Theoretical and experimental studies of various cutting conditions and vibration frequencies will be presented. The vibrations were generated by a previously developed workpiece holder at constant vibration amplitude of 0.002mm. In chapter 2, a review of the current state of related research is presented. Chapter 3 presents the theoretical analysis and model development of drilling thrust force prediction of VAD. Chapter 4 presents the theoretical analysis and model development of an exit burr height model, and a simplified analytical model predicting the optimal vibration conditions. Chapter 5 presents the experimental procedure and results, followed by comparison between theoretical model predictions and experimental results for thrust force and burr height. In Chapter 6, experimental studies of combined frequency vibration assisted drill (CFVAD) will be presented. Conclusions and suggestions for future work are given in chapter 7.

## **CHAPTER 2**

### **LITERATURE REVIEW**

#### **2.1 INTRODUCTION**

In this chapter the literature related to drilling burr formation and VAD is reviewed. This has been broken down into four areas: drilling force modeling, drilling burr formation, exit burr modeling for drilling, and vibration assisted machining.

#### **2.2 DRILLING FORCE MODELING**

A reliable thrust force model for drilling can be used to study and analyze different drilling conditions so that a specific condition that minimizes thrust force and burr size can be selected. They can also be used with a burr formation model to predict burr size in order to help plan the deburring operation. Models predicting thrust force in drilling are well developed, and the models with significant contribution to this area will be reviewed in this section.

Drilling is often modeled as a combination of orthogonal cutting and indentation along the chisel edge, and oblique cutting along the cutting edge, usually known as the lip, as shown in Figure 2.2.1 (Altintas, [7]).

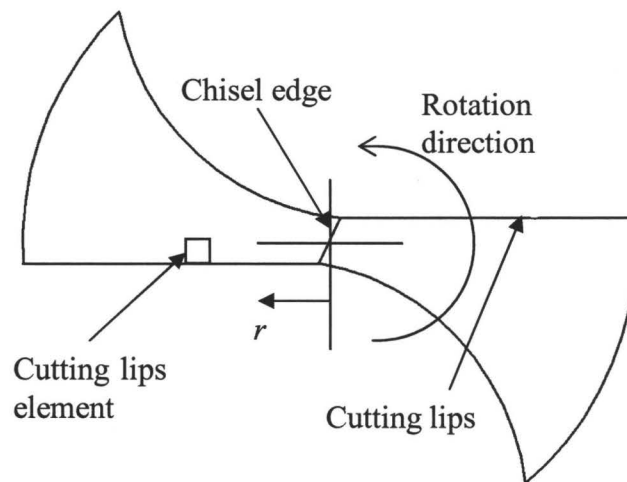


**Figure 2.2.1: Basic geometry of a drill tip.**

In contrast to other cutting processes, drilling does not have a fixed set of parameters, such as rake angle. Therefore, the cutting edges are usually broken down into elements for detailed analysis, although approximations, such as using average rake angle, are sometimes acceptable. Each element is modeled by a tool wedge model [8], which is commonly used in metal removal analysis, as shown in Figure 2.2.2. In this model, material in front of the tool is being removed by a chip formation mechanism. As the tool advances, material is being sheared along the primary and secondary shear zone and forms chips, which are separated from the workpiece material. The primary shear zone is commonly assumed to be a plane and therefore is referred to the primary shear plane. The angle between the primary shear plane and the cutting velocity is known as the shear angle,  $\phi$ . The notations  $t_1$ ,  $t_c$ , and  $\gamma$  are the uncut chip thickness, the deformed chip thickness, and the rake angle, respectively.  $\phi$  is conventionally found experimentally. However, empirical equations, which are limited to a set of specific

cutting conditions and drill geometries, are often used in this model because of the difficulties in accurately determining  $\phi$ . The important literature on drilling models will now be discussed.

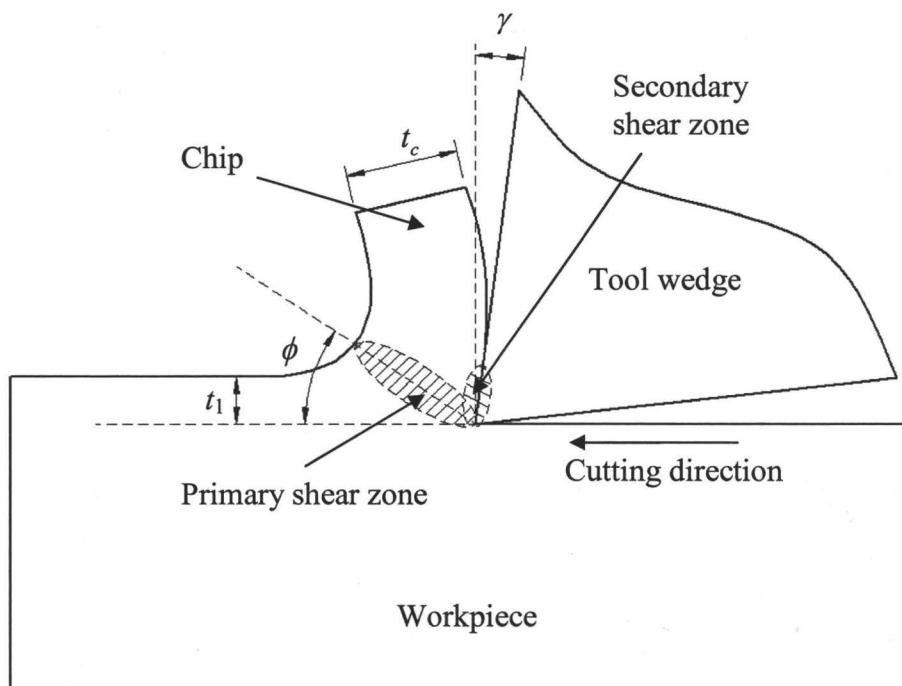


**Figure 2.2.2: Tool wedge model.**

Wiriyacosol and Armarego [9] studied and modeled the thrust and torque in drilling using a cutting mechanics approach. Their model analyzed the geometry of each cutting element of the drill and predicted the principal cutting forces by modeling each individual element using the tool wedge model. The resultant thrust and torque can then be found by summation. However, empirical calibrations are needed to determine the edge forces per unit width of cut, the effective shear strength, and the chip thickness ratio, which are all critical factors in their model. Armarego and Wright [10] later used the

same modeling approach to compare drills with three different flank configurations, and concluded that thrust and torque for drills with different flank configurations can be predicted using their model without modeling the complex drill flank geometry.

Watson [11 & 12] studied the geometry of drills and presented a thrust and torque prediction model for drilling. His model uses conventional oblique cutting theory to determine the principal cutting forces. While no calibration procedure was reported, experimentally calibrating the chip thickness ratio is typically necessary to determine the shear angle. Moreover, the reported experimental results were approximately 65% larger than the predicted values using his model.

Elhachimi *et al.* [13 & 14] presented a detailed study of a theoretical model to predict thrust and torque in high speed drilling using conventional twist drills. Their model thoroughly discussed the cutting mechanics of a drill, and was selected to be summarized in this section. Similar to the previous works, the drill is broken down into two cutting regions, the cutting lip and chisel edge. The chisel edge was further broken down into two regions: indentation region and orthogonal cutting region. The cutting regions on the chisel edge and the cutting lips were broken down into elements. By determining the thrust and torque on each element, the total thrust and torque can be computed. Using their terminology, each element has a length of  $dl$ , located at a radius  $r$  away from the drill axis (Figure 2.2.3). Thrust and torque were calculated using the oblique cutting model.

For the cutting lips, the inclination angle  $i$  and rake angle  $\gamma_n$  at each element can be computed geometrically. The cutting geometry of each element on the cutting lip is shown in Figure 2.2.3. The shearing force of each element can then be computed:

$$dF_s = \frac{k_{AB}t_1}{\sin\phi_n} dl \quad (2.2.1)$$

where  $t_1$  is the depth of cut,  $k_{AB}$  is the empirically determined specific cutting pressure, and  $\phi_n$  is the shear angle at each element. The principal cutting force,  $F_C$ , and its tangential component,  $F_T$ , produced by each element can then be computed by:

$$dF_C = dF_s \frac{\cos(\phi_n - \gamma_n)}{\cos(\phi_n + \lambda_n - \gamma_n)} \quad (2.2.2)$$

$$dF_T = dF_s \frac{\sin(\phi_n - \gamma_n)}{\cos(\phi_n + \lambda_n - \gamma_n)} \quad (2.2.3)$$

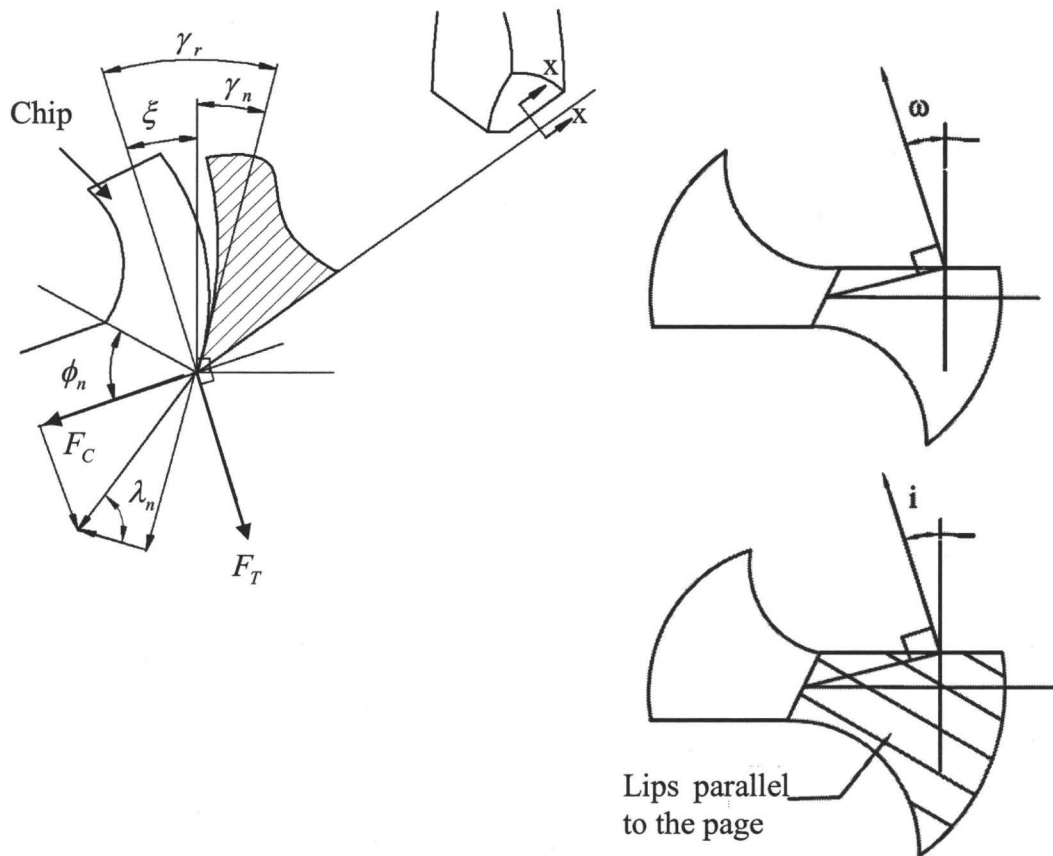


**Figure 2.2.3: Cutting geometry on the cutting lip reported in Elhachimi *et al.* [13].**

For the chisel edge, the region closer to the drill axis where cutting velocity is very close to zero is the indentation region; the outer region is the orthogonal cutting region, and can be modeled by an orthogonal cutting model with a negative rake angle. The model assumed that the magnitude of thrust and torque contributed by the indentation zone is negligible, and modeled only the cutting region of the chisel edge. The cutting region is defined by the outer end of the chisel edge and  $r_a$ , where:

$$r_a = \frac{f \tan p \sin \psi}{2\pi} \quad (2.2.4)$$

where  $f$  is the feed,  $p$  is half of the point angle of the drill, and  $\psi$  is the web angle. Since the dynamic rake angle varies with radius, the chisel edge is divided into differential elements. The dynamic rake angle  $\gamma_d$  at each element can again be computed geometrically, using the aid from Figure 2.2.4.

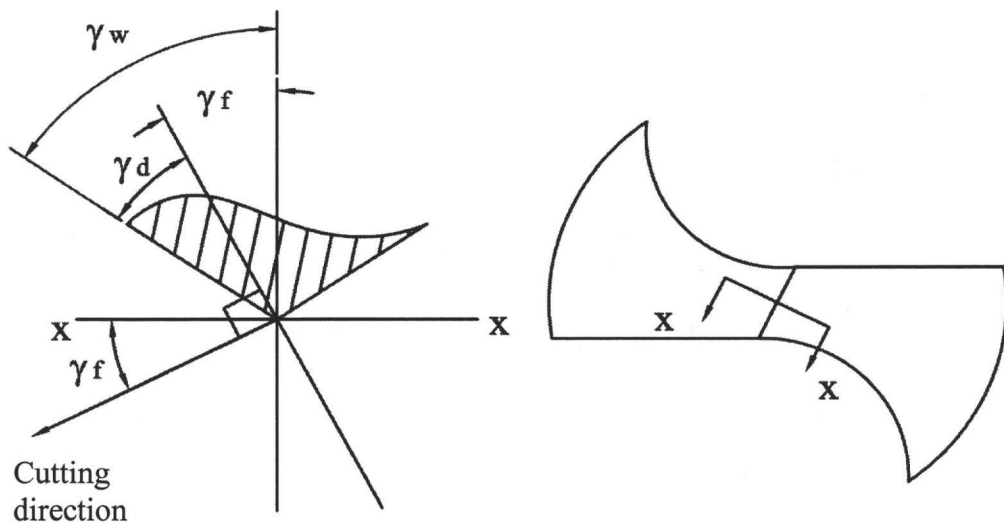


**Figure 2.2.4: Cutting geometry on the chisel edge reported in Elhachimi *et al.* [13].**

The shearing force  $dF_s$  for each element is:

$$dF_s = \frac{k_{AB} t_1}{\sin \phi_n} dr \quad (2.2.5)$$

This differential shear force can then be used to compute the principal forces produced by each element using equations (2.2.2) and (2.2.3). This model however relies on an experimentally determined cutting pressure,  $k_{AB}$ , which is dependent on many different parameters including drill geometries, spindle speed, drill feed, and material properties. Therefore, each value of  $k_{AB}$  is suitable for only a specific range of cutting parameters.

This model also provides little information on how individual cutting parameters can affect the thrust force, making model-based thrust force minimization difficult.

Analytical drilling models predicting thrust forces for conventional drilling are well established. However, due to the dynamic nature of VAD, these models cannot be directly applied to VAD. Several thrust force models for VAD have been published in the literature. They will be reviewed in section 2.5.

## 2.3 DRILLING BURR FORMATION

In order to reduce drilling burr size, understanding the mechanism of burr formation in drilling is important. Gillespie and Blotter [15] studied burr formation in machining. Their work provided the foundation for other studies related to burr formation.

Dornfeld *et al.* [16] investigated the process of rollover burr using plasticine as the working material. Rollover burrs resulted from material being plastically deformed instead of sheared. When the work required to cut the material equals the work required to deform it, the transition from shear to deformation occurs (known as the transition period). The authors divided the burr formation process into three stages: initiation, development, and final burr formation. Initiation occurs when the tool approaches the end of the work material and the transition period begins. A plastic hinge is developed on the exit surface of the work material during this transition period, forming a negative shear plane as shown in Figure 2.3.1. As the tool advances, the material in front of the tool rotates about this hinge until material fracture occurs. After material fracture occurred, the remaining deformed material becomes the burr. Note that if the fracture occurs before

the tool passes the exit surface of the workpiece, a fractured exit surface is formed (see Figure 2.3.2).

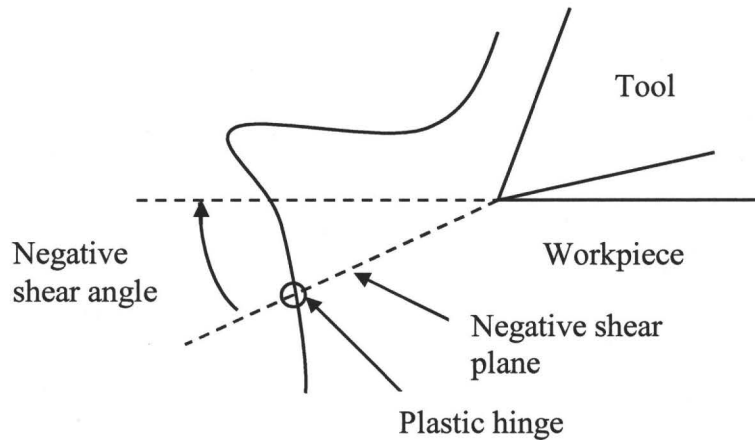


**Figure 2.3.1: Negative shear angle and negative shear plane.**

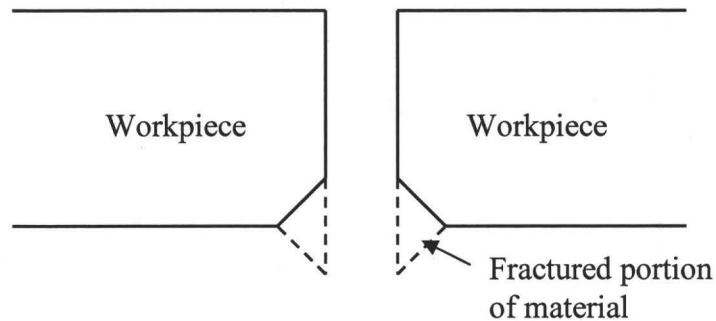


**Figure 2.3.2: Burr fractured.**

Dornfeld *et al.* [17-20] further studied the burr formation mechanism in drilling. The authors defined four types of burrs formed in drilling: normal burr, lean back burr, roll back burr, and roll back burr with wide exit (see Figure 2.3.3). They divided burr formation into four stages as shown in Figure 2.3.4: initiation stage; development stage; final burr formation stage; and burr fracture stage. As the drill approaches the exit surface the material under the chisel edge begin to deform plastically (stage 1: “initiation stage”).

The thickness of the material under the chisel edge where the initiation stage begins depends on the thrust force of the drill, and in general depends on the stress concentration on the work material below the drill. As the drill advances, the deformation zone expands to the edge of the drill (stage 2: “development stage”). At this stage, separation of the deformed materials from the hole perimeter may occur, forming a drill cap. The material around the hole perimeter deforms and forms a burr (stage 3: “final burr formation stage”). During the formation of the burr no chip formation occurs, and the heat generated during the deformation cannot be dissipated through the chips, causing a localized temperature increase at the inner surface of the burr. This increase in temperature causes thermal expansion at the inner surface, forming lean back and roll back burrs. When fracture occurs along the negative shear plane during burr formation, a roll back burr with wide exit is formed (stage 4: “burr fracture stage”).

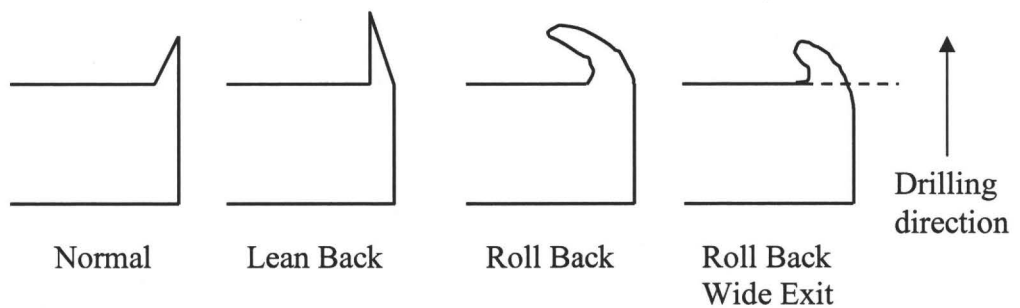


**Figure 2.3.3: Different types of burrs formed in drilling.**

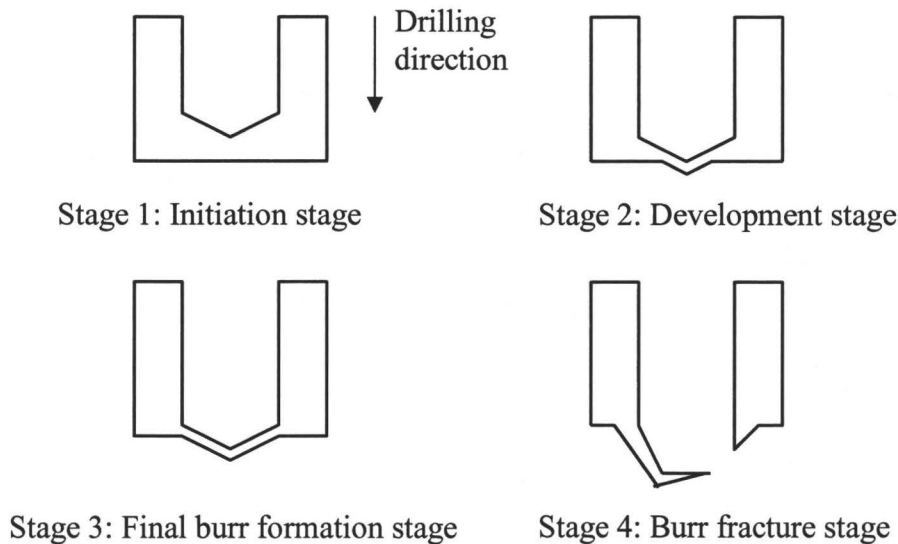


**Figure 2.3.4: Burr formation in drilling.**

Because burr formation begins when the thrust force acting on the workpiece is larger than what the remaining material under the drill can sustain without permanent deformation, if the thrust force on the work materials in drilling can be reduced, the initiation stage of burr formation can be delayed, and the resultant burr size can be reduced.

## 2.4 EXIT BURR MODELING IN DRILLING

If the burr size can be predicted accurately for any given cutting condition, a suitable condition that minimizes burr size can be predicted. Therefore, a model for accurately predicting burr size is important. However, there are not many predictive models in the published literature for burr size in drilling. This section summarizes these models.

Dornfeld *et al.* [18-20] reported several finite element analyses for burr formation in drilling. The simulation results for burr formation in drilling showed qualitative consistency with the theories developed for the burr formation mechanism in orthogonal cutting. Figure 2.4.1 (taken from Dornfeld [18]) shows the development of the negative shear zone, which was discussed in section 2.3 and presented in Figure 2.3.1. They used this model to demonstrate the concept of negative shear zone and pivoting hinge. Burr size prediction was achieved, but no finite element models for VAD have been published.

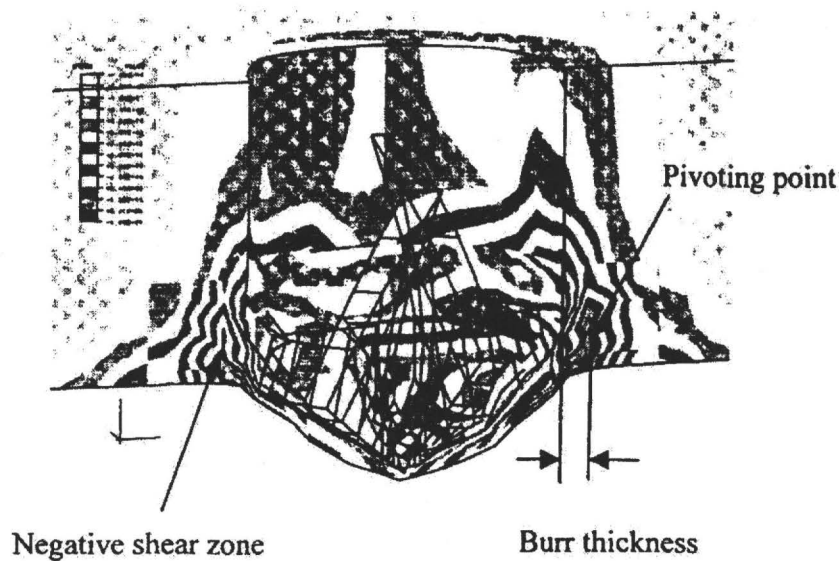


**Figure 2.4.1: Finite element model of drilling burr formation (Dornfeld [18]).**

Lauderbaugh and Mauch [21] presented an analytical burr model. Their model divides the drilling process into two stages. Stage 1 models the process until the drill just penetrated the workpiece material, and stage 2 models the rest of the process. They modeled the material under the drill as a circular plate and computed the deflection and the von Mises stress at the centre of the bottom portion of the plate (the material under

the drill centre). The computation for case 1 begins when the drill starts drilling, and continues until the principal stress level exceeds the ultimate tensile strength of the material, meaning the drill has penetrated the workpiece material. Once this condition occurs, the computation for case 2 begins. With some adjustments to the equations used to account for the change in the shape of the circular plate, the model monitors the von Mises stress along the material around the periphery of the drill and computes the deflection. Again, when the principal stress exceeds the ultimate tensile strength, the material around the periphery of the drill failed. The resultant material forms the burr, and the burr height equals the deflection of materials around the periphery of the drill.

Kim and Dornfeld [22] developed a simple exit burr model for drilling. Neglecting the effects of temperature, strain rate, and tool wear, they assume burr formation begins when the work required to deform the material is less than that required for chip formation. By analyzing these two work components individually, the thickness of material under the drill when burr formation begins can be found. Assuming no cutting occurs once burr formation begins, this thickness can be used to determine the resultant burr size. Because the model developed in this thesis is an extension of Kim and Dornfeld's model, their model will be presented in detail in Chapter 4.

## **2.5 VIBRATION ASSISTED MACHINING**

Vibration assistance has been applied in a variety of ways to machining processes. This section reviews selected publications with the objective of providing an overview of the current state of the art in vibration assisted machining. This section has been divided

into four sub-sections: low frequency vibration assisted (LFVA) machining with vibration frequencies below 1 kHz; high frequency vibration assisted (HFVA) machining with vibration frequencies above 1 kHz; combined frequency vibration assisted (CFVA) machining that is a combination of LFVA and HFVA; and two degree vibration assisted machining, which combines vibrations in two different directions together.

### 2.5.1 LFVA machining

LFVA machining has been proven to be able to reduce cutting forces. Typically, the vibrations are induced in the direction of cutting velocity. For drilling, the vibrations are usually induced in the axial direction. Ramkumar *et al.* [23] experimentally showed LFVA drilling (LFVAD) reduces thrust force and cutting temperature. The material being cut was glass fiber reinforced plastic. Their study also showed that there exists a particular combination of vibration and cutting conditions where the improvement of LFVAD over drilling was the greatest.

Zhang *et al.* [24] presented a parameter variation strategy for LFVAD of fibre reinforced plastic. They broke down the drilling process into three stages. They varied the vibration frequency, vibration amplitude, and feed. The governing factor for the parameter variation was a critical thrust force that was determined by a thrust force model. This critical thrust force represents the largest allowable thrust force before delamination occurs. In the first stage, when the drill initially engages the workpiece, higher cutting rates are possible without delamination of material, and constant parameters that produce a high cutting rate are used. In the second stage, after the drill fully engaged the workpiece and before exiting the workpiece, the parameters are varied to ensure the

drilling thrust force is lower than the critical thrust force. In the third stage, when the drill's chisel edge starts to exit the work piece, constant parameters with low cutting rate were used because the critical thrust force is significantly lower near the exit of the workpiece. Their experimental studies showed by visual comparison that the amount of delamination can be reduced with this technique.

Wang *et al.* [4] experimentally studied low frequency vibration drilling of fibre reinforced plastic. The reported results showed that low frequency vibration drilling can reduce thrust forces, but there exists a favourable vibration condition for a particular cutting condition. The authors correlated the reduction in thrust forces with the changes in chip formation in vibration drilling. The increases in thrust force when frequency or vibration amplitude passes a threshold is explained as increased load on the drill with the strong impact loading between the drill and the bottom surface of the hole.

Li *et al.* [25] developed a multi-stage vibration condition control for vibration drilling of laminated composite materials. The study varies the vibration condition according to the materials being cut, as well as the cutting zones: entrance of the hole, middle of the hole, and exit of the hole, in order to optimize the performance of vibration drilling. Using the reported technique, the average drill point deflection was reduced by over 20%, error of hole diameter by over 80%, and burr height by over 40% when compared with conventional drilling. However, the authors did not compare the reduction of their drilling technique with VAD with constant vibration frequency and amplitude.

### 2.5.2 HFVA machining

HFVA machining has been shown to be able to reduce cutting forces. One of the early attempts was reported by Weber *et al.* [26]. They reported that an ultrasonically vibrated tool can decrease the strength of the material in the shearing area by inducing fracture processes through the tool vibration, especially when machining brittle materials. HFVA turning can also decrease the friction along the contact area between the tool and the work material. Turning experiments were performed with tool vibration induced in the cutting velocity direction, with a frequency of 20 kHz and amplitude 8-12  $\mu\text{m}$ . The workpiece materials used were glass ceramic and alloy steel. They observed the formation of powder chips, because of the fracture induced by the tool vibration, when HFVA machining glass ceramics. They also observed a reduction in cutting forces. Surface quality was improved when HFVA turning alloy steel due to the smaller built-up edge that resulted from the reduced friction.

Takeyama and Kato [27] have experimentally shown the improvement in cutting performance achievable with HFVA drilling of aluminum. Mean thrust force and burr height were reduced by 62% and 75% respectively. The drill was vibrated ultrasonically at 200 kHz and 7-13.5  $\mu\text{m}$  in the axial direction. According to their theory, when the drill advances and half of the thickness of the material below the chisel edge of the drill becomes equal to or smaller than the amplitude of the induced high frequency vibration, the primary cutting motion is converted from rotational drilling action to ultrasonic impact action. These impact actions generate stress concentrations on the primary cutting path, and the material is cut with less thrust force. The oscillatory motion also provides a

slicing path at the circumferential edge of the tool, and the material around the hole perimeter tends to be sliced away. This results in less plastic deformation of material around the hole perimeter, and reduces burr size.

Moriwaki *et al.* [28] investigated the application of HFVA turning of soda-lime glass using single crystal diamond tools. They studied the effect of ultrasonic vibration assistance on the brittle-ductile transition and the transfer of tool edge profile to the machined surface. The applied ultrasonic assistance was 40 kHz with a maximum amplitude of 5  $\mu\text{m}$ . They reported that the intermittent cutting characteristic of HFVA turning causes separation of the rake face of the tool from the chip. This formed an aerodynamic lubrication between the tool rake face and the chip, reducing the friction between the two surfaces, and reducing the instantaneous cutting force and average cutting force. They also reported that the tool edge profile was completely transferred onto the machined surface using ultrasonic assisted turning, while with conventional turning, the machined surface profile has only half the depth of the tool edge profile. This observation suggested that the elastic recovery of the work material after the cut is completed is relatively small. This is logical because of the reduction in cutting force and the instantaneous elastic recovery of the work material when the tool is separated from the machined surface.

Babitsky *et al.* [29 - 32] have published several papers on HFVA turning. Their research included finite element analysis of the mechanism of ultrasonic assisted turning [29 & 30] and experimental investigations [31 & 32].

Their reported finite element model [29 & 30] included the elastic and plastic behaviour of the work material and the thermal behavior. Based on their simulation results, in HFVA turning the cutting tool remains in contact with the chip for 40% of the total cutting time. In regards to cutting forces, although the maximum stress values changes minimally, the stress state of HFVA turning changes significantly within each cycle of vibration. This resulted in a significant reduction in the maximum and average cutting forces. From the reported simulation results, the reductions are up to three times. A reduction in cutting tool temperature was also reported. The reduction in contact time was hypothesized to be the reason for this temperature reduction. This may lead to a reduction in tool wear in practice. Their simulation results also showed a reduction in residual tensile strain on the machined surface. This improves the surface quality by reducing surface fractures due to high residual tensile stress. Other findings included a reduction in chip thickness and chip curvature, which contributed to the reduction in cutting forces.

The experimental investigations reported by Babitsky *et al.* [31 & 32] included turning of nickel-based alloys C263, Inconel-718, and mild steel. The surface roughness and roundness of the work material machined by HFVA and conventional turning were compared. They reported improvements of surface roughness up to 50% with HFVA turning. They hypothesized that this improvement is due to the high frequency “vibro-impact” nature of the ultrasonic assisted turning increasing the dynamic stiffness of the whole cutting system, improving the accuracy of the cutting process. The peak-to-valley measurements of the roundness of the machined work material were also improved by up

to 50% with HFVA turning. This is again due to the increase of the system stiffness improving the accuracy of the cut.

In our previous work [33 - 35], a HFVA workpiece holder has been developed, and HFVA drilling of aluminum has been studied. Vibration was applied by a piezoelectric actuator attached to the workpiece holder. Based on the experimental results, we concluded that HFVA drilling can produce smaller burrs when suitable vibrations were applied [34 & 35]. However, with incorrect vibration assistance, larger burrs can be produced. HFVA drilling also produced larger tool wear on standard uncoated high speed steel (HSS) drills. Our further investigations showed that thrust force is reduced with HFVA drilling, and tool wear can be reduced with coated drills [35]. Moreover, the burr reduction performance of HFVA drilling did not deteriorate even with worn drills.

### **2.5.3 CFVA machining**

CFVA machining combines both low frequency and high frequency vibration components to produce a complex vibration motion between the tool and the work materials. The first CFVA machining application was presented by Ishikawa *et al.* [36] in the application of diamond core drilling of soda-glass. In diamond core drilling, diamond particles are bonded onto the tool. By rotating the diamond core drill, work material can be removed by the grinding action of the diamond particle. Adding vibration assistance will improve the grinding behaviour and chip evacuation, hence improving the material removal mechanism. With the reported experimental conditions, both LFVA and HFVA diamond core drilling alone can reduce the drilling force by up to 50%, but CFVA diamond core drilling can reduce the drilling force by up to 75%.

#### 2.5.4 Two degree vibration assisted machining

A recent addition to vibration assisted machining technology is the introduction of two degrees-of-freedom (DOF) vibration assistance. Moriwaki *et al.* [37 & 38] have reported a novel cutting methodology called elliptical vibration cutting, where vibrations are applied in two orthogonal directions, causing the tool to vibrate in an elliptical locus. Their work started with a study of low frequency elliptical vibration cutting [37], followed by the design and development of a high frequency (ultrasonic frequency) elliptical vibration turning tool holder and its application in diamond cutting of hardened steel [38].

The principal of elliptical vibration cutting is very similar to the one DOF vibration assisted cutting presented in sections 2.5.1-2.5.3. Either low or high frequency and low amplitude (ranging from 7-15  $\mu\text{m}$ ) vibrations are added to the direction of cutting velocity, and the direction of the depth of cut. This results in an elliptical vibration locus of the cutting tool (see Figure 2.5.1).

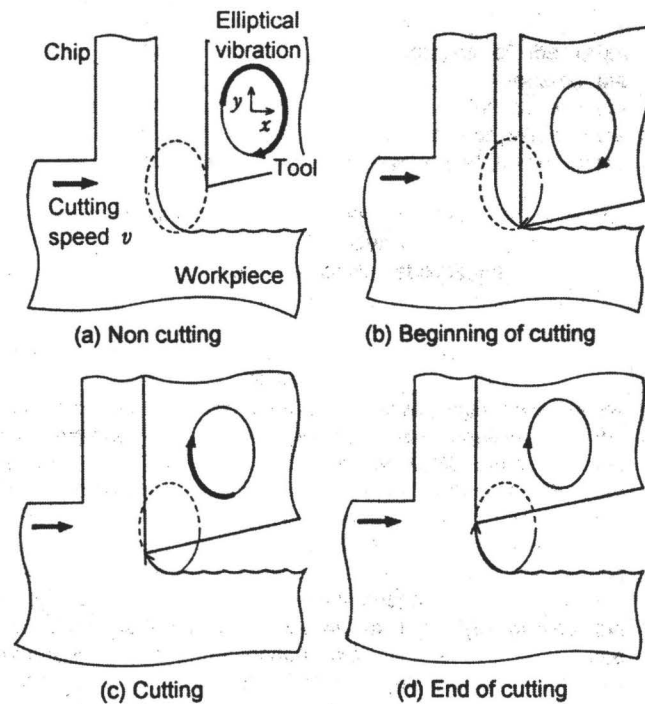


**Figure 2.5.1: Principal of elliptical vibration cutting (Moriwaki and Shamoto [37]).**

A low frequency elliptical vibration cutting system was successfully developed, and experimental results of cutting oxygen free copper were presented in [37]. Comparisons between the cutting forces measured from conventional cutting, one-degree vibration cutting, and elliptical vibration cutting were reported. Although the average principal and thrust forces of one DOF vibration cutting is lower compared with conventional cutting, the maximum value of the forces are the same. However, elliptical vibration cutting showed a reduction in the maximum cutting forces as well. Moreover, negative thrust force was observed. This negative thrust force resulted from the reversal of the frictional force acting on the rake face. With the vibration in the depth of cut direction, there exists a certain period of time where the tool's upward velocity is larger

than the chip velocity, causing a reversal of frictional force. This phenomenon is very similar to the chip evacuation effect of the axial vibration assistance in drilling. The chip thickness was also reduced by elliptical vibration cutting.

Moriwaki and Shamoto [38] later developed a high frequency elliptical vibrator. The principal of the vibrator is to excite a pinned beam to its natural resonance. The amplitude is magnified by a step horn design. They reported that the developed vibrator can be resonated at 20 kHz, with a maximum amplitude of 4  $\mu\text{m}$ . The developed system was used again for elliptical vibration assisted turning of oxygen free copper, and the results were compared with those obtained from one DOF vibration assisted turning as well as conventional turning. Their experiments showed that the chip thickness, principal force, and thrust force were reduced, which were in agreement with their previous findings. Moreover, the width of the chips was equal to the width of the work material for elliptical vibration turning, while both conventional and one DOF vibration assisted turning produced chips with larger width. Because of this observation, they concluded that elliptical vibration turning can reduce burr size along the width direction, although no burr measurement was reported. The surface profile and roughness of the machined surfaces were improved by using elliptical vibration turning as well.

### **2.5.5 VAD model**

Based on the theoretical model of drilling presented in [13 & 14], Zhang *et al.* [39] developed a theoretical model for VAD. The variation of cutting angles and uncut chip

thickness with time complicates the analysis of VAD. In their model, the total displacement and velocity of the tool in VAD are expressed as:

$$x(t) = A \sin(2\pi f t) + Fnt \quad (2.5.1)$$

$$v(t) = 2\pi f A \cos(2\pi f t) + Fn \quad (2.5.2)$$

where  $A$  is the vibration amplitude,  $f$  is the vibration frequency,  $t$  represents the time,  $F$  is the feed rate and  $n$  is the spindle speed in rpm. Expressing equations (2.5.1) in terms of the rotation angle of the drill  $\theta$  gives:

$$x(t) = A \sin\left(\frac{f}{n} \theta\right) + \frac{F}{2\pi} \theta \quad (2.5.3)$$

where  $\theta = 2\pi n t$ . Equation (2.5.3) expresses the axial displacement equation for one of the cutting lips. The other cutting lip will be  $180^\circ$  apart. By expressing the axial depth of cut in terms of  $\theta$ , the maximum depth of cut at different locations can be monitored. This method has been referred to as “surface updating” in the dynamic modeling of a drilling process with the presence of chatter vibration [Roukema & Altintas, 40 & 41]. With the maximum depth of cut determined, the instantaneous axial uncut chip thickness can be expressed as:

$$h_f = \begin{cases} Z(\theta) - \max\{Z_k(\theta)\} & \text{if } Z(\theta) > \max\{Z_k(\theta)\} \\ 0 & \text{otherwise} \end{cases} \quad (2.5.4)$$

The dynamic uncut chip thickness can then be expressed again using the geometrical properties of the drill. It is important to note that these geometric properties vary with time in VAD.  $h_f$  is used to calculate the dynamic uncut chip thickness,  $h_t$ . Note that  $h_t$

is equivalent to  $t_1$  used in [13 & 14]. After calculating  $h_l$ , the thrust force in VAD is predicted by following the method shown in [13 & 14].

Zhang *et al.* [39] proposed a model for predicting thrust force in VAD by analyzing the uncut chip thickness. This model however still depends on an experimentally determined  $k_{AB}$ . The tested vibration condition is also limited to 700 Hz. At higher vibration frequency, the material properties could change because of the increase in strain rate, and therefore  $k_{AB}$  could vary significantly. More experiments would likely be necessary to determine the proper  $k_{AB}$  for different vibration frequencies.

Wang *et al.* [42] presented a thrust force model for VAD by using a similar surface updating method to determine the instantaneous axial uncut chip thickness. However, instead of using the cutting pressure  $k_{AB}$ , they determined the resultant cutting force analytically using only the mechanistic cutting models developed by Watson [11 & 12]. The material shear strength is assumed to be constant with increasing vibration frequency. The model predictions are consistent with the presented experimental results, with a worst case error of 30% and averaged error of 23%. Theoretically this model does not require any experimental calibration. However, the tested vibration frequency is limited to 100 Hz only. At higher vibration frequency, the resultant cutting velocity will be increased, which also significantly increases the strain rate. High strain rate is associated with higher material shear strength. It is expected that as vibration frequency increases, the material shear strength will also increase significantly, and therefore using a constant material shear strength value in modeling high frequency VAD is inappropriate. Note that they reported using a vibration amplitude of 0.035 mm in all of

the experiments, which is three to four times higher than the typical vibration amplitude used in VAD [3-6]. Moreover, the typical vibration frequency used in VAD is at least 20 times higher than 100Hz [3-6], and therefore the resultant cutting velocity is significantly higher than their experiments.

The vibratory nature of VAD is very similar to regenerative chatter, and therefore literature related to the dynamic modeling of metal cutting with regenerative chatter will be briefly discussed in this section. Altintas [7] presented the dynamics of the general metal cutting process and reported that a wavy machined surface will be generated after the first cut on the workpiece. Budak and Altintas [43 & 44] studied and modeled the dynamic cutting forces for milling with chatter vibrations. Their studies modeled the variation of uncut chip thickness by the profile updating method discussed above. Li and Li [45] modeled the dynamic cutting forces for milling by modeling the variation of uncut chip thickness and strain-rate dependent shear strength. Roukema and Altintas [43 – 44, 46] presented the modeling of the dynamic cutting forces for drilling by modeling the variation of uncut chip thickness. Wu [47], Ismail *et al.* [48], Chandiramani and Pothala [49], and Moufki *et al.* [50] modeled the dynamic cutting force with the presence of plowing. The plowing forces are modeled analytically by determining the displaced volume of the workpiece. Lee and Altintas [51], and Wang and Zheung [52] modeled the plowing force empirically, and verified that the plowing force can have a significant effect on the total force.

## 2.6 CONCLUSIONS

Vibration assisted machining provides a convenient way to improve the machining performance compared to conventional machining. The vibration is typically induced by an external vibration assisted tool holder that retrofits onto modern machining centre. This tool holder can be designed to be installed onto an existing conventional machining center, minimizing the required modification. There are four existing types of vibration assisted machining: LFVA machining, HFVA machining, CFVA machining, and two-DOF vibration assisted machining.

Based on this review, LFVA machining alters the chip formation and can reduce the cutting forces. LFVA machining varies the instantaneous cutting velocity in turning, and both instantaneous cutting velocity and uncut chip thickness in drilling. These variations provide significant impact on the resultant cutting forces. The papers also consistently showed that there exists a better, or favourable, vibration condition. To maximize the performance of LFVA machining, the vibration condition must be carefully chosen. However, the published literature lacks a proper model to predict the favourable vibration condition, limiting the performance and applications of LFVA machining. Moreover, LFVA machining has been applied to ceramic and brittle materials only. No application of LFVA machining to ductile materials has been published.

HFVA machining contributes significantly to reductions in cutting forces and increases in machining accuracy. The major mechanism producing these benefits is the intermittent cutting nature of HFVA machining which alters the overall cutting behaviour of the process. It has been consistently reported that a favourable vibration condition

exists for a particular cutting condition, and poor choices of vibration conditions could increase thrust force and burr size. However, no proper model that can predict the suitable vibration conditions has been found. Moreover, because of the difficulty in achieving high frequency vibration, the vibration conditions found in the published literature are either limited to a particular resonant frequency, or limited to a very small amplitude (1-2 $\mu\text{m}$ ) only.

CFVA machining reduces cutting forces in diamond core drilling of ceramic materials. However, its application on metals has not been published. Since the material removal mechanism of diamond core drilling and conventional drilling is different, further investigation is necessary for CFVA drilling.

Two-DOF vibration assisted turning can further improve the performance of either LFVA or HFVA turning. The two governing mechanisms contributing to the cutting force reduction are the intermittent cutting provided by the vibration along the cutting velocity direction, and the variation of uncut chip thickness provided by the vibration along the depth of cut direction. However, the application of two-DOF vibration assisted drilling has not been reported.

Based on this review, analytical drilling models predicting thrust forces for conventional drilling are well established. However, due to the dynamic nature of VAD, these models cannot be directly applied to VAD. Zhang *et al.* [39] and Wang *et al.* [40] both presented analytical models to predict thrust forces for VAD. However, their models ignored the effects of strain-rate dependent shear strength and plowing forces, which will be shown to have significant effects on thrust force in Chapter 5 of this thesis. Further

research is therefore necessary to develop a reliable and accurate thrust force model for VAD. An obvious direction is incorporating the strain-rate dependent shear strength, and the plowing force model developed primarily for modeling regenerative chatter into the current VAD model.

Literature on finite element models for drilling burr formation has also been reviewed. No finite element models for VAD have been published. One major drawback with finite element modeling is that it is very difficult to use this method to predict the optimal cutting condition to minimize the burr size. One approach is to run many simulations to identify this cutting condition or ranges of cutting conditions, but this approach would be very time consuming. Therefore this thesis focuses on developing an analytical model for burr height prediction in VAD.

While drilling burr formation has been widely studied, few models predicting burr size efficiently exist in the current literature. Moreover, these models are limited to predict burr size for conventional drilling only. Further research is therefore necessary to develop an accurate burr size model for VAD. Because burr height is typically the dominant challenge in burr removal process [33], this thesis focuses on developing a burr height model for VAD.

The objective of this research is to develop an analytical model to predict the resultant burr height for VAD. The successful development of such a model can be used to determine the suitable vibration conditions, and will be beneficial for future research on LFVA, HFVA, or CFVA drilling. Two-DOF VAD involves complicated tool holder design to generate both axial and torsional vibrations, and therefore is beyond the scope

of this thesis. Moreover, the governing mechanisms of two-DOF vibration assisted turning are intermittent cutting and variation of uncut chip thickness. These mechanisms can already be achieved by one-DOF VAD. The model that will be presented in this thesis will provide valuable information for future research of VAD including two-degree VAD. This thesis also presents a simplified analytical method to determine the suitable vibration conditions for burr height reduction without the need for extensive simulation.

## CHAPTER 3

### THRUST FORCE MODELING FOR VAD

#### 3.1 INTRODUCTION

VAD is a highly dynamic cutting process, and the relationship between thrust force and vibration condition is highly nonlinear. Accurate thrust force prediction is important for burr height prediction. In this chapter, the development of a novel thrust force model for VAD is presented. The developed model is fundamentally based on the thrust force model for conventional drilling, with a few crucial modifications to model the dynamic behavior of VAD.

#### 3.2 THRUST FORCE MODEL FOR CONVENTIONAL DRILLING

##### 3.2.1 Introduction

As discussed in Chapter 2, the thrust force model for conventional drilling is well established and is based on the traditional tool wedge model for metal cutting. Figure 3.2.1 shows the schematic of a traditional tool wedge model, where  $\phi$  is the shear angle,  $\gamma$  is the rake angle,  $h$  is the uncut chip thickness, and  $h_c$  is the chip thickness.  $F_C$  and

$F_T$  are the principal cutting forces acting on the workpiece in the cutting and feed direction, respectively. Based on conventional metal removal theories, the principal cutting forces are:

$$F_C = \frac{\tau h w \cos(\lambda - \gamma)}{\sin \phi \cos(\phi + \lambda - \gamma)} \text{ and} \quad (3.2.1)$$

$$F_T = \frac{\tau h w \sin(\lambda - \gamma)}{\sin \phi \cos(\phi + \lambda - \gamma)}, \quad (3.2.2)$$

where  $\tau$  is the material's shear strength,  $w$  is the width of the cut, and  $\lambda$  is the friction angle.

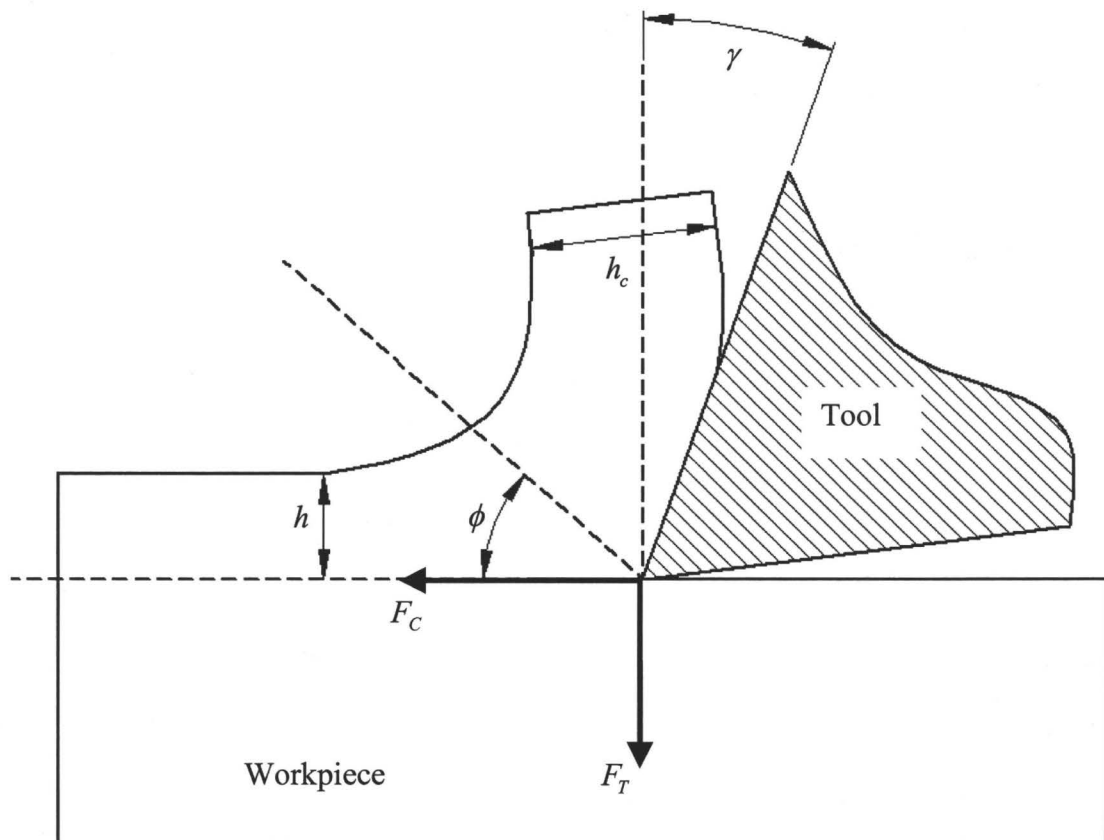
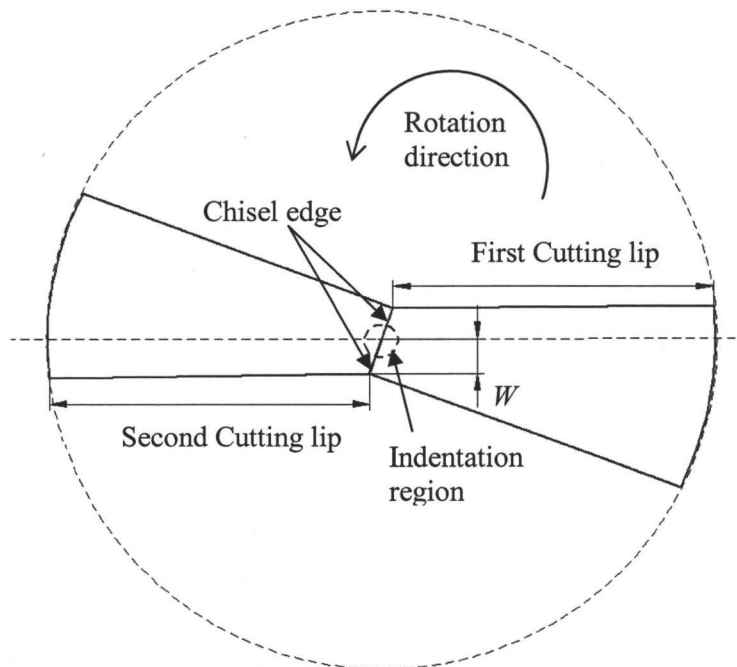


Figure 3.2.1. Schematic of the tool wedge model.

To apply the conventional metal removal theories to drilling, the drill is typically divided into three regions: the indentation region in the very centre of a drill on the chisel edge, the orthogonal cutting region on the chisel edge, and the oblique cutting region on the cutting lips, as shown in Figure 3.2.2. This thesis addresses burr reduction in drilling aluminum 6061-T6. Burr formation occurs at the final stage of drilling where the tool exits the work material. The cutting force along the chisel edge contributes only 10-20% of the total cutting force [7]. Because the thrust force reduction by VAD reaches 25% only [33], the contribution of the chisel edge to the reduction is negligible. Therefore, in this thesis, the cutting forces along the chisel edge will be calibrated experimentally. The material presented in this chapter will focus on the cutting lips of the drill.



**Figure 3.2.2. Cutting regions of a drill.**

### 3.2.2 Cutting model for the cutting lips of a drill

In drilling, the geometries of the cutting lips vary with radius. Therefore, the cutting lips of a drill must be divided into elements that are analyzed individually (see Figure 3.2.3). The effective cutting angles and the resultant cutting direction can be analyzed, and the principal cutting forces can then be calculated by equations (3.2.1) and (3.2.2) for each element.

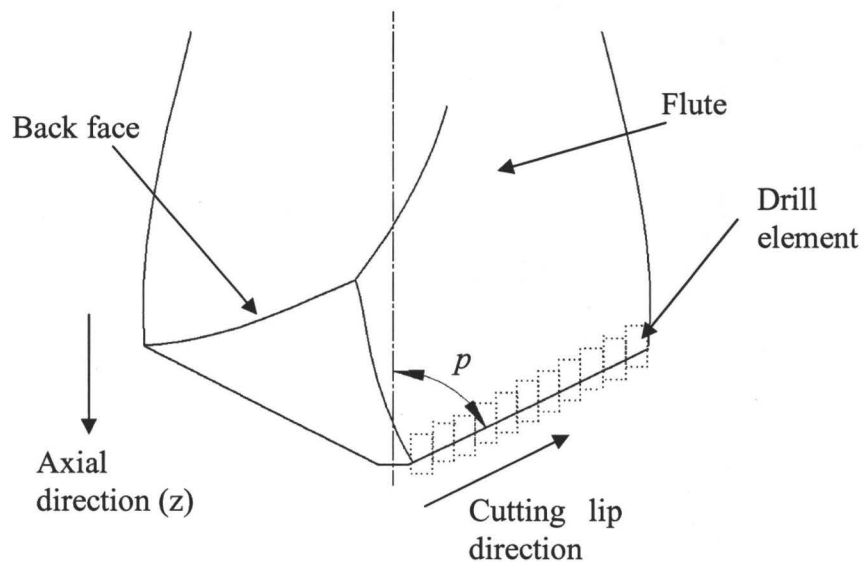


**Figure 3.2.3. Cutting lips of a drill divided into elements (only one of the two lips is shown).**

Figure 3.2.4 shows the schematic of a drill and the effective geometry of an element. The effective uncut chip thickness,  $h_l$ , is constant for conventional drilling. If  $F$  is the drill feed of the drilling process in mm/rev, then the axial uncut chip thickness is constant for a two-flute drill:

$$h_f = \frac{F}{2} . \tag{3.2.3}$$

The effective uncut chip thickness  $h_l$  for a particular element with distance  $r_i$  away from the centre of the drill is:

$$h_l = h_f \sin(p) \cos\left(\frac{\zeta}{2}\right) , \tag{3.2.4}$$

where  $\zeta = \tan^{-1}[\tan(\omega)\cos(p)]$  , (3.2.5)

$$\omega = \sin^{-1}\left(\frac{W}{r_i}\right) \tag{3.2.6}$$

and  $p$  is half of the point angle as shown in Figure 3.2.3,  $W$  is half of the web thickness as shown in Figure 3.2.2.

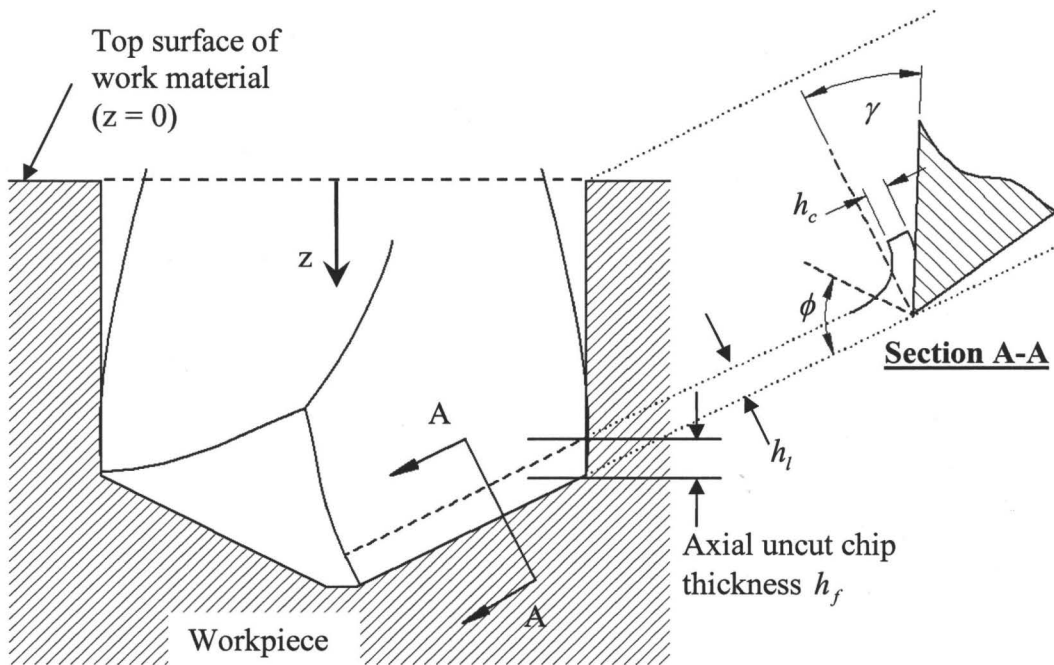


Figure 3.2.4. Cutting geometry of a particular element on a cutting lip.

The width of the element  $\Delta w$  can be found by calculating the length of the cutting lips, then dividing by the number of elements,  $M$ . Referring to Figure 3.2.5, which shows the end view of a drill,  $\Delta w$  can be calculated by the following equations:

$$\Delta w = \frac{D \cos(\omega_0) - D' \cos(\omega')}{2M}, \quad (3.2.7)$$

where  $\omega_0 = \tan^{-1}\left(\frac{2W}{D}\right)$  and  $(3.2.8)$

$$\omega' = \sin^{-1}\left(\frac{W}{W'}\right). \quad (3.2.9)$$

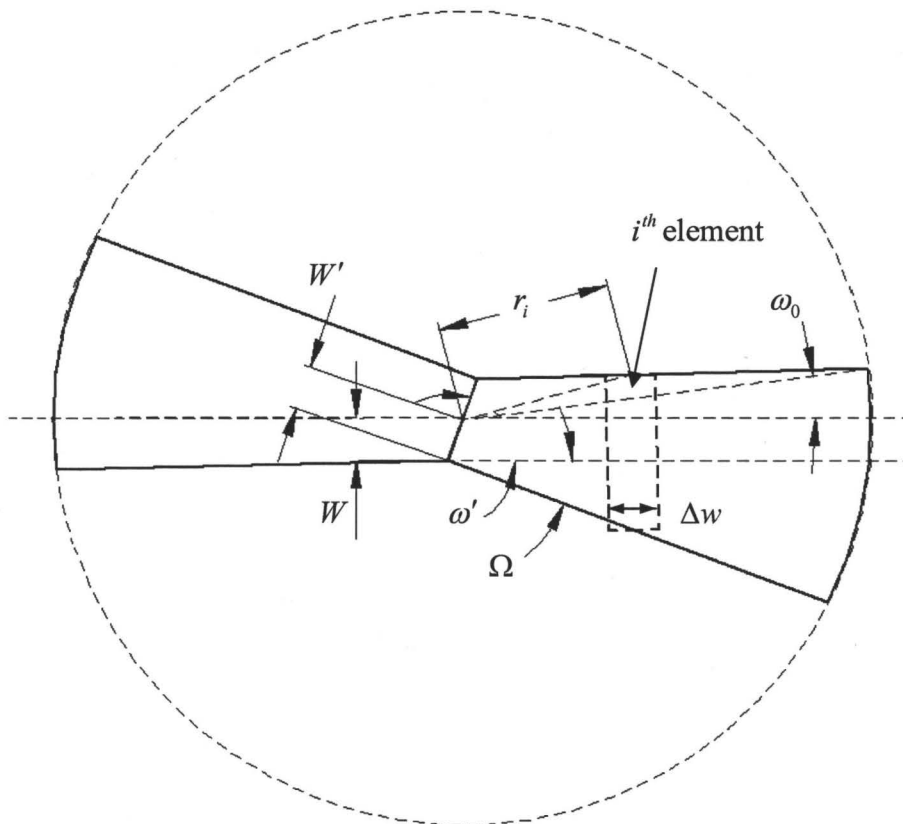


Figure 3.2.5. End view of a drill showing its element on one of the cutting lips.

The effective, or dynamic, shear angle  $\phi_{nd}$  in metal cutting is traditionally determined by experimentally measuring the chip thickness for the particular cutting condition. Note that the effective angles are represented by the subscript  $nd$ . Referring to Figure 3.2.1:

$$\phi_{nd} \approx \tan^{-1}\left(\frac{h}{h_c}\right). \quad (3.2.10)$$

However, because the cutting geometry of each individual element varies, determining all possible values of  $\phi_{nd}$  is not practical. Instead, Lee and Shaffer's model [53] is used in this thesis:

$$\phi_{nd} + \lambda_{nd} - \gamma_{nd} = \frac{\pi}{4}. \quad (3.2.11)$$

Another approximation can be applied to further simplify equation (3.2.1) and (3.2.2) [54]:

$$\lambda_{nd} = \frac{\pi}{6} + \frac{\gamma_{nd}}{2}. \quad (3.2.12)$$

The remaining unknowns are the material's shear strength  $\tau$  and the effective rake angle  $\gamma_{nd}$ .  $\tau$  is known to be dependent on the strain and strain rate but commonly assumed to be constant throughout the drilling process. The generic value of  $\tau$  can be found in a material handbook, but these generic values were obtained by experimental measurement at a relatively low strain rate ( $10^{-3} - 10^{-1} s^{-1}$ ). During metal cutting, the strain rates at the primary and secondary shear zone can reach  $10^3 - 10^6 s^{-1}$ . Thus the generic values of  $\tau$  from a material handbook are not suitable. One common method to estimate material shear strength at a high strain rate is the Johnson–Cook model [55], which states:

$$\tau = \frac{1}{2} [A + B(\varepsilon)^n] \left[ 1 + C \ln \left( \frac{\dot{\varepsilon}}{\dot{\varepsilon}_0} \right) \right] (1 - T_h^m), \quad (3.2.13)$$

where  $\varepsilon$  is the strain,  $\dot{\varepsilon}$  is the strain rate,  $\dot{\varepsilon}_0$  is the reference strain rate, and  $T_h$ ,  $A$ ,  $B$ ,  $C$ ,  $m$  and  $n$  are material-dependent constants. Guo [56] reported that for drilling aluminum 6061-T6, suitable values of the constants are:

$$\begin{aligned} A &= 275, \\ B &= 86, \\ C &= 0.058 - 0.194h - 0.003\bar{V}, \\ \dot{\varepsilon}_0 &= 1, \\ T_h &> 1, \\ m &= -\infty \text{ and} \\ n &= 0.39. \end{aligned} \quad (3.2.14)$$

Note that  $C$  is time varying for VAD. The strain and strain rate during a metal removal process can be estimated by the following equations:

$$\varepsilon = \frac{\cos(\gamma_{nd})}{\sin(\phi_{nd})\cos(\phi_{nd} - \gamma_{nd})} \text{ and} \quad (3.2.15)$$

$$\dot{\varepsilon} = \frac{\cos(\gamma_{nd})\bar{V}}{\cos(\phi_{nd} - \gamma_{nd})v}. \quad (3.2.16)$$

In equations (3.2.14) to (3.2.16),  $\bar{V}$  is the magnitude of the resultant cutting velocity and  $v$  is the shear thickness.  $v$  is a material dependent property, and for aluminum 6061-T6,  $v$  is assumed to be 0.005 mm [56]. The effective rake angle  $\gamma_{nd}$  can be estimated by analyzing the cutting directions and geometry of the cutting element for each element. Following the derivation given in [11-12] and referring to Figure 3.2.5:

$$\kappa_r = \tan^{-1}[-\tan(p)\cos(\omega)], \quad (3.2.17)$$

$$r_i = \sqrt{\left[ D \cos \omega_0 - \left( i - \frac{1}{2} \right) \Delta w \right]^2 + W^2} \quad , \quad (3.2.18)$$

$$\beta = \tan^{-1} \left[ \frac{2r_i \tan(\beta_0)}{D} \right] \quad , \quad (3.2.19)$$

$$\gamma_f = \tan^{-1} \left[ \frac{\tan(\beta) \sin(\omega)}{\sin(p) - \cos(p) \sin(\omega) \tan(\beta)} \right] \quad , \quad (3.2.20)$$

$$V_{axial} = Fn \quad , \quad (3.2.21)$$

$$\eta_d = \tan^{-1} \left[ \frac{V_{axial}}{2\pi r_i n} \right] = \tan^{-1} \left[ \frac{Fn}{2\pi r_i n} \right] \quad , \quad (3.2.22)$$

$$\kappa_{rd} = \tan^{-1} \left[ \frac{\sin(\kappa_r)}{\cos(\kappa_r) \cos(\eta_d) + \tan(\lambda_s) \sin(\eta_d)} \right] \quad , \quad (3.2.23)$$

$$\lambda_{sd} = \sin^{-1} \left[ \cos(p) \sin(\eta_d) + \sin(p) \cos(\omega) \cos(\eta_d) \right] \quad , \quad (3.2.24)$$

$$\gamma_{fd} = \gamma_f + \eta_d \quad , \quad \text{and} \quad (3.2.25)$$

$$\gamma_{nd} = \tan^{-1} \left[ \frac{\tan(\gamma_{fd}) \cos(\lambda_{sd})}{\sin(\kappa_{rd})} + \frac{\sin(\lambda_{sd})}{\tan(\kappa_{rd})} \right] \quad . \quad (3.2.26)$$

where  $\Delta w$  is the width of each element and  $\beta_0$  is the helix angle of the drill. Equations (3.2.17) to (3.2.26) represent the geometric relationships between the cutting angles. The important parameters are the effective rake angle  $\gamma_{nd}$  and the dynamic feed angle  $\eta_d$ , which defines the cutting direction of a drilling process. The principal cutting forces can now be calculated for each element using equation (3.2.1) and (3.2.2). The corresponding thrust force for each element can be expressed as:

$$\Delta P_i = F_{l,T} \sin p \cos \eta_d + F_{l,C} \sin \eta_d \quad , \quad (3.2.27)$$

where the subscript  $i$  represents the thrust and principal cutting forces for the  $i^{\text{th}}$  element.

The total thrust force can then be found by summing the thrust force for all elements:

$$P_{Total} = \sum_{i=1}^M \Delta P_i . \quad (3.2.28)$$

### 3.3 THRUST FORCE MODELING FOR VAD

One of the major differences between VAD and conventional drilling is the variation of drill feed. Following the discussion presented in Section 3.2, varying drill feed varies the effective uncut chip thickness, cutting geometries (especially the effective rake angle), strain and strain rate, and the material shear strength. In Chapter 2, various thrust force models for VAD that modeled only the variations of effective uncut chip thickness and cutting geometries were reported. In this section, the details of modeling these variations will be presented.

#### 3.3.1 Effective uncut chip thickness and cutting angles for VAD

As described in Section 3.2.2, the axial uncut chip thickness for conventional drilling is constant and can be calculated by equation (3.2.3). However, for VAD, the axial uncut chip thickness varies with time. Following Wang *et al.*'s [15] methodology, the instantaneous axial uncut chip thickness for VAD can be estimated by studying the instantaneous displacement and velocity of the tool. The displacement equals the summation of the displacement due to the feed  $Fnt$  and the displacement due to the vibration  $A\sin(2\pi ft)$  as follows:

$$z(t) = A \sin(2\pi f t) + F n t . \quad (3.3.1)$$

Similarly, the instantaneous velocity is:

$$\dot{z}(t) = 2\pi f A \cos(2\pi f t) + F n . \quad (3.3.2)$$

In equation (3.3.1) and (3.3.2),  $A$  and  $f$  are the vibration amplitude (mm) and frequency (Hz), respectively,  $F$  is the feed rate (mm/rev),  $n$  is the spindle speed (rev/sec), and  $t$  is the time (s), with  $t = 0$  representing the drill just above the material (*i.e.*  $z(0) = 0$ ). To determine the axial uncut chip thickness, which is critical to estimate cutting forces, it is necessary to monitor the maximum depth of removed material at the rotational angle of interest  $\theta$  (see Figure 3.3.1). Therefore it is more convenient to express equations (3.3.1) and (3.3.2) as a function of  $\theta$ . Note that  $\theta$  is measured from the centerline of the drill and not along the cutting lips. Transforming the independent variable from time ( $t$ ) to rotational angle of the drill ( $\theta$ ) by substituting  $\theta = 2\pi n t$  into equation (3.3.1) gives:

$$z(\theta) = A \sin\left(\frac{F\theta}{n}\right) + \frac{f\theta}{2\pi} \quad (3.3.3)$$

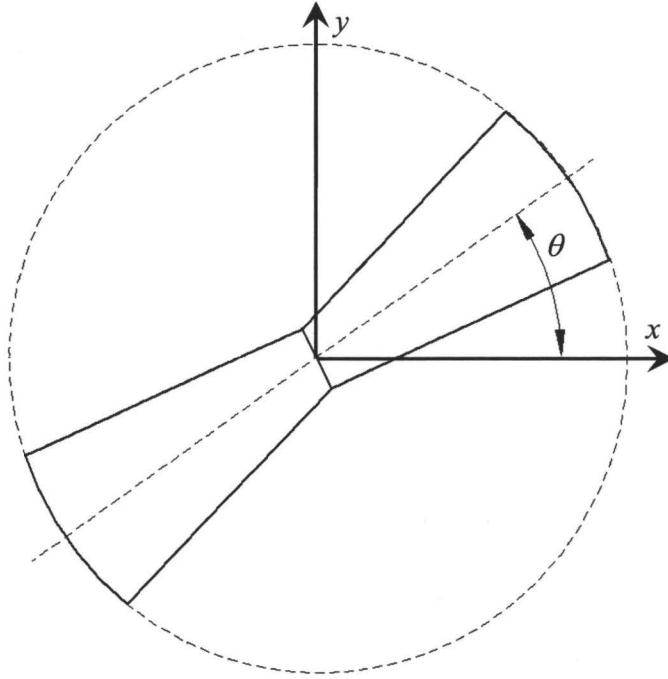


**Figure 3.3.1. Rotational angle of a cutting lip of a drill.**

To calculate the axial uncut chip thickness, the depth of the material immediately in front of the cutting lips ( $z_{\max}(\theta)$ ) must be determined (see Figure 3.3.2).  $z_{\max}(\theta)$  can be estimated by monitoring the axial location of the cutting lips prior to the current instant. For a two flute drill where there are two cutting lips at  $\pi$  radians away from each other, all the axial locations of the cutting lips prior to the current instant are equal to  $z(\theta - q\pi)$ , where  $q$  is a positive integer. Therefore, the maximum axial location of the cutting lips prior to the current instant, *i.e.* the depth of the material immediately in front of the cutting lips at the current instant  $z_{\max}(\theta)$ , equals:

$$z_{\max}(\theta) = z(\theta - m\pi), \quad (3.3.4)$$

where  $m$  is the minimum value that satisfies the expression:

$$z(\theta - m\pi) > z(\theta - [m+1]\pi) . \tag{3.3.5}$$

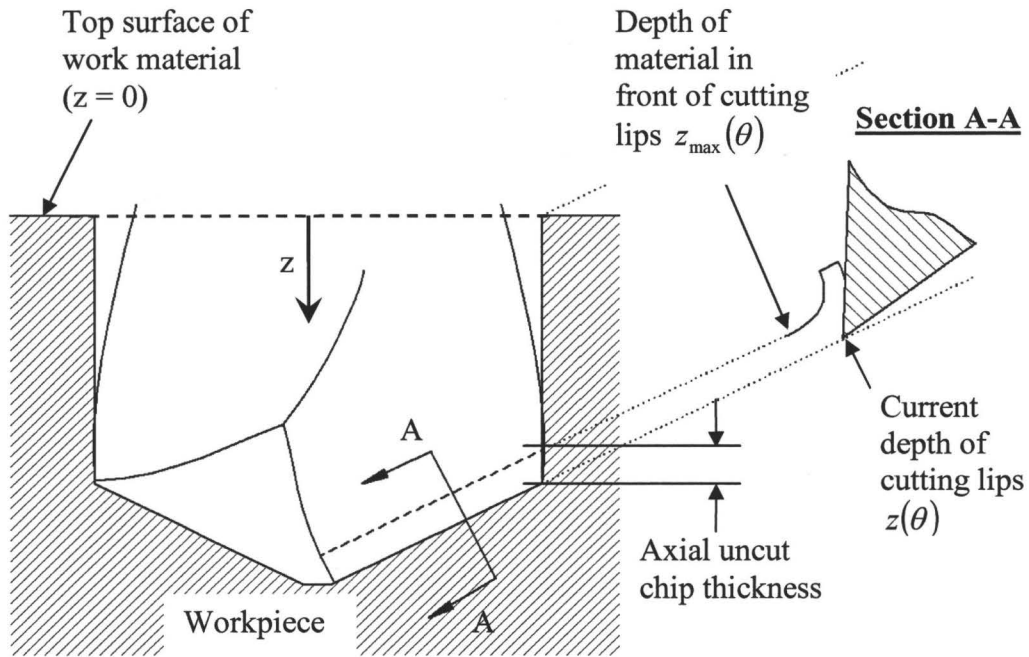
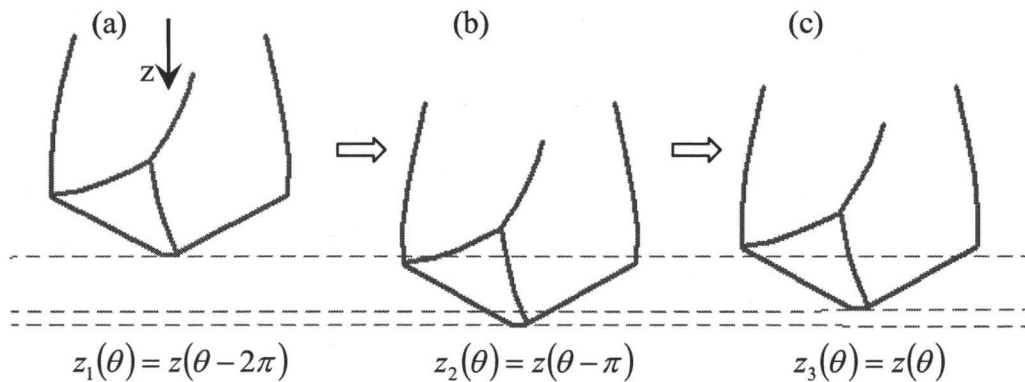


Figure 3.3.2. Geometry involved in determining the axial uncut chip thickness.

For the example shown in Figure 3.3.3,  $z_{\max}(\theta) = z(\theta - \pi)$  and  $m = 1$ . After  $z_{\max}(\theta)$  is found, the axial uncut chip thickness  $h_f$  equals:

$$h_f = \begin{cases} z(\theta) - z_{\max}(\theta) & \text{if } z(\theta) > z_{\max}(\theta) \\ 0 & \text{otherwise} \end{cases} . \tag{3.3.6}$$



**Figure 3.3.3. Example of determining  $z_{\max}(\theta)$ .**

The effective uncut chip thickness  $h_l$  can then be calculated using equations (3.2.4) to (3.2.6). The equations used to calculate the cutting angles, equations (3.2.15) to (3.2.23), remain the same, except for equation (3.2.21). Because the axial velocity now equals:

$$V_{axial} = \dot{z}(t) + Fn , \quad (3.3.7)$$

therefore, the dynamic feed angle equals:

$$\eta_d = \tan^{-1} \left[ \frac{\dot{z}(t) + Fn}{2\pi r_k n} \right] . \quad (3.3.8)$$

Replacing equation (3.2.21) with (3.3.8),  $\gamma_{nd}$  for VAD can be calculated.

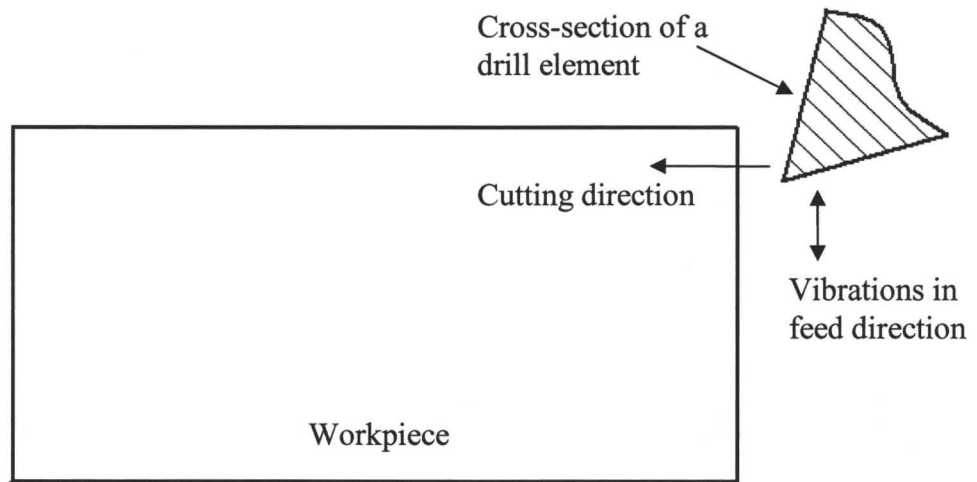
### 3.3.2 Plowing force estimation

Because of the oscillation of the drill during VAD, a wavy machined surface is produced after each half revolution of the drill. When the cutting edges engage the workpiece again, plowing can occur, as shown in Figure 3.3.4. If the volume of the workpiece material displaced by the tool is known, the plowing force can be estimated.

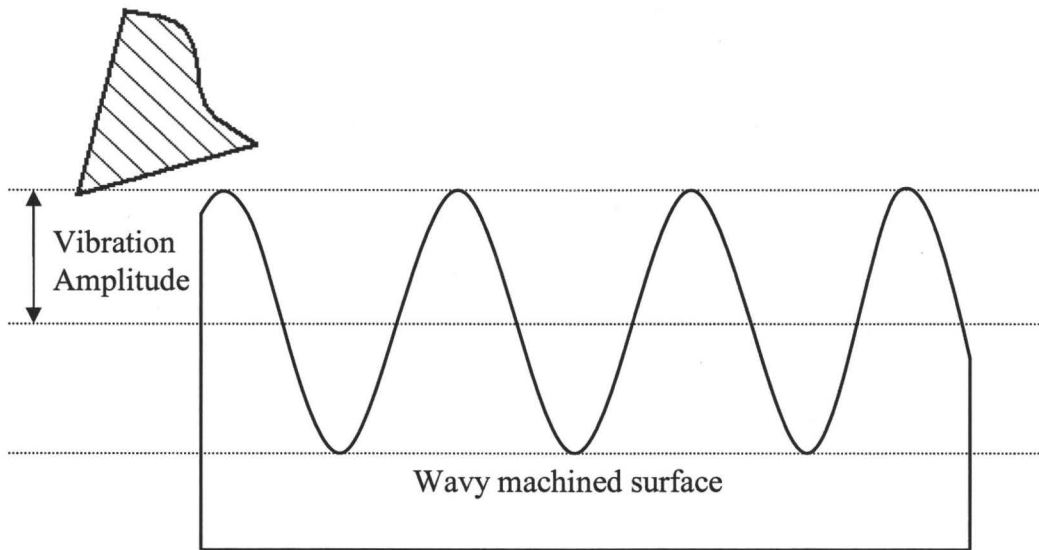
Based on the analysis by Wu [47], the resulting forces for the  $i^{th}$  element are:

$$F_{pt} = f_{sp} \Delta V_i \quad (3.3.9)$$

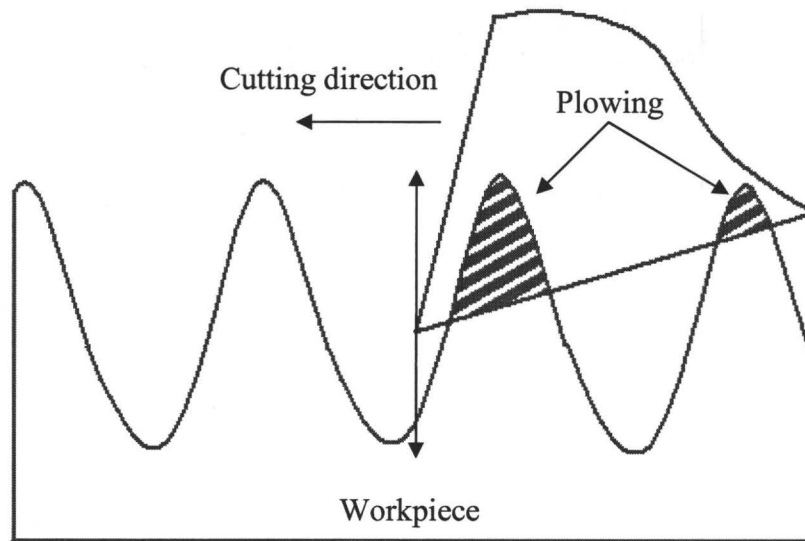
$$F_{px} = \mu_c F_{pt} . \quad (3.3.10)$$



*a) Initially, the drill element engages a flat surface.*



*b) After the first cut, a wavy machined surface is formed.*



*c) In subsequent cuts, the flank surface of the drill may come in contact with the machined surface (even at multiple locations), causing plowing of the material.*

**Figure 3.3.4. Formation of plowing force for an element in VAD.**

In equations (3.3.9) and (3.3.10),  $F_{pt}$  and  $F_{px}$  are the plowing force components in the thrust and horizontal directions, respectively;  $f_{sp}$  is the experimentally determined specific plowing force,  $\Delta V_i$  is the displaced volume, and  $\mu_c$  is the mean friction coefficient of the tool–work interface.  $\Delta V_i$  will now be estimated by considering the tool profile and the maximum depth of the machined surface.

The tool profile can be modeled by dividing each drill element into small segments along the drill flank direction. Figure 3.3.5 shows the difference between the drill elements and the segments on a drill element. The axial location of segment  $k$  on each drill element can be calculated by equation (3.3.10):

$$T_k = z(\theta) - i \cdot \Delta l_i \tan(\gamma), \quad (3.3.10)$$

where  $k$  refers to the  $k^{\text{th}}$  segment,  $\Delta l_i$  is the length of each segment, and  $\gamma$  is the flank clearance angle. The geometry of a drill element is shown in Figure 3.3.6. At any instant, the depth of the machined surface corresponding to each drill element is given by:

$$z'_{\max,k} = A \sin\left(\frac{f(\theta - j\pi - k\Delta\theta)}{n}\right) + \frac{F(\theta - j\pi - k\Delta\theta)}{2\pi} \quad k = 1, 2, \dots, \bar{k}, \quad (3.3.11)$$

where  $\Delta\theta$  is the rotational difference between each segment (see Figure 3.3.5),  $\bar{k}$  is the total number of segments on each element, and  $j$  is the minimum positive integer that satisfies the inequality:

$$A \sin\left(\frac{f(\theta - j\pi - k\Delta\theta)}{n}\right) + \frac{F(\theta - j\pi - k\Delta\theta)}{2\pi} > A \sin\left(\frac{f(\theta - (j+1)\pi - k\Delta\theta)}{n}\right) + \frac{F(\theta - (j+1)\pi - k\Delta\theta)}{2\pi} \quad (3.3.12)$$

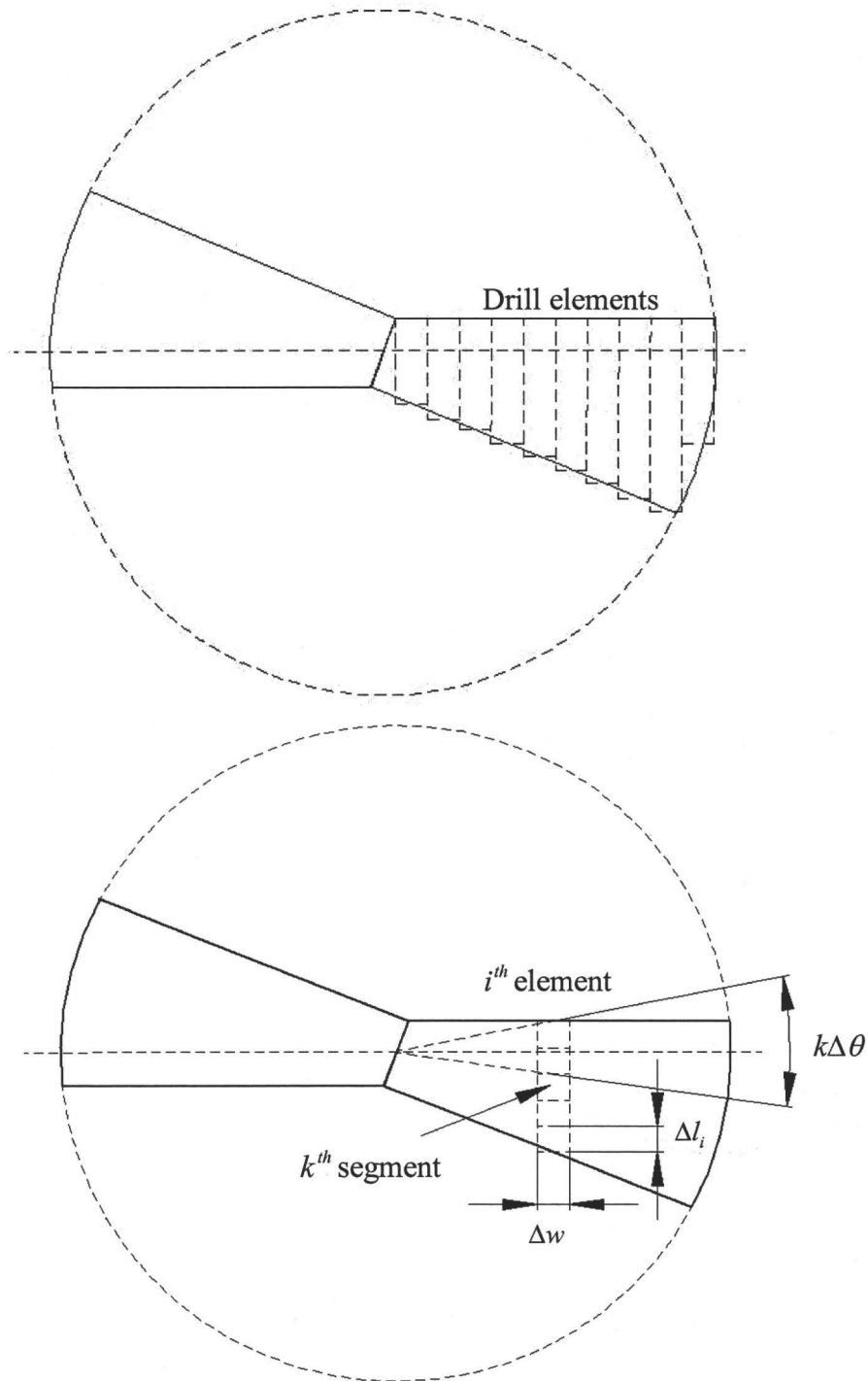


Figure 3.3.5. Geometry of drill elements and segments.

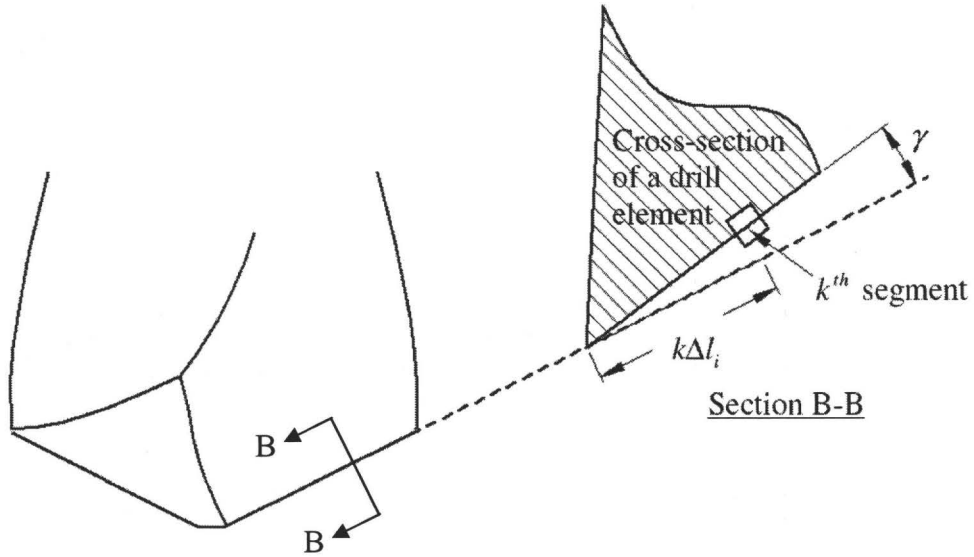


Figure 3.3.6. Geometry of the  $k^{\text{th}}$  segment.

The theory behind equation (3.3.12) is the same as the theory behind equation (3.3.5).

The plowing depth of the  $k^{\text{th}}$  segment on a drill element can then be calculated using:

$$\Delta d_k = \begin{cases} T_k - z'_{\max, k} & \text{if } T_k - z'_{\max, k} > 0 \\ 0 & \text{if } T_k - z'_{\max, k} < 0 \end{cases} \quad (3.3.13)$$

The displaced volume per segment can then be calculated by multiplying  $\Delta d_k$  with  $\Delta l_i$

and the width of the element  $\Delta w$  and summing as follows:

$$\Delta V_i = \sum_{k=1}^N \Delta d_k \Delta l_i \Delta w, \quad (3.3.14)$$

$$\text{where } \Delta l_i = \frac{2W + \left[ W' \cos \omega' + \frac{D}{2} \cos \omega_0 - \left( i - \frac{1}{2} \right) \Delta w \right] \tan \Omega}{N}, \quad (3.3.15)$$

and  $N$  equals the number of segments per element. Note that  $\Omega$  has been defined in Figure 3.2.5.

### 3.3.3 Strain rate-dependent shear strength model

As presented in Section 3.2.2, generic values of material shear strength are not appropriate for use in a metal cutting model because the strain rate along the primary and secondary shear zone during metal cutting reaches  $10^4$  to  $10^9$  times higher than the nominal strain rate ( $10^{-3}$  to  $10^{-1} s^{-1}$ ) used to determine generic material properties. As previously noted, the Johnson–Cook model should be used to estimate the shear strength  $\tau_i$ , and the empirical constants used in the Johnson–Cook model for aluminum 6061-T6 reported by Guo [56] were given in equation (3.2.14). These constants will be calibrated experimentally, which will be presented in Chapter 5. In this thesis,  $\tau_i$  is modeled by the following equations:

$$\tau_i = \frac{1}{2} \left( 247.5 + 77.4 \varepsilon^{0.38} \right) \left[ 1 + C \ln \left( \frac{\dot{\varepsilon}}{3.07} \right) \right], \quad (3.3.16)$$

$$C = 0.058 - 0.194 h_1 - 0.003 \bar{V}, \quad (3.3.17)$$

$$\varepsilon = \frac{\cos \gamma_{nd}}{\sin \phi_{nd} \cos(\phi_{nd} - \gamma_{nd})}, \text{ and} \quad (3.3.18)$$

$$\dot{\varepsilon} = \frac{\bar{V} \cos \gamma_{nd}}{0.005 \cos(\phi_{nd} - \gamma_{nd})}, \quad (3.3.19)$$

Because of the increase in strain rate, the shear strength of the material will be increased at a higher vibration frequency, resulting in a higher thrust force.

### 3.3.4 Total thrust force for VAD

The thrust force for VAD can be predicted by combining the results of Sections 3.2.2, and 3.3.1 to 3.3.3. The resultant thrust force for each element can be calculated as:

$$\Delta P_i = F_{l,T} \sin p \cos \eta_d + F_{l,C} \sin \eta_d + F_{pt} . \quad (3.3.20)$$

The total thrust force can be found by adding all the elemental thrust force components together, as in equation (3.2.28). Note that  $P_{Total}$  is now time dependent. The mean thrust force  $\bar{F}_{th}$  is calculated by:

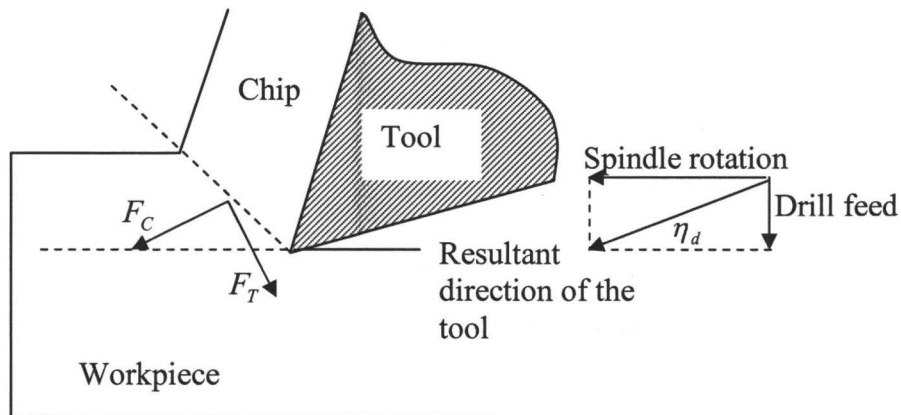
$$\bar{F}_{th} = \frac{1}{T} \int_0^T P_{Total} dt . \quad (3.3.21)$$

Because  $\eta_d$  varies in VAD, it is possible that under certain ranges of vibration conditions, the elemental and/or total thrust force becomes negative. These negative values represent a change in direction of thrust force. The vibration condition (combination of vibration frequency and amplitude) where the minimum thrust force in VAD equals zero is defined as the *critical vibration condition* in this thesis. In later chapters, it will be shown that the critical vibration conditions have important implications on burr height.

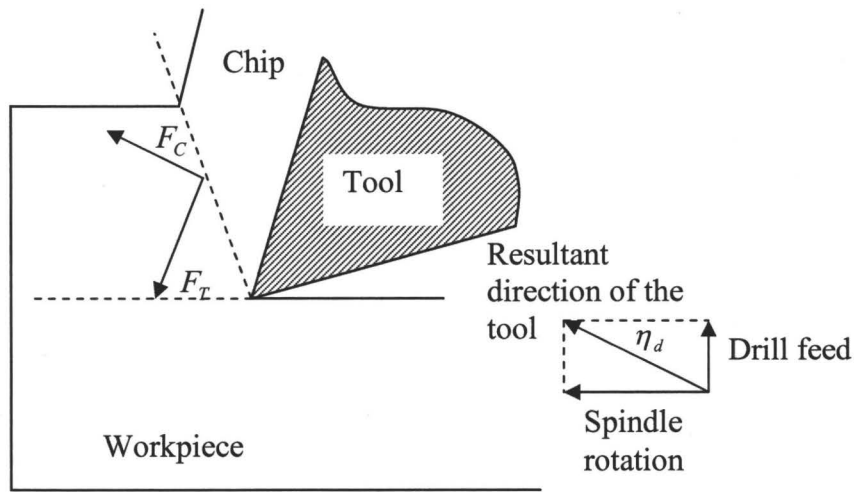
The occurrences of negative thrust force can be analyzed by studying the locus of a drill element. In VAD, when the vibration velocity is large enough, the direction of the feed can change from moving into the workpiece material (hereafter referred to as downward stroke) to moving out of the workpiece material (hereafter referred to as upward stroke). The condition where this phenomenon occurs is when the vibration velocity is larger than the drill feed velocity, *i.e.*

$$\dot{z}(t) > Fn . \quad (3.3.22)$$

Figure 3.3.7 shows the schematic of cutting forces during downward and upward strokes of the tool. During the downwards stroke, both of the principal cutting forces point downward, thereby creating a downward thrust force. Note that  $F_C$  is parallel to the resultant direction of the tool. However, during the upward stroke,  $F_C$  points upward, while  $F_T$  points downward. Depending on the dynamic feed angle  $\eta_d$  and the magnitudes of  $F_C$  and  $F_T$ , the direction of the resultant thrust force can be pointing upward (*i.e.* negative thrust force).



**a) Downward stroke of the tool**



**b) Upward stroke of the tool**

**Figure 3.3.7. Schematic of cutting forces during downward (a) and upward (b) strokes of the tool.**

Referring to equation (3.3.20), because the plowing force always points downward, the transition from positive to negative thrust force occurs when:

$$F_{C,k} \sin(\eta_d) > F_{T,k} \sin(p) \cos(\eta_d) + F_{pt,k} . \quad (3.3.23)$$

As mentioned above, the critical vibration conditions have important implications on burr height. Therefore, determining the critical vibration conditions is important. Equating the left and right hand sides of equation (3.3.23) gives:

$$F_{C,k} \sin(\eta_d) = F_{T,k} \sin(p) \cos(\eta_d) + F_{pt,k} . \quad (3.3.24)$$

The critical vibration condition for each element is different. To find the overall critical vibration condition, *i.e.* the condition when the total minimum thrust force reaches zero, the total thrust force must be considered. Therefore, equation (3.3.24) becomes:

$$\sum_{k=1}^M [F_{C,k} \sin(\eta_d)] = \sum_{k=1}^M [F_{T,k} \sin(p) \cos(\eta_d) + F_{pt,k}]. \quad (3.3.25)$$

Solving Equation (3.3.25) analytically can be very time consuming, but it can easily be solved by computer simulations. Note that all parameters in equation (3.3.25) are time dependent. To determine the critical vibration frequency, computer simulation of at least one complete vibration cycle is necessary.

### 3.4 CONCLUSIONS

This chapter presented the modeling and analysis of thrust force for VAD. Instead of the commonly used finite element modeling, an analytical approach has been used. This provides a model that is capable of predicting instantaneous and mean thrust force for different tool geometry, cutting conditions, and vibration conditions. The geometric parameters of the tool that can be varied are the drill diameter  $D$ , helix angle  $\beta_0$ , chisel edge angle  $\omega'$ , and chisel edge width  $W'$ . The cutting and vibration conditions that can be varied are the spindle speed  $n$ , feed rate  $F$ , vibration frequency  $f$ , and vibration amplitude  $A$ .

The presented model incorporates the analysis of instantaneous uncut chip thickness, instantaneous cutting angles that are both dependent on time and location of the drill, material shear strength at the current state of strain and strain rate, and the plowing force that results from axially vibrating the tool on an uneven machined surface. By incorporating all of the above analyses, a model closely representing the actual conditions of VAD has been developed.

Because of the dynamic nature of VAD, thrust force can be negative (*i.e.* the direction of the thrust force changes from downward to upward). A method for determining this critical vibration condition was presented. In Chapter 5, it will be shown that this critical vibration condition has important implications for the final burr height.

## CHAPTER 4

### BURR HEIGHT MODELING FOR VAD

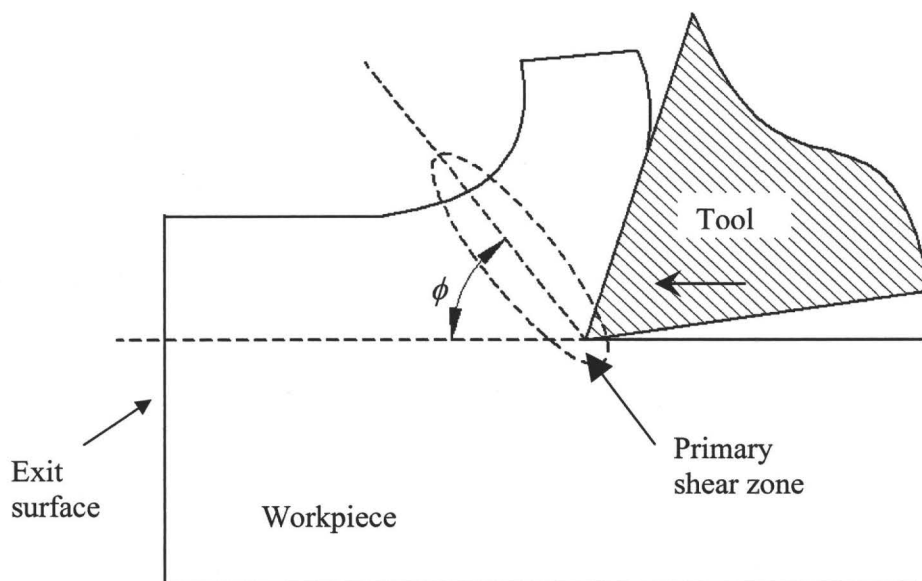
#### 4.1 INTRODUCTION

With the model for predicting thrust force now defined, as presented in Chapter 3, modeling burr formation and predicting the resultant burr height under different tool geometries, cutting conditions, and vibration conditions becomes possible. Being able to estimate burr height accurately for VAD under different cutting and vibration conditions is important because a poor choice of vibration conditions can result in a larger burr height compared to conventional drilling, while a proper choice of vibration conditions can produce burrs with a smaller height. This thesis only addresses the prediction of exit burr height because the exit burr is usually significantly larger than the entrance burr. While burr size is determined by both its height and width, for most applications burrs that are large in width but small in height are acceptable, while burrs with a small width but large height will present problems in fit, form, and function of the component. In this chapter, the development of an exit burr height model for VAD is presented. Recall that the definition of exit burr height and width was presented in Figure 1.3 in Chapter 1.

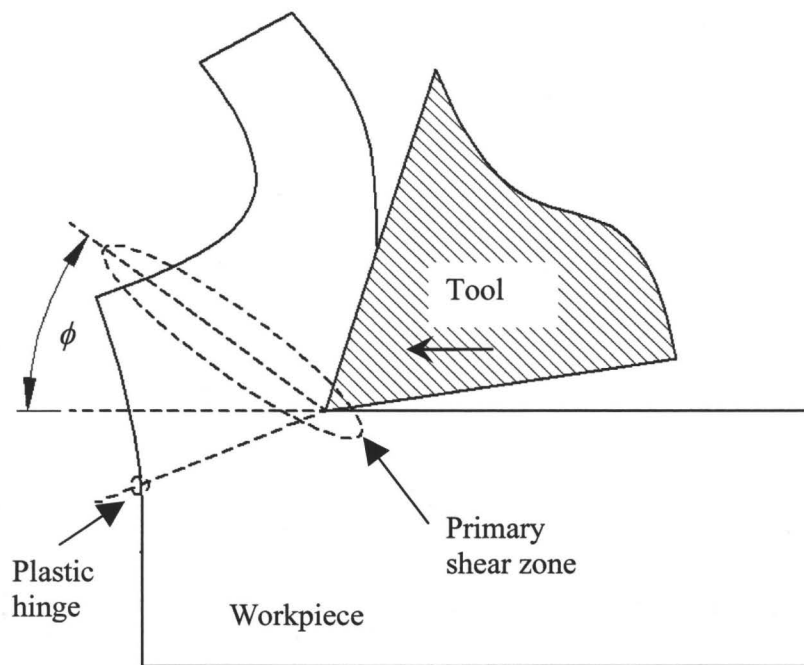
## 4.2 EXIT BURR HEIGHT MODEL FOR VAD

### 4.2.1 Exit burr in drilling

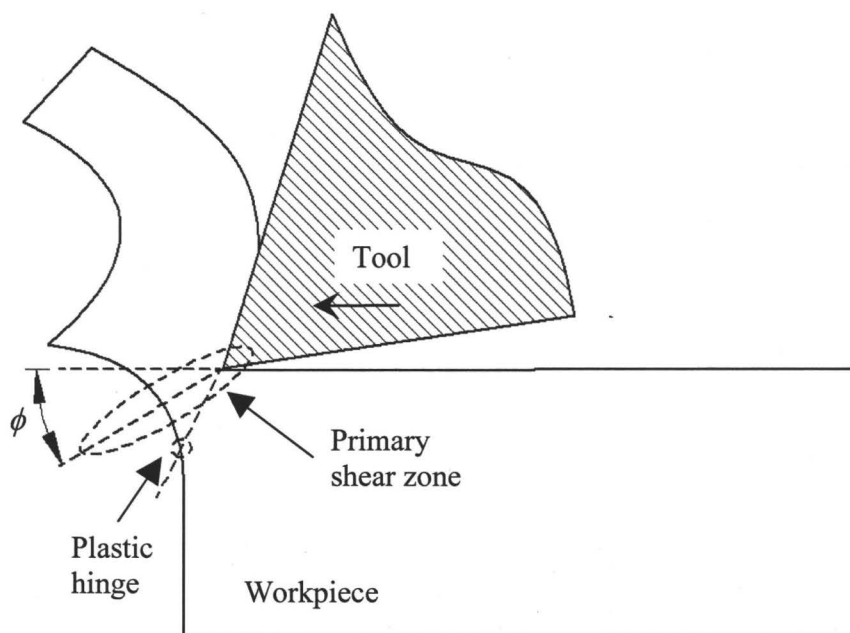
Exit burr is commonly defined as the deformation of workpiece material on the surfaces where the cutting tool exits the workpiece. Figure 4.2.1 illustrates the formation of an exit burr when the tool approaches the exit surface. This type of burr is defined as a roll-over burr and is characterized by the rotation of the primary shear zone about a plastic hinge at the exit surface, forming a negative shear angle.



a) Tool initially cutting material with positive shear angle.



b) When the tool gets close to the exit surface, the primary shear zone begins to rotate.



c) The primary shear zone continues to rotate and forms a negative shear angle.

**Figure 4.2.1. Formation of an exit burr as the tool approaches the exit surface.**

However, while an exit burr in drilling also occurs at the exit surface of the workpiece material along the path of the drill, its characteristics are slightly different from those presented above. Because the effective tool path of a cutting edge element on a drill is not perpendicular to the exit surface, the primary shear zone does not rotate about the plastic hinge. Although the exit burr in drilling is still defined as a roll-over burr, the burr formation mechanism changes significantly. Accurately determining all the instantaneous cutting angles presented in Chapter 3 after burr formation begins becomes highly complicated. Fortunately, burr formation is a highly stochastic phenomenon, and including all the factors affecting burr formation in the model does not guarantee accurate results. Instead, a simplified approach, based on Kim and Dornfeld's exit burr model [22] with a careful model calibration process will be used in this thesis. Comparison between the model predictions and experimental results in Chapter 5 will show that this approach improves Kim and Dornfeld's model by up to 36%.

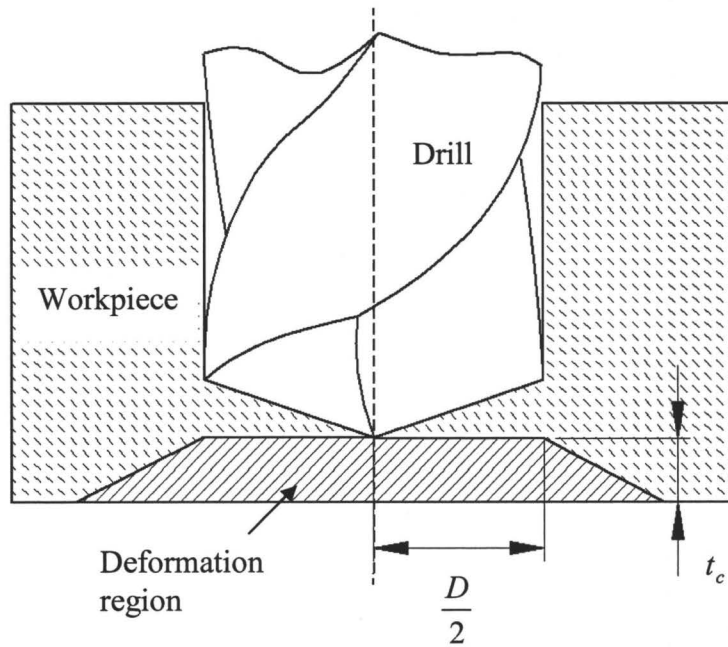
#### **4.2.2 Determining the critical material thickness using Kim and Dornfeld's model**

Kim and Dornfeld's [22] burr height model was discussed in Section 2. Because the proposed burr height model is primarily based on Kim and Dornfeld's model, the details of their model will be presented in this section. The Kim and Dornfeld model assumes the effects of temperature, strain rate, and tool wear are negligible. Burr formation begins when the work done by the cutting force in the feed direction (thrust force)  $\Delta W_t$  exceeds the work required to plastically deform the material under the drill,  $\Delta W_d$ .  $\Delta W_d$  is dependent on the material properties and the thickness of the material

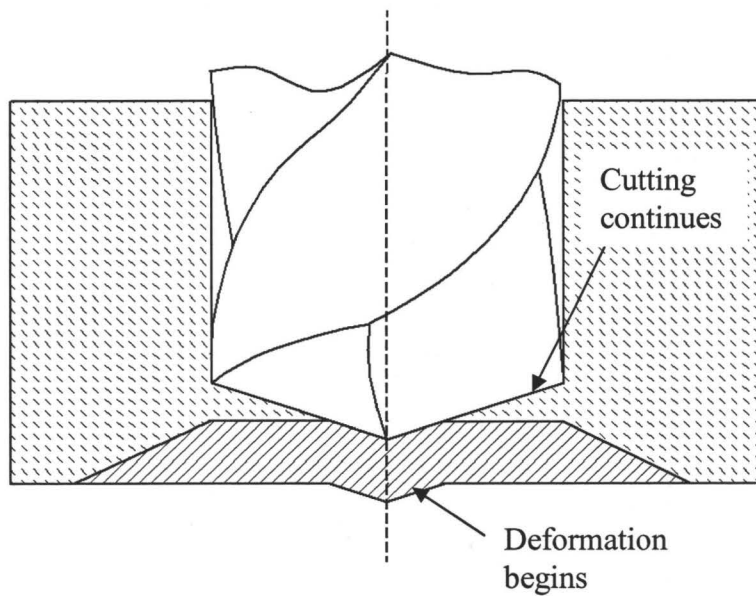
under the drill. The material thickness where burr formation begins is defined as the critical material thickness ( $t_c$ ).

Figure 4.2.2 illustrates the proposed burr formation mechanism. As the drill advances toward the exit surface, part of the material starts to deform. The deformation is assumed to be constrained within the shaded area, in the form of a disc. Once material deformation starts, it is assumed that no more cutting occurs in the shaded region. The deformation continues until fracture occurs at the outer perimeter of the drill. The burr is left after the deformation and fracture have completed (Figure 4.2.2e). With this assumption, once deformation begins in the centre of the drill, part of the material under the drill near the outer cutting edge region is still being cut. Therefore, between the initial stage of the deformation (Figure 4.2.2a) and the final deformation stage (Figure 4.2.2d), both cutting and deformation occur simultaneously. Within these stages, it is assumed that the total work done  $\Delta W_{Total}$  by the thrust force and the deformation remains constant:

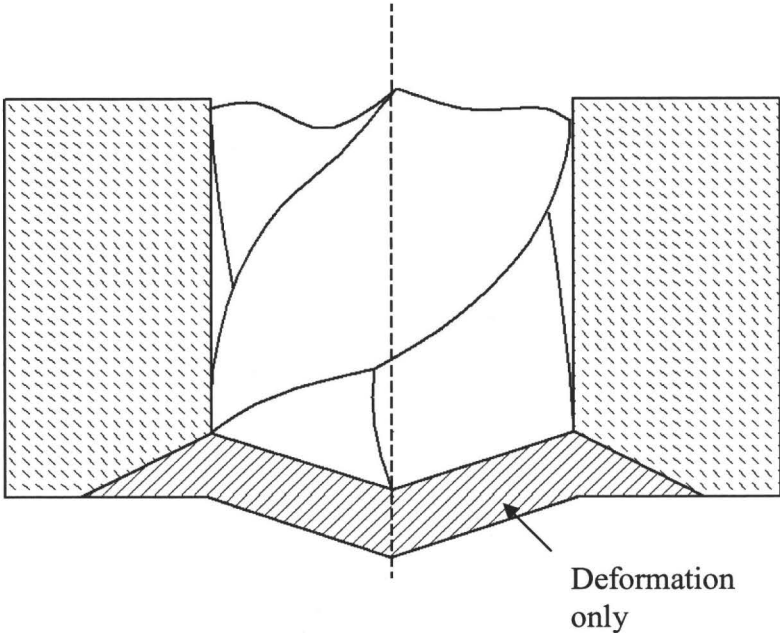
$$\Delta W_t + \Delta W_d = \Delta W_{Total} . \quad (4.2.1)$$



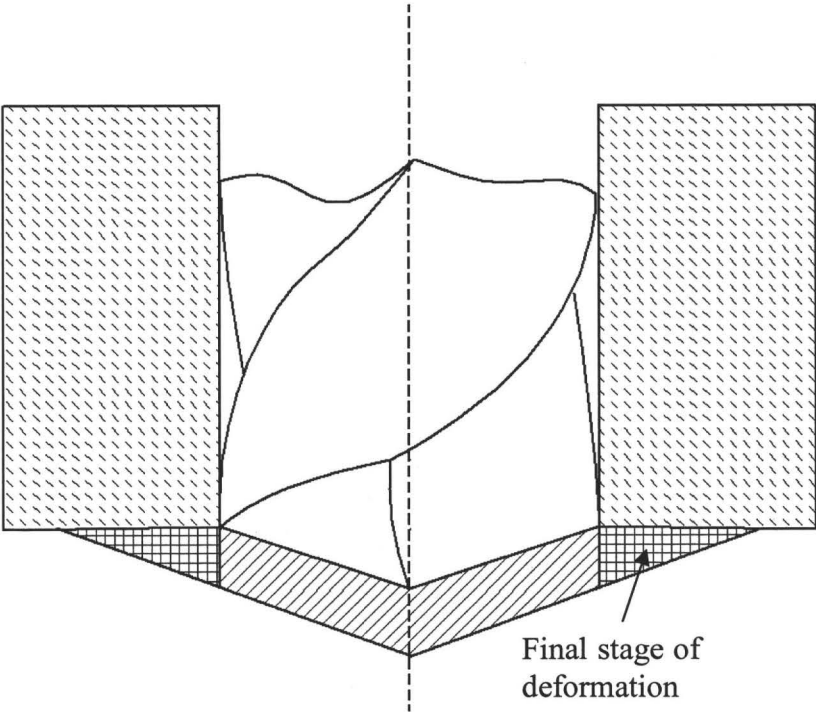
a) Deformation is assumed to be localized in the shaded region.



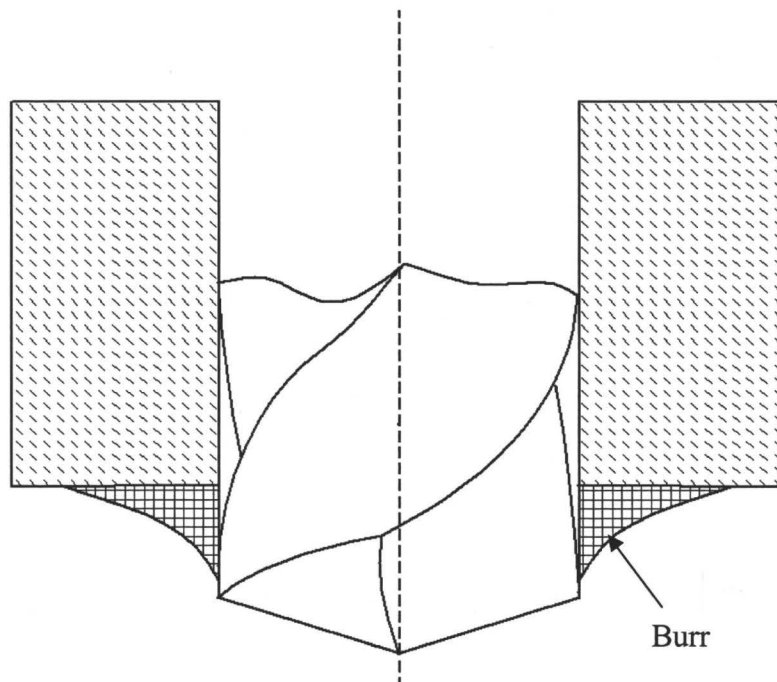
b) Deformation begins, while cutting still continues in the outer part of the material.



c) All work produced by the drill occurs as deformation.



d) Deformation occurs only at the outer periphery of the shaded region.



- e) Deformation has finished and fracture has occurred at the periphery of the drill, leaving the exit burr.

**Figure 4.2.2. Burr formation mechanism.**

Figure 4.2.3 shows a typical measurement of drilling thrust force. The final stage where the thrust force begins to decrease is assumed to be where the initial deformation stage begins. Since  $\Delta W_{Total}$  is assumed to be constant, it equals the product of the steady state averaged thrust force  $\bar{F}_{th}$  (averaged over the time span of stage (a) in Figure 4.2.3) and the total axial displacement that the drill traveled from stage (b), where deformation begins to occur, to stage (d), where the outer edge of the cutting lips reached the exit surface of the workpiece.  $\Delta W_{Total}$  can therefore be expressed as:

$$\Delta W_{Total} = \bar{F}_{th} \left( t_c + \frac{D}{2 \tan p} \right). \quad (4.2.2)$$

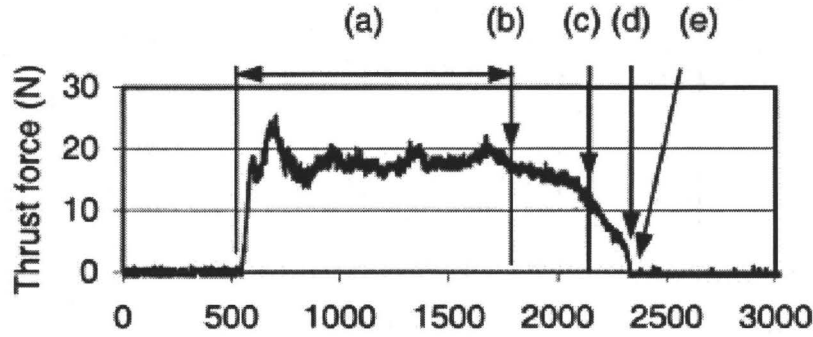


Figure 4.2.3. Typical measurement of drilling thrust force (taken from [22]).

To model  $\Delta W_t$ ,  $F_{th}$  between stage (b) and (d) must first be determined. Although it is possible to model the work done by the drilling thrust force using computer simulations, a second-order approximation used in Kim and Dornfeld's model is proposed for modeling the thrust force between these two stages to reduce simulation time:

$$F_{th}(z) = \bar{F}_{th} \left\{ 1 - \frac{z^2}{\left[ t_c + \frac{D}{2 \tan p} \right]^2} \right\}. \quad (4.2.3)$$

Therefore,  $\Delta W_t$  can be expressed as:

$$\Delta W_t = \int_0^L F_{th}(z) dz = \bar{F}_{th} \int_0^L \left( 1 - \frac{z^2}{L^2} \right) dz, \text{ where } L = \left( t_c + \frac{D}{2 \tan p} \right). \quad (4.2.4)$$

To determine  $\Delta W_d$ , the shaded region shown in Figure 4.2.2 is modeled as a circular thin plate deformed into a circular cone shell. Figure 4.2.4 shows the proposed model of half of the cross-section of the material under the drill before and after the deformation

(polygon  $agcd$  is deformed into  $egbh$ ). The deformation is assumed to consist of material elongation (from  $abcd$  to  $hbck$ ), followed by the bending of  $bc$  to  $bj$ . The work required to deform  $\Delta cbg$  to  $\Delta bjg$  is assumed to be negligible. The total work required to complete the deformation equals the sum of the work required for the elongation  $\Delta W_e$  and the work required for the bending  $\Delta W_b$ :

$$\Delta W_d = \Delta W_e + \Delta W_b \tag{4.2.5}$$

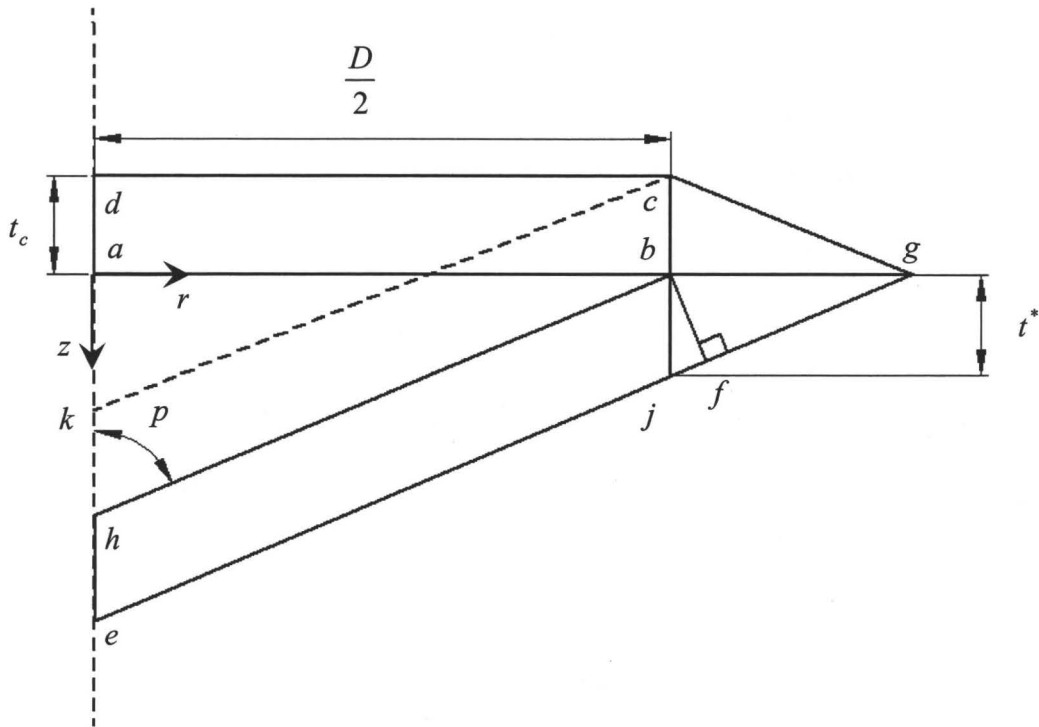


Figure 4.2.4. Deformation of material under the drill.

$\Delta W_e$  can be determined by first calculating the total strain along  $ab$ ,  $\epsilon_{ab}$ :

$$\epsilon_{ab} = \ln \left[ \frac{\frac{D}{2 \sin p} + \overline{jf}}{\frac{D}{2}} \right] = \ln \left[ \frac{1}{\sin p} \left( 1 + \frac{2t_c}{D} \sin^2 p \cos p \right) \right]. \tag{4.2.6}$$

For a circular thin plate, the strain distribution along  $ab$  is not uniform but a function of radial distance from the centre. The strain distribution is assumed to have the form of a second-order polynomial:

$$\varepsilon_{ab}(r) = \frac{3}{2} \left( 1 - \frac{4r^2}{D^2} \right) \ln \left[ \frac{1}{\sin p} \left( 1 + \frac{2t_c}{D} \sin^2 p \cos p \right) \right] . \quad (4.2.7)$$

Therefore,

$$\Delta W_e = \int_V \sigma_y \varepsilon_{ab}(r) dV = \frac{3}{16} \pi D^2 \sigma_y t_c \sin p \ln \left[ \frac{1}{\sin p} \left( 1 + \frac{2t_c}{D} \sin^2 p \cos p \right) \right] . \quad (4.2.8)$$

Because  $\frac{2t_c}{D} \sin^2 p \cos p \ll 1$ :

$$\ln \left( 1 + \frac{2t_c}{D} \sin^2 p \cos p \right) \approx \left( \frac{2t_c}{D} \sin^2 p \cos p \right) . \quad (4.2.9)$$

Therefore,

$$\Delta W_e \approx \frac{3}{16} \pi D^2 \sigma_y t_c \sin p \left[ \ln \left( \frac{1}{\sin p} \right) + \frac{2t_c}{D} \sin^2 p \cos p \right] . \quad (4.2.10)$$

$\Delta W_b$  can be found by the following equation:

$$\Delta W_b = M_b \Delta \theta , \quad (4.2.11)$$

where  $M_b$  is the required bending moment, and  $\Delta \theta$  is the resultant change in angle, and:

$$M_b = \frac{1}{4} \pi \sigma_y D t_c^2 \quad (4.2.12)$$

$$\Delta \theta = \left( \frac{\pi}{2} - p \right) , \quad (4.2.13)$$

and therefore,

$$\Delta W_b = \frac{1}{4} \pi \sigma_y D t_c^2 \left( \frac{\pi}{2} - p \right). \quad (4.2.14)$$

Substituting equations (4.2.2), (4.2.4), (4.2.5), (4.2.10), and (4.2.14) into (4.2.1),  $t_c$  can be solved by:

$$t_c = \frac{\left( \frac{1}{3} F_{th} - C_1 C_2 \right) + \sqrt{\left( C_1 C_2 - \frac{1}{3} F_{th} \right)^2 + \frac{2D(C_1 C_3 + C_4)}{3 \tan p}}}{2(C_1 C_3 + C_4)}, \quad (4.2.15)$$

$$\text{where } C_1 = \frac{3}{16} \pi D^2 \sin p, \quad (4.2.16)$$

$$C_2 = \ln \left( \frac{1}{\sin p} \right), \quad (4.2.17)$$

$$C_3 = \frac{2 \sin^2 p \cos p}{D}, \text{ and} \quad (4.2.18)$$

$$C_4 = \frac{1}{4} \pi \sigma_y \left( \frac{\pi}{2} - p \right) D. \quad (4.2.19)$$

After determining  $t_c$ , the final burr height  $H$  can be obtained analytically. Figure 4.2.5 shows the schematic of the final burr formation. The shaded area represents the final burr shape. Referring to Figure 4.2.4,  $t^*$  can be found by conservation of volume before and after the deformation:

$$\text{Volume } abcd = \overline{ab} \times \overline{bc} = \overline{ab} \times t_c, \quad (4.2.20)$$

$$\text{Volume } hejb = \overline{ab} \times \overline{jb} = \overline{ab} \times t^*, \quad (4.2.21)$$

$$\text{Volume } abcd = \text{Volume } hejb, \quad (4.2.22)$$

$$\therefore t^* = t_c. \quad (4.2.23)$$

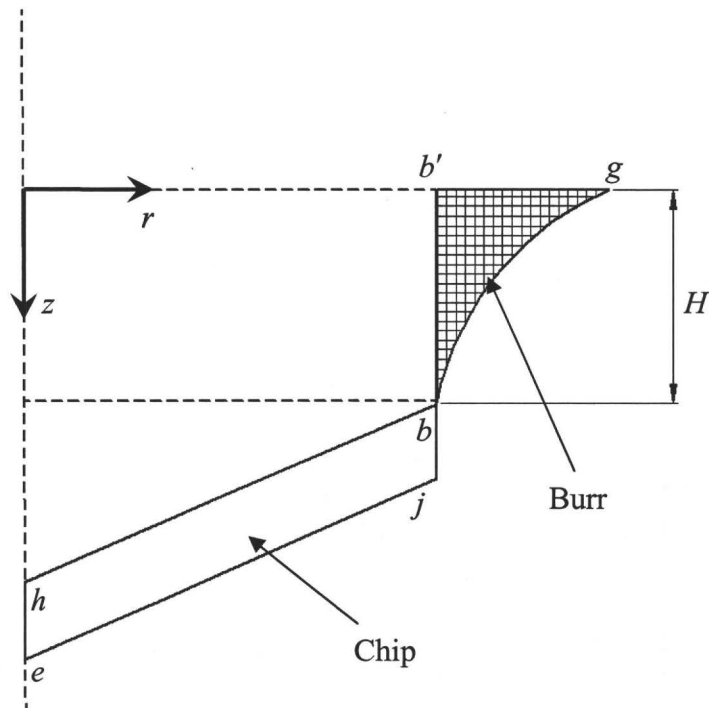


**Figure 4.2.5. Final burr formation.**

The final burr fracture is assumed to be a tensile fracture of material. Assuming perfect plastic material behavior, fracture occurs when the plastic strain  $\varepsilon_p$  equals the fracture strain of the material  $\varepsilon_f$ :

$$\varepsilon_p = \varepsilon_f . \quad (4.2.24)$$

$\varepsilon_p$  and  $\varepsilon_f$  at the periphery of the hole can respectively be expressed as:

$$\varepsilon_p = \frac{2}{\sqrt{3}} \ln\left(\frac{H}{t^*}\right) = \frac{2}{\sqrt{3}} \ln\left(\frac{H}{t_c}\right) \text{ and} \quad (4.2.25)$$

$$\varepsilon_f = \ln\left(\frac{100}{100 - \%R.A.}\right), \quad (4.2.26)$$

where %R.A. is the percentage reduction in area of the material at tensile fracture.

Solving for  $H$  from equations (4.2.24) to (4.2.26) gives:

$$H = t_c \exp \left[ \frac{\sqrt{3}}{2} \ln \left( \frac{100}{100 - \%R.A.} \right) \right]. \quad (4.2.27)$$

### 4.2.3 Proposed burr height model

Kim and Dornfeld's model uses the estimated total thrust force to determine  $t_c$ . However, in Section 3.3, the thrust force is shown to vary with time for VAD. To calculate  $t_c$  using Kim and Dornfeld's model, the time-averaged value of the thrust force can be used. In Section 3.3.4, it was shown that the thrust force for VAD can reach negative values, which can reduce the time-averaged value of the thrust force. However, exit burr formation is caused by the tool pushing down onto the workpiece material, *i.e.* by producing a thrust force pointing downward and plastically deforming the workpiece material. A negative thrust force value represents a thrust force that is pointing upward, which will not cause burr formation on the exit surface. Therefore, considering this the overall averaged thrust force will underestimate  $t_c$ . In this thesis, it is hypothesized that only the positive portion of the thrust force contributes to burr formation. Equation (3.3.21) is replaced with:

$$\bar{F}_{th}^+ = \frac{1}{T^+} \int_0^T F_{th}^+ dt \quad (4.2.28)$$

where:

$$F_{th}^+ = \begin{cases} F_{th} & \text{if } F_{th} > 0 \\ 0 & \text{otherwise} \end{cases}, \quad (4.2.29)$$

$$T^+ = \int_0^T x dt, \text{ and} \quad (4.2.30)$$

$$x = \begin{cases} 1 & \text{if } F_{th} > 0 \\ 0 & \text{otherwise} \end{cases}. \quad (4.2.31)$$

Kim and Dornfeld's model also assumes perfectly plastic material properties. In equation (4.2.24), only plastic strain is used to determine the strain on the material around the periphery of the hole. However, the total strain equals the sum of plastic strain  $\varepsilon_p$  and elastic strain  $\varepsilon_e$ :

$$\varepsilon_T = \varepsilon_p + \varepsilon_e = \frac{2}{\sqrt{3}} \ln \left( \frac{H}{t_0 \sin p} \right) + \varepsilon_e. \quad (4.2.32)$$

With this observation, the burr height  $H$  should be modeled as:

$$H = t_c \exp \left\{ \frac{\sqrt{3}}{2} \left[ \ln \left( \frac{100}{100 - \%R.A.} \right) - \varepsilon_e \right] \right\}. \quad (4.2.33)$$

Next, it is necessary to determine the elastic strain  $\varepsilon_e$ . After burr formation begins, it is assumed that no chip formation occurs, therefore the drilling process will behave similar to a forming process. The material spring back theory used in forming process analysis [57] is proposed to determine the elastic strain  $\varepsilon_e$  as follows:

$$\varepsilon_e = \frac{\sigma}{E} = \frac{F_a}{ES^*}, \quad (4.2.34)$$

where  $F_a$  is the applied force,  $E$  is the elastic modulus, and  $S^*$  is the cross-sectional area of the material before unloading and is calculated by [57]:

$$S^* = \frac{S(1 - \varepsilon_e)}{1 - (1 - 2\nu)\varepsilon_e}, \quad (4.2.35)$$

where  $S$  is the cross-sectional area of the material after unloading (*i.e.* the cross-sectional area of the resultant burr), and  $\nu$  is Poisson's ratio. Referring to Figure 4.2.4 and Figure 4.2.5,  $S$  can be approximated as the area of a triangle:

$$S \approx \frac{1}{2} H \times \overline{b'g} = \frac{1}{2} H t_c \tan p . \quad (4.2.36)$$

$\varepsilon_e$  can then be modeled by substituting equation (4.2.31) into equation (4.2.30) and replacing  $F_a$  by  $\overline{F}_{th}^+$ :

$$\varepsilon_e = \frac{\overline{F}_{th}^+}{E} \left[ \frac{1 - (1 - 2\nu)\varepsilon_e}{S(1 - \varepsilon_e)} \right] . \quad (4.2.37)$$

Equations (4.2.33), (4.2.36), and (4.2.37) together form a system of equations that cannot be solved analytically. By solving this system of equations numerically using Newton's method,  $H$  can be accurately predicted.

### 4.3 PREDICTING THE FAVOURABLE VIBRATION FREQUENCY

In our previous work [34 & 35] we showed that a favourable vibration condition that produces the smallest burr height exists for VAD. In contrast to Takeyama and Kato's theory [27], maximum burr height reduction does not exist at the maximum achievable vibration frequency and/or amplitude (which are limited by the actuation system). Determining this favourable vibration condition is important to maximize the effect of burr reduction with minimal vibration effort. In this thesis, the vibration amplitude is fixed at 0.002 mm due to the limitation of the experimental setup. The goal is to determine the favourable vibration frequency for this or any given amplitude.

One approach for finding this frequency is to run many simulations using the equations presented above. However, an analytical approach should significantly reduce the computation time. Therefore, it is desirable to determine the thrust force and work analytically. In the thrust force model presented in Chapter 3, the dynamic normal rake angle  $\gamma_{nd}$  is computed by solving a system of four equations with four unknowns. However, by studying the system of equations, it is found that:

$$\gamma_{nd} \approx \eta_d . \quad (4.3.1)$$

For example, Figure 4.3.1 shows the relationship between  $\gamma_{nd}$  and  $\eta_d$  for a one-vibration cycle at 12 kHz. With this approximation, the principal forces become a function of  $\eta_d$ , which can be easily computed by equation (3.2.22).

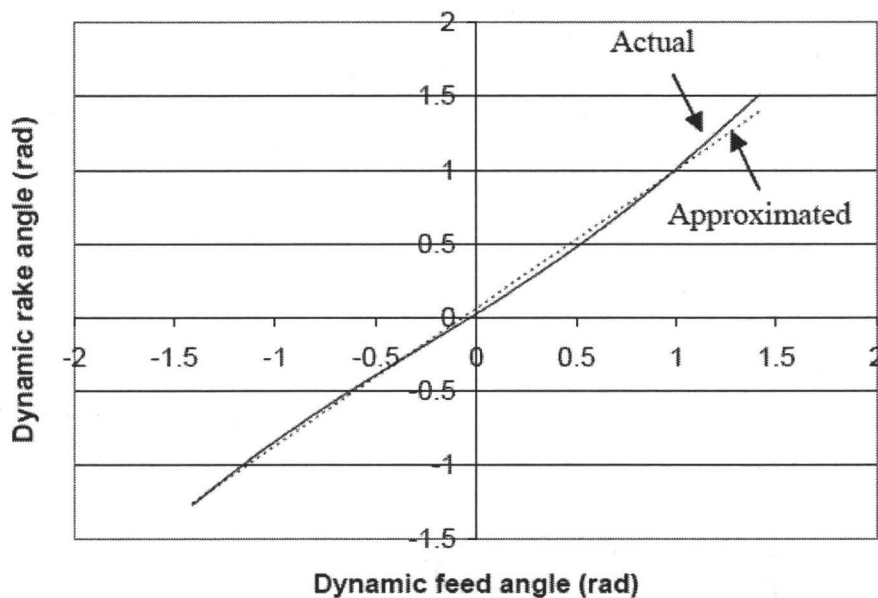


**Figure 4.3.1. Comparison between actual and approximated relationship between**

$\gamma_{nd}$  **and**  $\eta_d$ .

Burr height is minimized when the total work done by the thrust force acting on the workpiece is minimized. Therefore, to determine the favourable vibration frequency, work done by thrust force (along the axial direction) of VAD must be analyzed. The work done along the axial direction per vibration cycle  $W_t$  is:

$$W_t = \int_0^{\bar{z}_0} dW_t = \int_0^{\bar{z}_0} F_{th} dz , \quad (4.3.2)$$

where  $dW_t$  is the differential work done with respect to the displacement and  $\bar{z}_0$  is the resultant axial displacement after one vibration cycle and can be calculated by:

$$\bar{z}_0 = FnT , \quad (4.3.3)$$

where  $T$  is the period of vibration. To simplify the mathematical computation, the vibration can be approximated using a triangular wave.  $z(t)$  is then the triangular wave superimposed on the axial feed. An exaggerated example is shown in Figure 4.3.2.

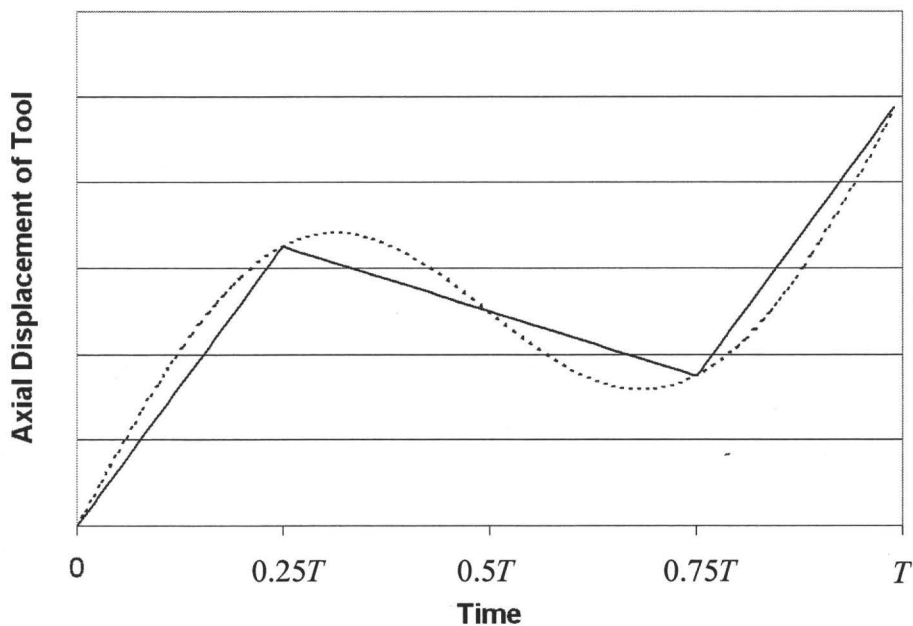


**Figure 4.3.2: Example of an approximated axial displacement of the drill.**

The axial velocity,  $z(t)$ , can then be expressed as:

$$dz = \begin{cases} (4fA + Fn)dt & 0 \leq t < \frac{1}{4f} \\ (-4fA + Fn)dt & \frac{1}{4f} \leq t < \frac{3}{4f} \\ (4fA + Fn)dt & \frac{3}{4f} \leq t < \frac{1}{f} \end{cases} . \quad (4.3.4)$$

Transforming the dependent variable from  $z$  to  $t$ , equation (4.3.2) becomes:

$$W_i = \int_0^{T/4} (4fA + Fn)F_{th}dt + \int_{T/4}^{3T/4} (-4fA + Fn)F_{th}dt + \int_{3T/4}^T (4fA + Fn)F_{th}dt . \quad (4.3.5)$$

The work done by cutting element  $i$  equals:

$$W_{t,i} = \int_0^{T/4} (4fA + Fn)\Delta P_i dt + \int_{T/4}^{3T/4} (-4fA + Fn)\Delta P_i dt + \int_{3T/4}^T (4fA + Fn)\Delta P_i dt . \quad (4.3.6)$$

Because  $T$  varies with frequency, to compare work done by one cutting element at a different vibration frequency, the normalized work done is introduced:

$$\bar{W}_{t,i} = \frac{W_{t,i}}{Z_0} . \quad (4.3.7)$$

Equation (4.3.7) represents the work done to the workpiece produced by one cutting element per unit axial depth of cut for any element  $i$ . Assuming  $\Delta P_i$  varies linearly with  $i$ ,  $\bar{W}_{t,i}$  will vary linearly with  $i$ . Therefore, the  $\bar{W}_{t,i}$  of the middle element of the cutting lip represents the averaged value of  $W_i$ , and the vibration frequency that minimizes  $\bar{W}_{t,i}$  for the middle element of the cutting lip is the favourable vibration frequency.

Using the approximation of  $\gamma_{nd}$  described in equation (4.3.1),  $\Delta P_i$ , the elemental thrust force, can be expressed in terms of  $\eta_d$ , which can be determined by equation

(3.2.27). Equation (3.2.27) can be further simplified by using equations (4.3.4). Therefore,

$\eta_d$  can be expressed as:

$$\eta_d = \begin{cases} \tan^{-1}\left(\frac{4fA + Fn}{2\pi rn}\right) & 0 \leq t < \frac{1}{4f} \\ \tan^{-1}\left(\frac{-4fA + Fn}{2\pi rn}\right) & \frac{1}{4f} \leq t < \frac{3}{4f} \\ \tan^{-1}\left(\frac{4fA + Fn}{2\pi rn}\right) & \frac{3}{4f} \leq t < \frac{1}{f} \end{cases}, \quad (4.3.8)$$

over the interval  $-\frac{\pi}{2} < \eta_d < \frac{\pi}{2}$ . With this approximation,  $\eta_d$  is independent of  $t$  within a specific range. Typically the vibration frequency and amplitude range from 1 kHz to 20 kHz and 0.004 mm to 0.015 mm respectively, while spindle speed and drill feed range from 115 rpm to 1350 rpm and 0.05 mm/rev to 0.08 mm/rev respectively in VAD [4, 24, 27, 33-35]. Under these conditions,  $4fA$  is at least ten times larger than  $Fn$ . Particularly for the present research,  $4fA$  is at least 32 times larger than  $Fn$ . Therefore:

$$\eta_d \approx \begin{cases} \tan^{-1}\left(\frac{2fA}{\pi rn}\right) & 0 \leq t < \frac{1}{4f} \\ \tan^{-1}\left(\frac{-2fA}{\pi rn}\right) & \frac{1}{4f} \leq t < \frac{3}{4f} \\ \tan^{-1}\left(\frac{2fA}{\pi rn}\right) & \frac{3}{4f} \leq t < \frac{1}{f} \end{cases}. \quad (4.3.9)$$

Denoting  $\tan^{-1}\left(\frac{2fA}{\pi rn}\right) = \eta_d^+$  and  $\tan^{-1}\left(\frac{-2fA}{\pi rn}\right) = \eta_d^-$ , equation (4.3.9) can be rearranged as:

$$4fA = 2\pi rn \tan(\eta_d^+) \quad (4.3.10)$$

$$\text{and} \quad -4fA = 2\pi rn \tan(\eta_d^-). \quad (4.3.11)$$

Combining equations (3.2.26), (4.3.1), (4.3.6), (4.3.7), and (4.3.9) to (4.3.11), the normalized work done can be found. Note that  $dW_t$  could be negative, and since negative work does not contribute to burr formation, all negative values of  $dW_t$  should be neglected. Taking all these conditions into account, the value of  $\bar{\eta}_d$  that minimizes  $\bar{W}_{t,i}$ , denoted as  $\bar{\eta}_d^*$ , may be rapidly found numerically. Then the favourable vibration frequency  $f^*$  with a known amplitude  $A$  is obtained using:

$$f^* = \frac{2\pi r n \tan \bar{\eta}_d^* - Fn}{4A} . \quad (4.3.12)$$

#### 4.4 CONCLUSIONS

This chapter presented the analysis and modeling of burr height for VAD. The proposed model, which is based on Kim and Dornfeld's burr model, assumed no cutting occurs once burr formation begins. With this assumption and by determining the work required for chip formation and that for plastic deformation, the critical thickness of the material under the drill where burr formation begins as well as the final burr height can be determined. The model also incorporates the hypothesis that only the positive portion of the thrust force contributes to burr formation and included elastic spring back of the workpiece material to provide more accurate burr height prediction.

An approach to determine the favourable vibration frequency has also been developed. The presented method uses simplified equations and reasonable approximations to simplify the mathematical calculations. Instead of running many

simulations, this method provides a rapid way to determine the favourable vibration frequency. A simple program was written to perform the calculations. The predictions for different cutting conditions will be presented and compared with an experimental study in Chapter 5.

## **CHAPTER 5**

### **EXPERIMENTAL STUDY OF VAD**

#### **5.1 INTRODUCTION**

In this chapter, various experimental studies on VAD will be presented. One set of controlled experiments will be used to calibrate the models presented in Chapters 3 and 4. The remaining results will be compared with the model predictions. The accuracy of the developed method to determine the favourable vibration frequency will also be verified.

#### **5.2 EXPERIMENTAL SETUP**

Experiments were carried out with the previously developed VAD system. The system consists of a vibration workpiece holder and the polarity switching drive circuit. Vibrating the workpiece instead of the tool, which is a common practice in vibration-assisted turning, has a few advantages for VAD. Designing a vibration-assisted tool holder for VAD is not trivial because of the connection needed between the rotating spindle and the external power source of the vibration actuator. Moreover, because of the length of the tool, vibrating the tool axially also potentially increases tool wobbling. By vibrating the workpiece, the relative displacement between the tool and the workpiece

remains unchanged, and this approach provides a simple design solution for small workpieces. It also reduces the potential for tool wobbling. A previously developed workpiece holder is driven by a piezoelectric stack actuator with a carefully designed compressive preload system to avoid overloading the actuator with tensile force [33]. A polarity switching drive circuit was developed to supply an oscillating voltage with sufficient power to the actuator and induce an axial vibratory motion to the workpiece. Table 5.2.1 summarizes the performance of the developed VAD system. Figure 5.2.1 and Figure 5.2.2 show the schematic and hardware photo of the vibration workpiece holder and polarity drive circuit, respectively. Details of the mechanical and electrical design of this hardware were presented in Chapter 5 of [33].

**Table 5.2.1. Mechanical specifications of the VAD hardware.**

Frequency Range (kHz)	Amplitude Range (mm)	Force Delivery (kN)
0-20	0-0.002	5

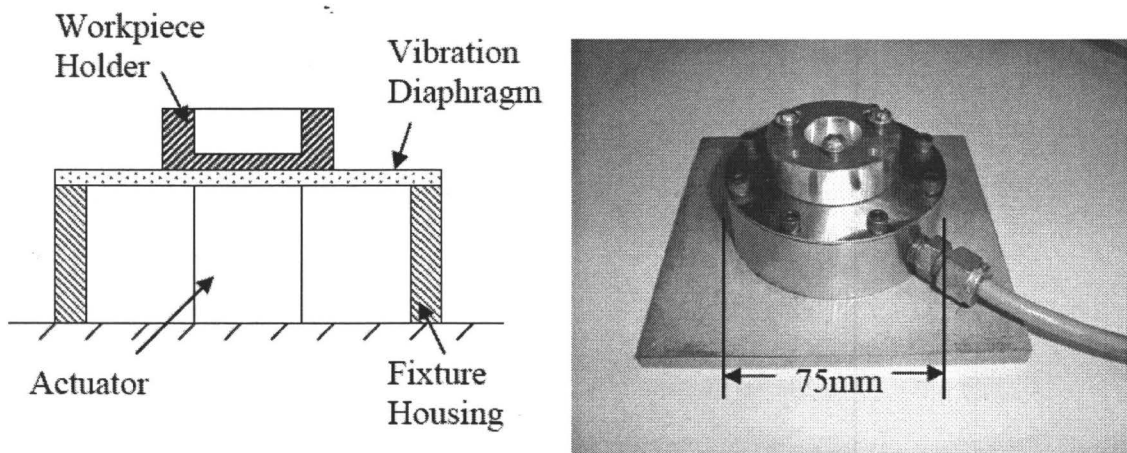


**Figure 5.2.1. Vibration workpiece holder.**

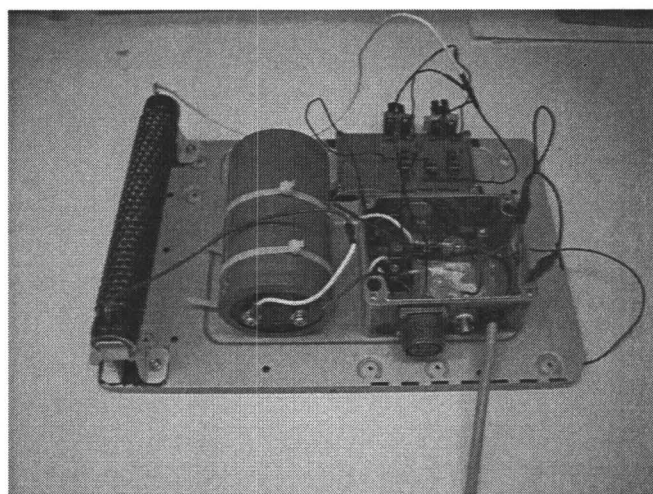
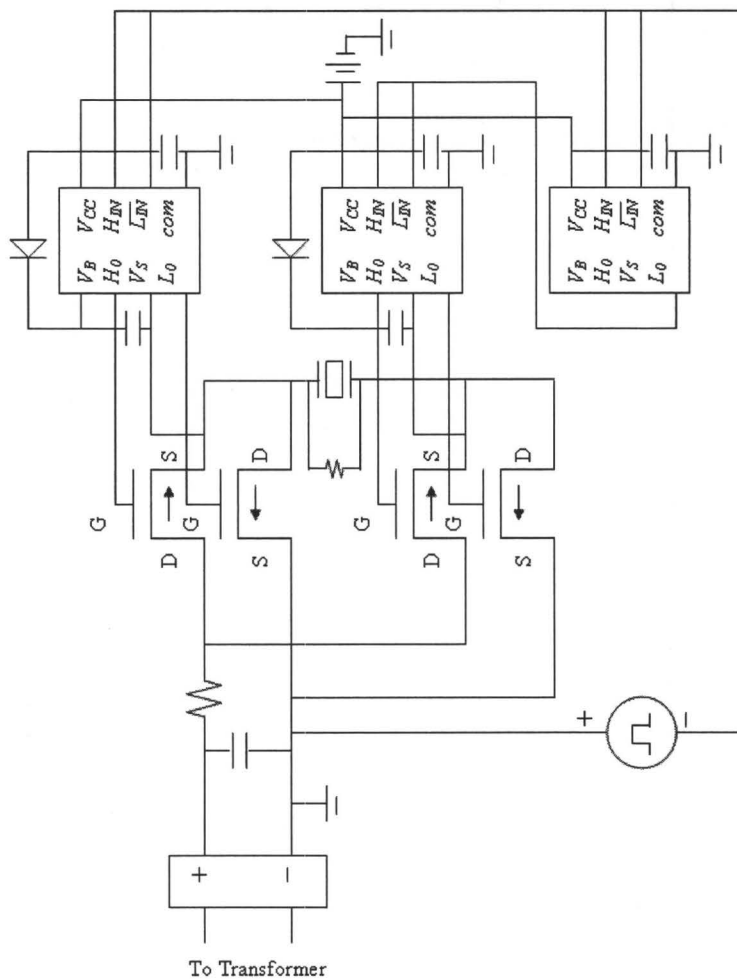
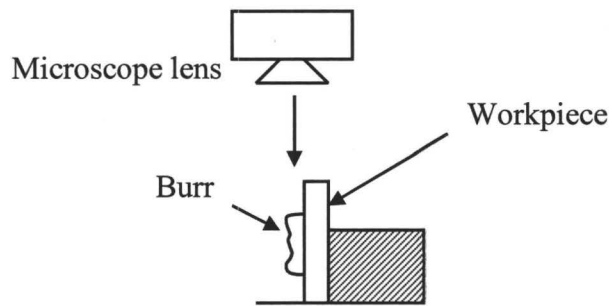


Figure 5.2.2. Polarity switching drive circuit.

Experiments were conducted with selected cutting and vibration conditions. Each test was performed on a horizontal CNC machine tool (Makino MC56-5XA), with the VAD system attached onto a Kistler Type 9255B table dynamometer, which was attached to the machine table. The maximum vibration amplitude of the VAD system is 0.002 mm. Since vibration amplitude lower than 0.002 mm has not been reported in the literature, the vibration amplitude was chosen to be 0.002 mm. Based on the author's previous research [33], the favourable vibration frequency for drilling aluminum with vibration amplitude of 0.002 mm occurs between 6 to 10 kHz. The vibration frequency was therefore chosen to vary from 4 to 12 kHz in 2 kHz increments. The drills used were TiN-coated standard twist drills. The workpieces were 3.18-mm thick Al 6061-T6 plates (25 mm x 25 mm). Five drilling experiments were performed for each cutting and vibration condition. A new drill was used for each set of five experiments. Force measurements were taken during the test by the table dynamometer with a sampling frequency of 120 kHz. Burr height was measured under four different views, using a tool-maker's microscope, as shown in Figure 5.2.3. The mean values of the thrust force and burr height for each cutting and vibration condition were calculated for subsequent comparison with the values of the corresponding model predictions. Figure 5.2.4 shows some examples of the tested workpiece. All photos were taken under the same scale. The tested conditions are summarized in Table 5.2.2.



**Figure 5.2.3. Measurement of burr height.**

**Table 5.2.2. Cutting and vibration conditions of the performed experiments.**

Test #	Sample #	Drill Dia. (mm)	Spindle Speed (rpm)	Feed (mm/s)	Vibration Freq. (kHz)	Vibration Amp. ( $\mu\text{m}$ )	Ave. uncut chip thickness (mm)
1	1-5	3.175	1000	1.90	0	2	0.114
2	6-10	3.175	1000	1.90	4	2	0.114
3	11-15	3.175	1000	1.90	6	2	0.114
4	16-20	3.175	1000	1.90	8	2	0.114
5	21-25	3.175	1000	1.90	10	2	0.114
6	26-30	3.175	1000	1.90	12	2	0.114
7	31-35	3.35	1300	1.30	0	2	0.060
8	36-40	3.35	1300	1.30	4	2	0.060
9	41-45	3.35	1300	1.30	6	2	0.060
10	46-50	3.35	1300	1.30	8	2	0.060
11	51-55	3.35	1300	1.30	10	2	0.060
12	56-60	3.35	1300	1.30	12	2	0.060
13	61-65	3.35	4000	1.00	0	2	0.015
14	66-70	3.35	4000	1.00	4	2	0.015
15	71-75	3.35	4000	1.00	6	2	0.015
16	76-80	3.35	4000	1.00	8	2	0.015
17	81-85	3.35	4000	1.00	10	2	0.015
18	86-90	3.35	4000	1.00	12	2	0.015
19	91-95	4	1000	1.00	0	2	0.060
20	96-100	4	1000	1.00	4	2	0.060
21	101-105	4	1000	1.00	6	2	0.060
22	106-110	4	1000	1.00	8	2	0.060
23	111-115	4	1000	1.00	10	2	0.060
24	116-120	4	1000	1.00	12	2	0.060

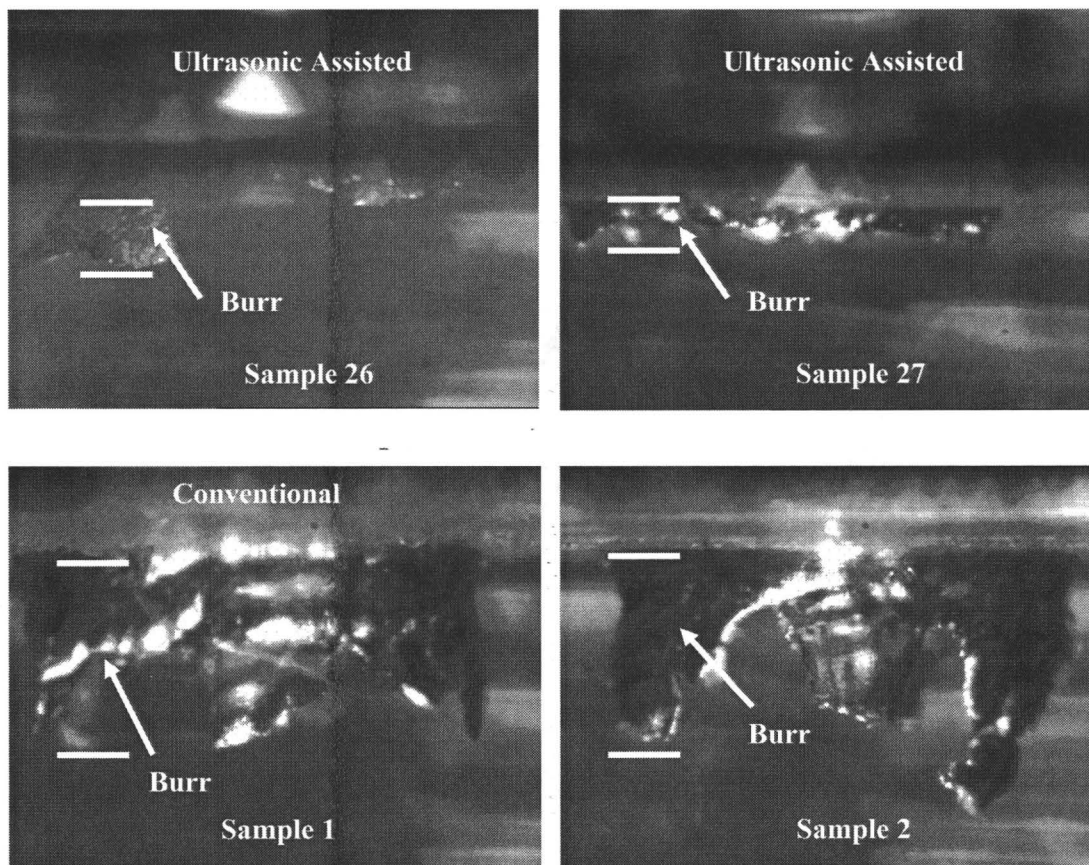


**Figure 5.2.4. Some examples of the machined workpiece.**

Tests 1–6 were used as a control set of experiments for model calibration purposes. Tests 7–12, 13–18, and 19–24 are three different groups of experiments, and the conditions were chosen to isolate the drill diameter, cutting speed, and average uncut chip thickness to determine their corresponding effect on the performance of VAD. These three factors are the governing factors affecting the thrust force and burr height for drilling aluminum. Although another governing factor is the material property, this study only addresses burr formation in drilling aluminum 6061-T6. Therefore, the same material was used for all the tests.

Results of the experiments, which will be presented later in sections 5.4 to 5.6, showed that if the vibration frequency is chosen correctly, VAD could reduce burr height. Within the tested vibration frequency, the favourable frequency was located at approximately 8 kHz. Both the model simulation and the method that rapidly predicts the favourable frequency (presented in Chapters 3 and 4) are consistent with this conclusion. However, to accurately predict the values of the mean thrust force and burr height, it is necessary to calibrate the model.

### 5.3 MODEL CALIBRATION

Tests 1–6 were used as a set of control experiments for model calibration. Table 5.3.1 summarizes the experimental results and the model prediction for the corresponding cutting and vibration condition.

**Table 5.3.1. Mean thrust force measurement for tests 1–6.**

Test #	1	2	3	4	5	6
Mean Thrust Force (N)	142.7	149.1	147.7	139.4	132.6	134.5

Figure 5.3.1 presents the comparison between experimental measurement (solid data points) and model predictions (hollow data points) before the calibration. The model consistently underestimated the mean thrust force, which is expected because the current model neglected the thrust force produced at the indented region of the drill. Because the indentation force  $P_i$  is very similar to the plowing force, it is assumed that  $P_i$  is proportional to the indented volume. Because the total indented volume for all vibration

conditions within each set of experiment remains the same, the indentation force for tests within the same set (tests 1–6 in this case) is equal to a constant.

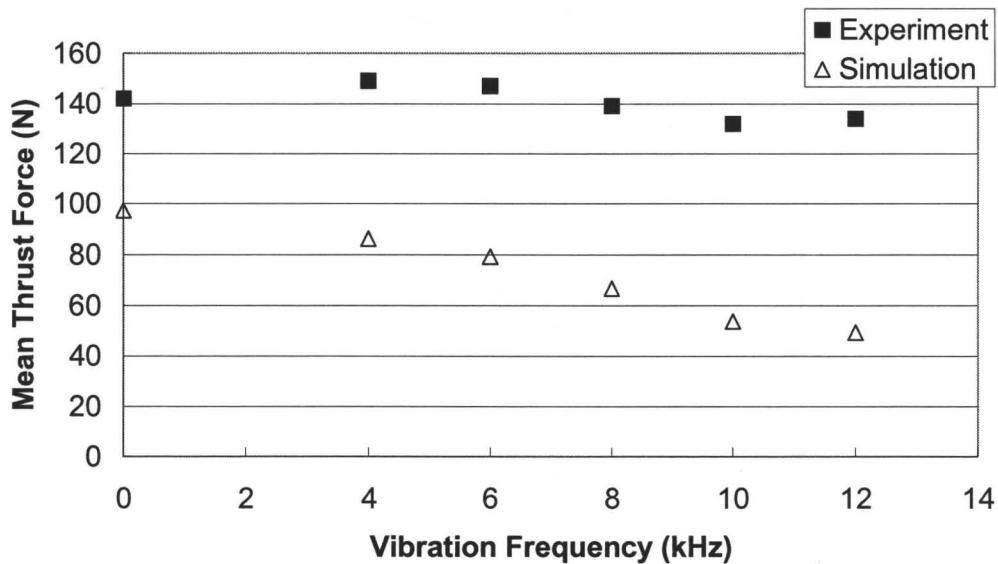


**Figure 5.3.1. Mean thrust force vs vibration frequency for tests 1–6 before calibration.**

Another observation is that the deviation between the model prediction and experiment measurement increases as the vibration increases. This contradicts the assumption that the indentation forces within tests 1–6 equal a constant. Calibration to the Johnson–Cook model is necessary. Equation (3.2.13) shows that  $\tau_i$  is related to the strain and strain rate through the constant terms  $A$ ,  $B$ ,  $m$ ,  $n$ ,  $\epsilon_0$ , and variable  $C$ . These parameters can be fine tuned with a least square curve-fitting algorithm, using equations (3.2.14) as a starting point. The objective is to fine tune the constants such that the deviation between the model predictions and experiment measurements remains as close to a constant as possible. Table 5.3.2 summarized the calibrated constants. Figure 5.3.2 shows the model

prediction with Johnson–Cook model calibration. The deviations between the model predictions and experimental measurements are now very close to a constant.

**Table 5.3.2. Model prediction of the mean strain and strain rate for tests 1–6.**

Parameters	Guo's constants	Calibrated constants
$A$	275	247.5
$B$	86	77.4
$m$	$-\infty$	$-\infty$
$n$	0.39	0.38
$\dot{\epsilon}_0$	1	3.07
$C$	$0.058-0.194h-0.003V$	$0.058-0.194h-0.003V$

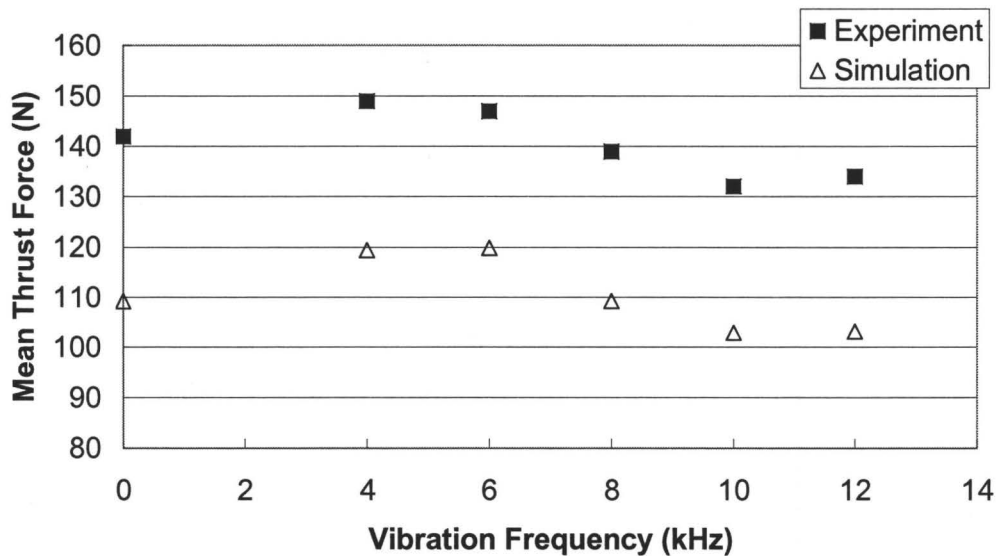


**Figure 5.3.2. Mean thrust force vs vibration frequency for tests 1–6 after calibration with Johnson-Cook model.**

The average difference between the experimental results and the model prediction is 38.0 N. Assuming  $P_i$  is proportional to the drill feed  $F$ , equation (5.3.1) can be used to calibrate the model for the indentation force:

$$P_i = \frac{38.0}{1.90} F \quad . \quad (5.3.1)$$

Figure 5.3.3 shows the comparison between the experimental results and the model with calibrations for the indentation force and the constant term used in the Johnson–Cook model. The calibrated model shows significant improvement and less than 5% error with the measurements from the control experiment.

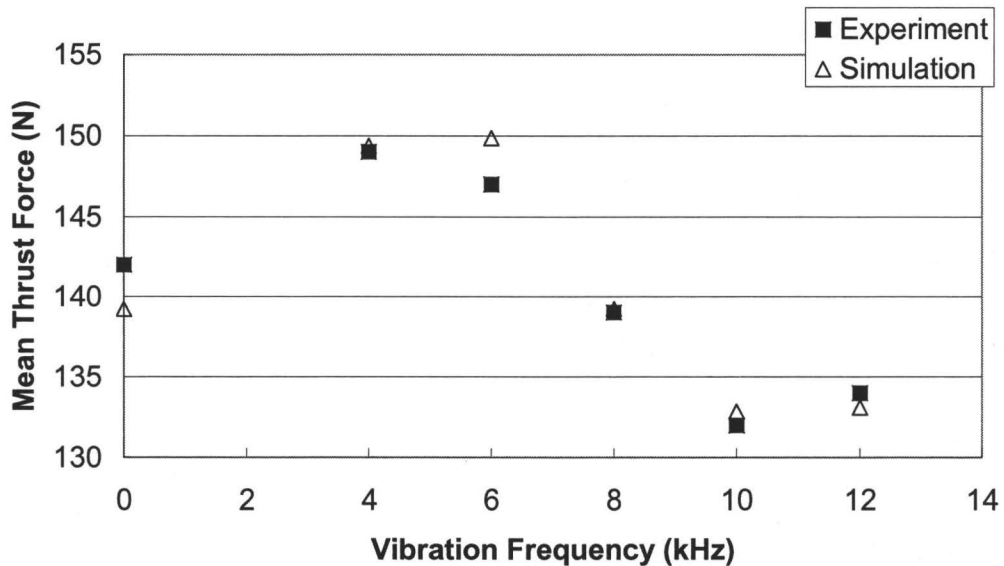


**Figure 5.3.3. Mean thrust force vs vibration frequency for tests 1– 6 for force model calibrated with Johnson-Cook model and indentation force.**

## **5.4 THRUST FORCE MODEL PREDICTION AND EXPERIMENTAL RESULTS**

The calibrated model was used to predict thrust force for tests 7–24. These predictions were compared with the experiment measurements. Table 5.4.1 summarizes

the comparison between the model predictions and the mean values of the experiment measurements.

**Table 5.4.1. Comparison between model prediction and experimental measurements.**

Test No.	Mean Thrust Force (N)	Model Prediction (N)	Deviation (%)
7	114.9	118.5	3.1
8	113.4	123.8	9.1
9	115.6	115.9	0.3
10	109.3	111.8	2.5
11	106.3	100.7	-5.3
12	107.0	97.4	-8.9
13	57.5	63.4	10.3
14	55.5	62.9	12.3
15	56.5	62.4	10.5
16	53.9	61.1	13.4
17	53.2	59.4	11.6
18	58.1	57.7	-0.5
19	127.1	134.4	5.8
20	137.3	127.6	-6.9
21	135.4	123.6	-8.4
22	114.9	122.4	6.5
23	106.8	109.0	1.9
24	109.1	113.0	3.7

The experimental mean thrust force results are compared with the corresponding simulation results in Figure 5.4.1–Figure 5.4.3. The solid data points represent simulation results using the calibrated model, and the hollow circular data points represent experimental data. The maximum deviation between experimental results and the simulations was 18%. Note that the experimental thrust force measurements averaged over each set of four tests fall within 13% of the simulation predictions.

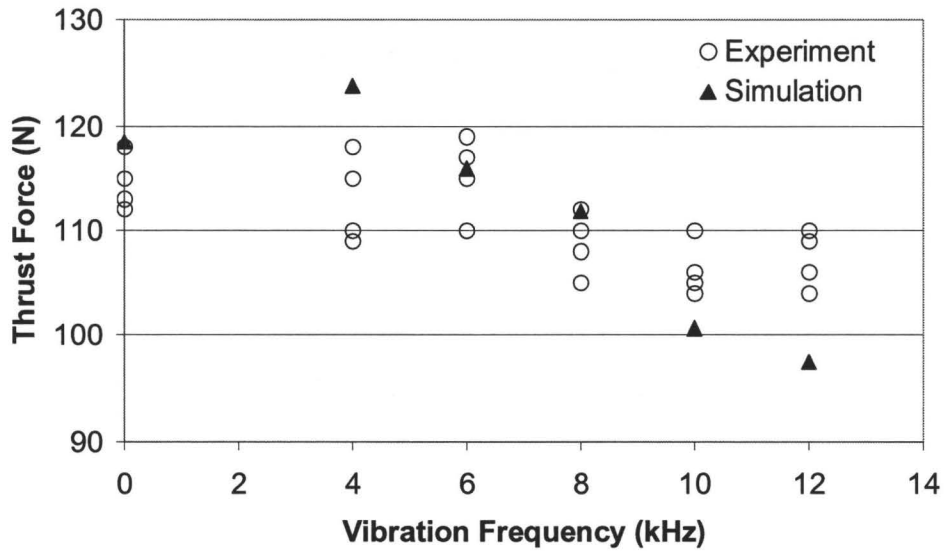


Figure 5.4.1. Simulations and experimental thrust force results for tests 7–12.

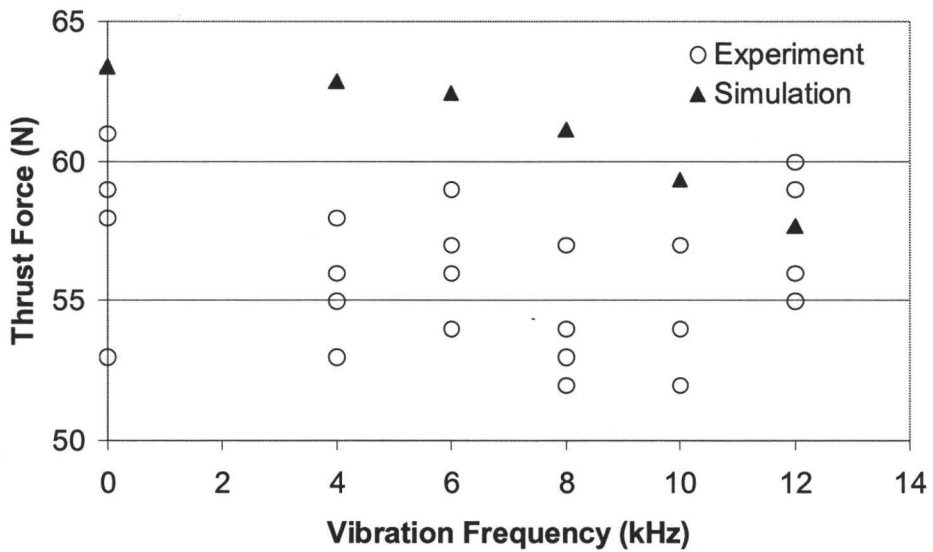
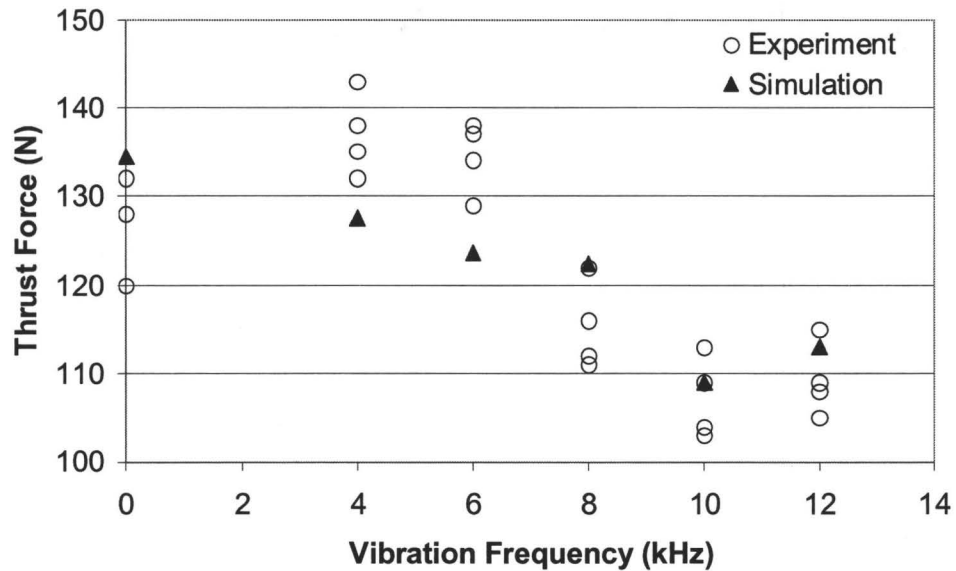


Figure 5.4.2. Simulations and experimental thrust force results for tests 13–18.



**Figure 5.4.3. Simulations and experimental thrust force results for tests 19–24.**

Figure 5.4.4–Figure 5.4.6 present the comparison between the mean value of the experimental thrust force measurements (averaged over each set of four tests) and simulation results with both the plowing force and strain rate-dependent shear strength models (simulation), without the plowing force model (w/o  $F_{pt}$ ), and without plowing force and shear strength models (w/o  $F_{pt}$  and  $\tau_i$ ), respectively. The comparisons show that including  $F_{pt}$  and  $\tau_i$  in the simulation generally improves the thrust force predictions. The plots also show that at higher vibration frequencies including  $\tau_i$  becomes more important. This is logical since increasing the vibration frequency increases the strain rate.

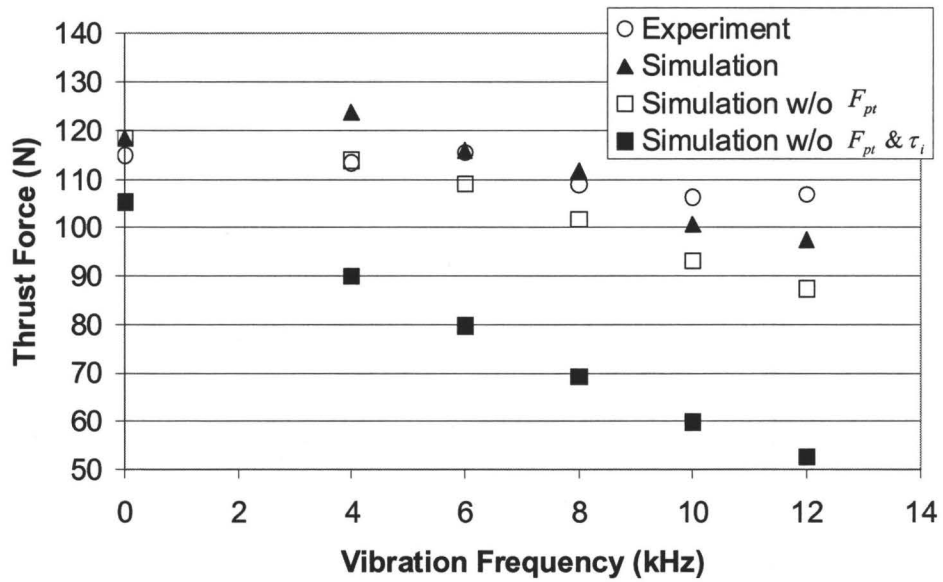


Figure 5.4.4. Different thrust force simulation results for tests 7–12.

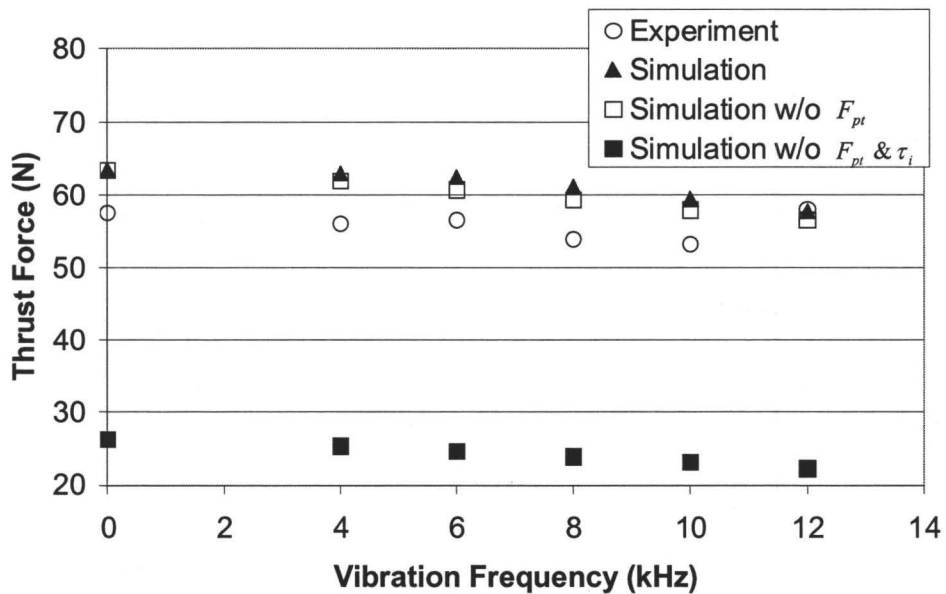


Figure 5.4.5. Different thrust force simulation results for tests 13–18.

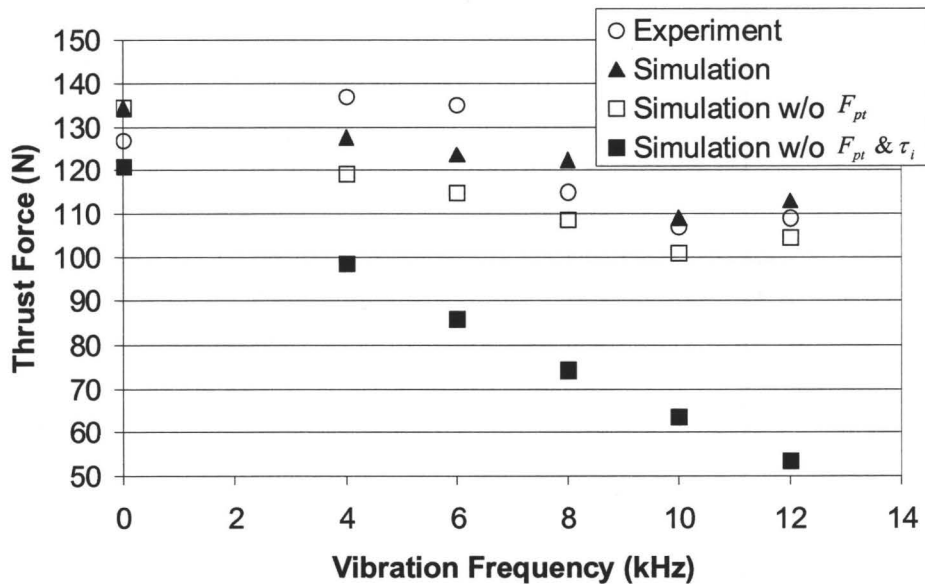


Figure 5.4.6. Different thrust force simulation results for tests 19–24.

## 5.5 BURR HEIGHT MODEL PREDICTION AND EXPERIMENTAL RESULTS

The calibrated model was also used to predict burr height for tests 7–24. These predictions were compared with the experimental measurements. Table 5.5.1 summarizes the comparison between the model predictions and the mean values of the experimental measurements.

Table 5.5.1. Comparison between model prediction and experimental measurements.

Test No.	Mean Burr Height (mm)	Model Prediction (mm)	Deviation (%)
7	0.114	0.130	-11.2
8	0.100	0.102	-1.8
9	0.092	0.097	-5.1
10	0.085	0.093	-8.2
11	0.104	0.092	11.5
12	0.111	0.097	12.3

13	0.097	0.091	6.1
14	0.076	0.083	-9.3
15	0.077	0.082	-7.2
16	0.063	0.080	-16.6
17	0.084	0.079	6.1
18	0.083	0.077	6.7
19	0.198	0.179	9.6
20	0.132	0.125	6.3
21	0.126	0.121	4.4
22	0.114	0.120	-5.5
23	0.137	0.124	9.5
24	0.138	0.158	-13.5

The experimental results and the comparison with the simulation results for burr height measurements are shown in Figure 5.5.1 to Figure 5.5.3. The solid data points represent simulation results and hollow circular data points represent experimental data. The maximum deviation of experimental results from simulations is  $\pm 16\%$ , and the mean values of the experimental burr height measurements fall within  $\pm 19\%$  of the simulation predictions. Since burr formation is a highly stochastic process, the large scattering of the experimental data is expected.

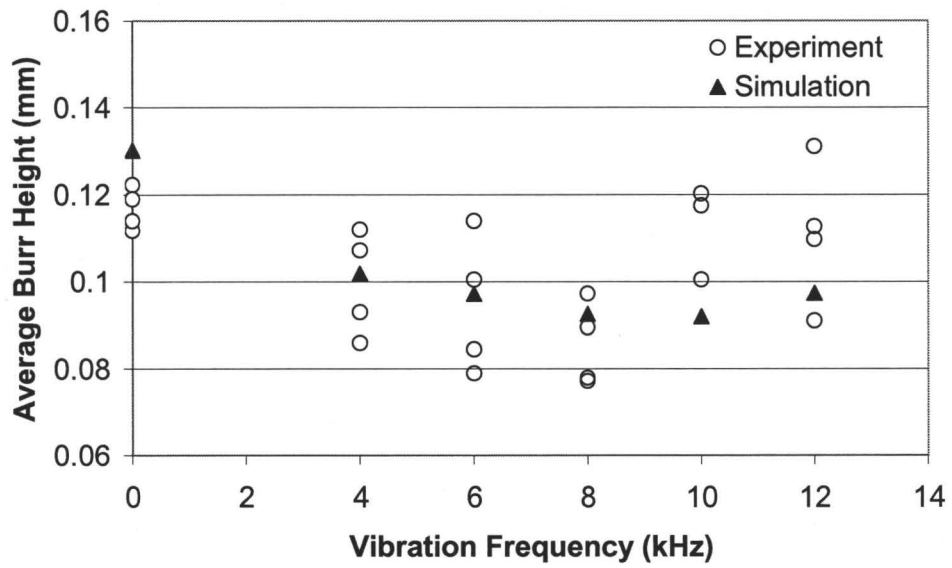


Figure 5.5.1. Simulations and experimental burr height results for tests 7–12.

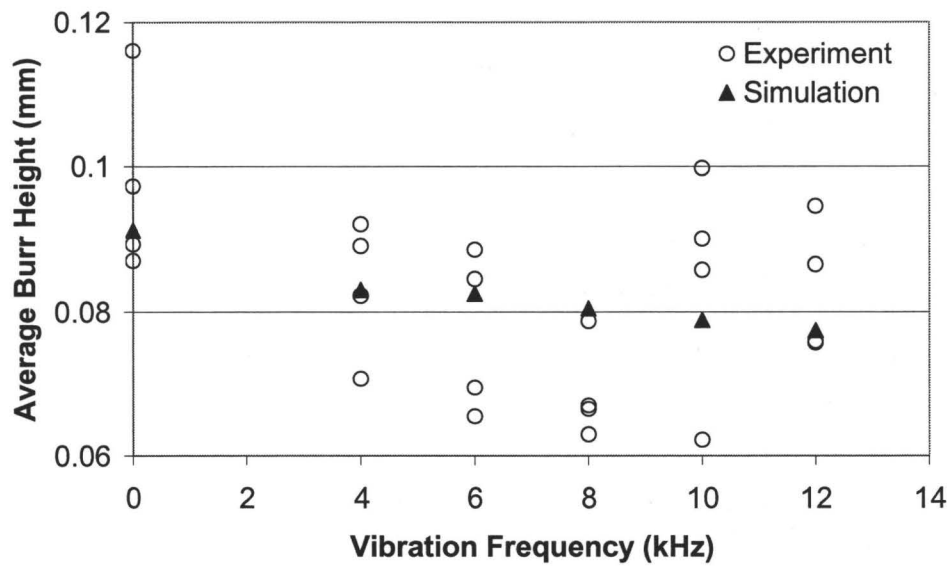
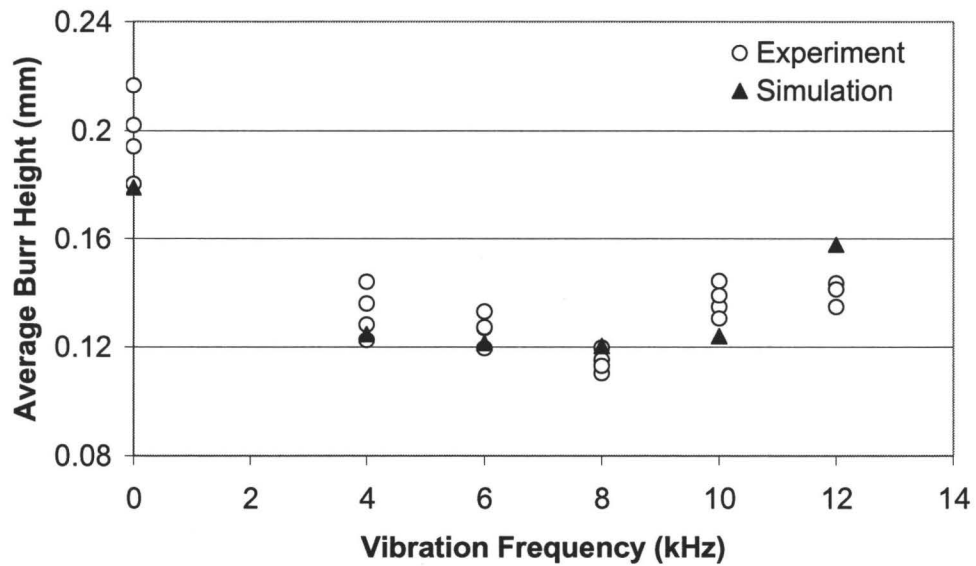


Figure 5.5.2. Simulations and experimental burr height results for tests 13–18.



**Figure 5.5.3. Simulations and experimental burr height results for tests 19–24.**

Figure 5.5.4 to Figure 5.5.6 present the comparison between the complete simulation results (labeled as *sim*); simulation results without the exclusively positive thrust forces (labeled as *w/o  $F_{th}^+$* ), i.e., including the negative values; simulation results without the exclusively positive thrust forces and the elastic spring back of materials (labeled as *w/o  $F_{th}^+$  &  $\varepsilon_e$* ); and the mean value of the experimental burr height measurements (labeled as *ave*) for tests 7–24. For conventional drilling (at 0 Hz vibration frequency), the results without  $F_{th}^+$  &  $\varepsilon_e$  were obtained by combining the model developed by Kim and Dornfeld [22] with the thrust force prediction equations presented in Section 2.4. The comparisons show that the modifications presented in this paper improve the accuracy of the simulation results for conventional drilling by up to 13%. They also demonstrate that these modifications are important in order to predict the burr height for VAD accurately. For example for test 16 the accuracy is improved by 35%.

Note that at low vibration frequencies (below 8 kHz in our studies), there are no negative thrust forces, and therefore the simulation results with and without  $F_{th}^+$  are the same.

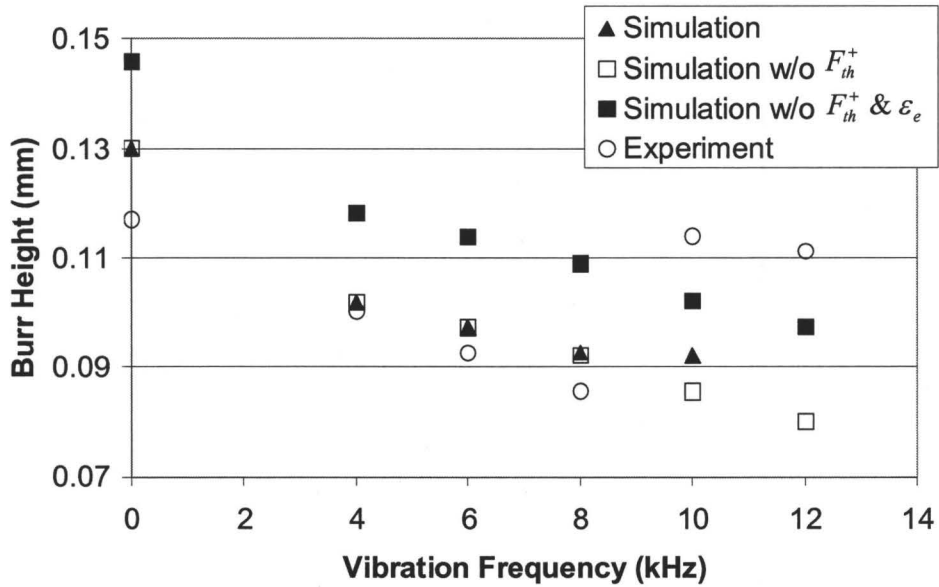


Figure 5.5.4. Different burr height simulation results of tests 7–12.

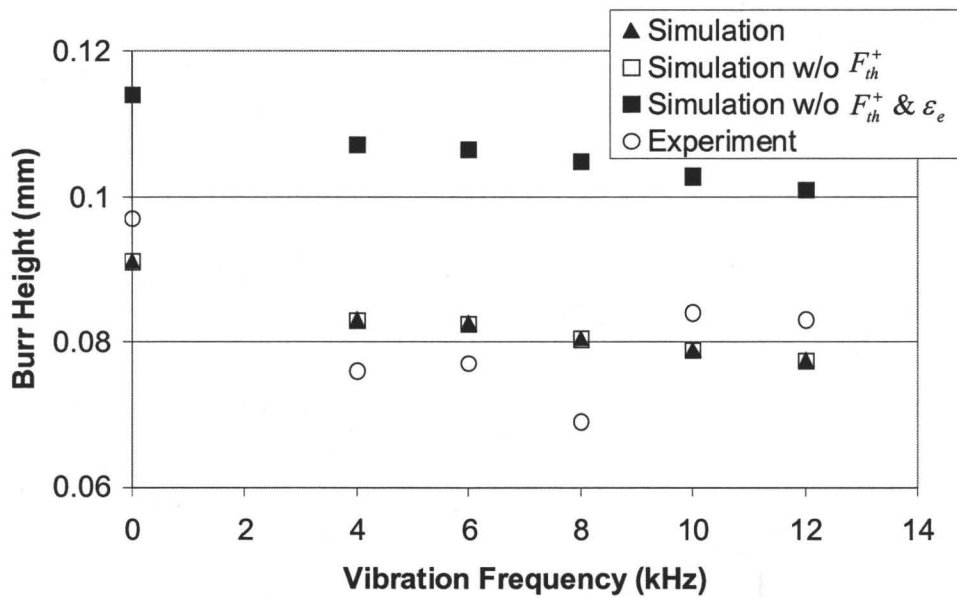


Figure 5.5.5. Different burr height simulation results of tests 13–18.

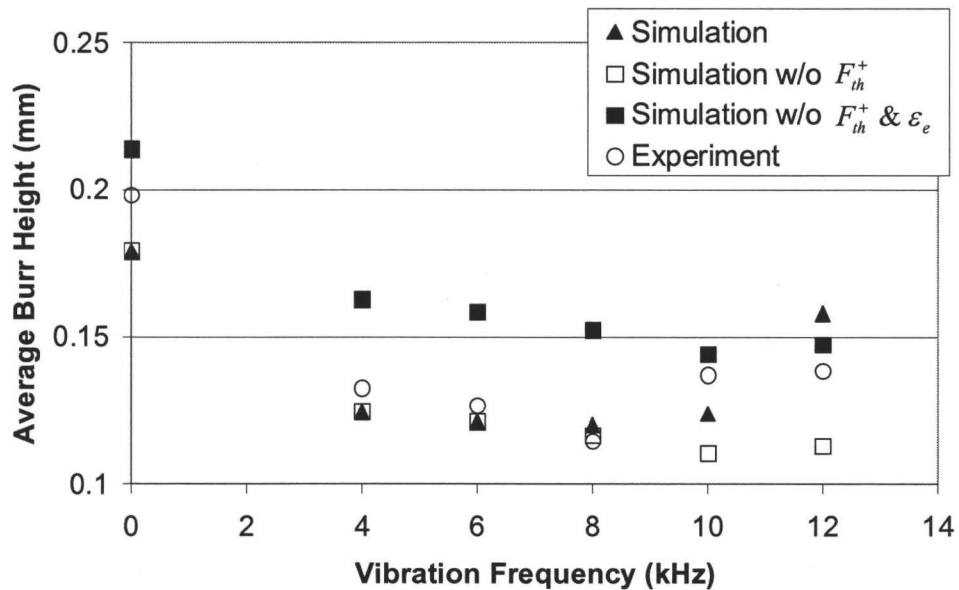


Figure 5.5.6. Different burr height simulation results of tests 19–24.

## 5.6 PREDICTING THE FAVOURABLE VIBRATION FREQUENCY

The program developed to determine the favourable vibration frequency that was presented in Section 4.2 was used to predict the favourable vibration frequency for the cutting conditions used in tests 7–24. The prediction was compared with the experimental results (Table 5.6.1) and showed consistency with experimental observation. Figures showing the relationship between  $\overline{W}_{t,i}$  and  $\overline{\eta}_d$  for cutting conditions 2 to 4 are presented in Appendix A.

**Table 5.6.1. Prediction of  $\bar{\eta}_d^*$  and  $f^*$ .**

Condition No.	$\bar{\eta}_d^*$	Predicted $f^*$ (Hz)	Experimental $f^*$ (Hz)
2	0.55	8575	$6000 < f^* < 8000$
3	0.22	8772	$6000 < f^* < 8000$
4	0.55	7902	$6000 < f^* < 8000$

## 5.7 CONCLUSIONS

The presented experimental results have shown that VAD has the potential to reduce both mean thrust force and burr height. Consistent with previous findings, poor choice of vibration conditions can increase thrust force and burr height, while a proper choice can provide significant reductions.

The proposed thrust force model presented in Chapter 3, which includes the variation of dynamic uncut chip thickness, the presence of plowing forces, and the variation of shear strength due to the changes in strain rate in VAD, has been used to predict the mean thrust force for the performed experiments. Comparisons between experimental results and model predictions have shown the accuracy of the developed model. The mean values of the experimental thrust forces for all tested conditions fall within  $\pm 13\%$  of the model predictions, and the worst case error is 18%. The comparisons also demonstrated the importance of modeling the plowing force and incorporating strain rate-dependent shear strength for producing accurate thrust force predictions.

The proposed burr height model that was presented in Chapter 4 was used to predict the mean burr height for the performed experiments. This model incorporated the

hypothesis that only the positive portion of the thrust force contributes to burr formation and included elastic spring back of the workpiece material to provide more accurate predictions. Comparisons between experimental results and model predictions have shown the accuracy of the developed model. The mean values of the experimental burr heights for all tested conditions for VAD fall within  $\pm 16\%$  of the model predictions, and the worst case error is 19%. Compared to Kim and Dornfeld's burr height model for conventional drilling, the proposed model improves the accuracy by up to 13% .

The rapid approach to determine the favourable vibration frequency presented in Section 4.2 showed consistent results with the experimental study. The presented method used simplified equations and reasonable approximations to simplify the mathematical calculations. The comparison with experimental results showed that this method is not only fast and simple but also provides an accurate prediction for the favourable vibration frequency.

## **CHAPTER 6**

# **COMBINED FREQUENCY VIBRATION ASSISTED DRILLING**

### **6.1 INTRODUCTION**

The concept of CFVAD has been described in Chapter 2. In this chapter, the data from 45 CFVAD experiments for aluminum 6061-T6 will be presented and discussed. The objectives of this experimental study are to demonstrate the effect of CFVAD in drilling aluminum, and to provide directions for future research.

### **6.2 CFVAD EXPERIMENTS**

The CFVAD experiments were conducted on a Makino MC56-5XA milling center. The cutting conditions were: 1000 RPM spindle speed and 0.1 mm/sec feedrate. The chosen low frequency and high frequency vibration amplitudes were 0.1 mm and 0.002 mm respectively, and the chosen vibration frequencies are summarized in Table 6.2.1. These conditions were chosen based on two factors: the maximum velocity of the drill generated by the low frequency vibration must be larger than the axial drill velocity generated by the drill feed in order to generate intermittent cutting; and the frequency

separation between low and high frequency must be within 1000 Hz. These factors are consistent with the characteristics of the vibration conditions for CFVAD reported in [36]. Note that the low frequency vibrations will be generated by the machine tool, and this limited the magnitude of the vibration frequency. Coelho *et al.* [58] reported that the maximum response time of a typical CNC machine axis is 25 ms. The minimum vibration period was chosen to be ten times the total response time, and therefore the maximum vibration frequency generated by the machine tool was 2 Hz. Nine new 3.18 mm finished TiN coated high speed steel twist drills were used to drill five 3.18 mm thick aluminum 6061-T6 workpieces for each of the vibration conditions, resulting in a total of 45 drilling tests. Drilling thrust forces were measured using a Kistler Type 9255B table dynamometer. The mean thrust force was obtained by finding the average over the five time-averaged thrust force values of each drilling test. Burr heights were measured using the same method as described in Chapter 5. The mean burr height was obtained by finding the average over the five averaged burr height values of each drilling test. The experimental measurements are summarized in Table 6.2.1.

**Table 6.2.1: CFVAD experimental results for the chosen vibration conditions.**

Low Frequency (Hz)	High Frequency (Hz)	Mean thrust force (N)	Mean burr height (mm)
0	0	92.9	0.35
0	200	79.25	0.44
0	1000	88.9	0.47
1	0	13.73	0.33
1	200	13.44	0.42
1	1000	8.66	0.43
2	0	29.12	0.49
2	200	35.84	0.55
2	1000	25.85	0.56

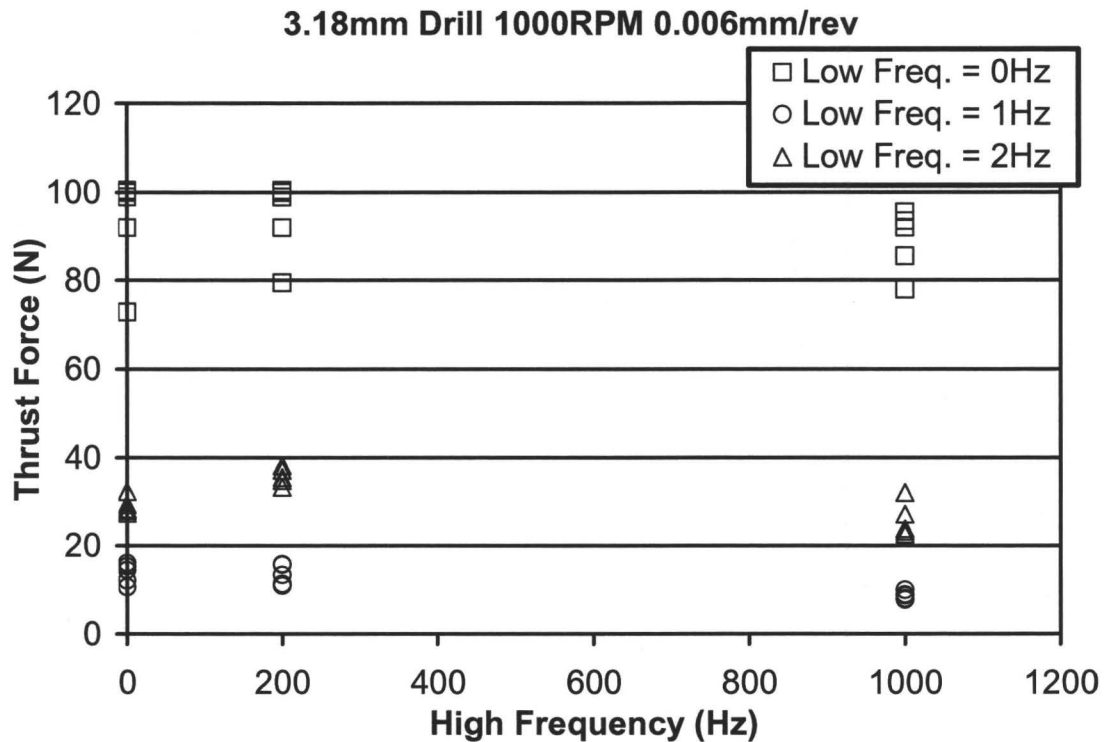


**Figure 6.2.1: Mean thrust force vs. high frequency vibration component for 45 CFVAD experiments.**

Figure 6.2.1 graphically shows the influence of the high and low frequency components on the thrust force. The three low frequency components are represented by different data points as shown. These experimental results show that CFVAD can reduce the mean thrust force. Among the chosen conditions, a combination of 1 Hz and 1000 Hz produced the lowest mean thrust force. The results also suggest that the effects of the two different vibration components are independent of each other. This means combining two different favourable vibration conditions together should result in further mean thrust force reduction than using single frequency vibration assistance. In this example, among the three chosen low frequency components, 1Hz was the favourable vibration frequency;

while 1000Hz was the favourable vibration frequency among the three chosen high frequency components. By combining 1Hz and 1000Hz, a further reduction in thrust force was achieved. One future research direction would be to further study the effects of CFVAD on thrust force.

Figure 6.2.2 shows the influence of the vibration components on the burr height. It appears that the low frequency vibration has an insignificant effect on the burr height. This finding is unexpected since the addition of low frequency vibration reduced the thrust force as shown above. One possible explanation is that the low frequency vibration amplitude is too large. From the simulation results presented in Chapter 5, the critical material thickness,  $t_c$ , falls below 0.1 mm. Therefore, the burr formation occurs within one cycle of the chosen low frequency vibration amplitude. Another future research direction would be to develop a suitable external low frequency vibration generator, and experimentally determine whether CFVAD at a lower amplitude would be beneficial for burr height reduction.

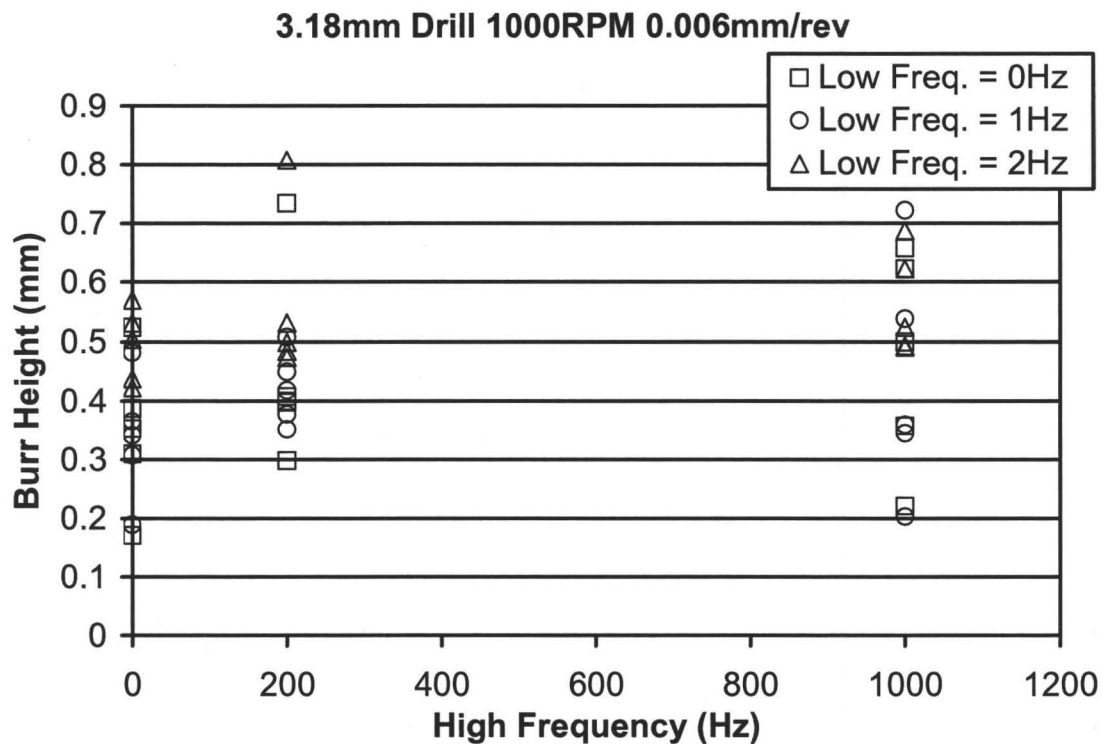


**Figure 6.2.2: Burr height vs. high frequency vibration component for 45 CFVAD experiments.**

### 6.3 CONCLUSIONS

CFVAD experimental results were presented and discussed in this chapter. The low frequency component was generated by the machine tool. This limited the low frequency vibration frequency and amplitude that could be applied. The data from 45 drilling experiments showed that the mean thrust force can be further reduced by adding a suitable low frequency vibration component to high frequency VAD. The influence of CFVAD on burr height was inconclusive. This was likely caused by the available low

frequency vibration amplitude being larger than  $t_c$ . This meant that the burr formation process was completed within one low frequency vibration cycle, and therefore the vibration had little or even no influence on the overall burr formation. Future research is necessary to extend CFVAD to the burr height reduction application.

## CHAPTER 7

### CONCLUSIONS AND RECOMMENDATIONS

#### 7.1 INTRODUCTION

This thesis presented the development of a thrust force and burr height model for VAD aluminum 6061-T6. It was found that to model the thrust force accurately, all significant governing factors of VAD must be modeled accurately. It was also found that only the positive portion of the thrust force is important for burr height predictions, and elastic spring back should be included to model burr height for the chosen material.

One hundred and twenty VAD experiments have been reported. Thirty experiments were used to calibrate the developed model, and ninety experiments were used to validate the accuracy of the developed model. The mean values of the experimental thrust force and burr height measurement falls within 7% and 10% of the model predictions respectively, with the corresponding worst case errors of 10% and 15%. An analytical method for rapidly predicting favourable vibration frequency has also been developed. The predictions are consistent with the experimental results. One journal paper has been published from the thrust force modeling research [59]. The burr height model has been published in a second journal paper [60].

Forty-five CFVAD experiments have been reported. The results showed that CFVAD can reduce thrust force, but the influence on burr height is inconclusive. Further research is necessary before the potential benefit of CFVAD can be concluded.

## 7.2 CONCLUSIONS

1. Comparison between experiments and simulation results prove that modeling all significant characteristics of VAD is important in order to accurately predict thrust force. The existing models only model the instantaneous uncut chip thickness. This is not sufficient to provide accurate thrust force predictions. It was found that modeling the shear strength of the material under different vibration conditions is important. A strain-rate dependent shear strength model is included in the new thrust force model. Experimental results prove that the strain-rate dependent shear strength model can improve the accuracy of the thrust force model by up to 33%.
2. It was found that with the presence of vibrations, the drill face can be plowing on the material under the drill. The corresponding plowing force is a function of the displaced volume of workpiece material by the plowing actions of the drill. A plowing model is included in the thrust force model to improve the predictions of the model. Experimental results demonstrate that the plowing force model further improves the accuracy of the thrust force model by up to 9%.
3. It was found that while burr height is dependent on the thrust force, in VAD thrust force can reach negative values when the vibration frequency and/or amplitude is high. These negative thrust forces have an insignificant influence on burr height.

Comparison between model predictions and experimental results proves that including negative values of thrust force will wrongly predict burr height (when the vibration frequency is high enough such that negative thrust force exists), while using only the positive portion of the thrust force significantly improves the burr height predictions at high vibration frequencies.

4. The burr height model presented by Kim and Dornfeld [29] does not account for the elastic spring back of the workpiece material after final burr fracture occurs. It was found that this model is not appropriate for aluminum 6061-T6, which is a ductile metal. An elastic spring back model is included in the burr height model. Experimental results prove that the current model improves the accuracy of Kim and Dornfeld's model by up to 13%.
5. Experimental results showed that a favourable vibration frequency for burr height reduction exists. An analytical method that rapidly predicts this frequency was presented. This method determines the frequency that minimizes the normalized work done. It is proposed that when the normalized work done is minimized, the burr height is also minimized. The predictions obtained using this method are consistent with the experimental results.
6. CFVAD experiments have been reported. It was found that the influences of the low and high frequency vibrations on thrust forces are independent of each other. It is hypothesized that by combining two favourable vibration conditions together thrust force can be further reduced.

7. The CFVAD experimental study on burr height reduction is inconclusive. The available low frequency vibration amplitude is higher than the critical material thickness, which is a crucial factor for burr height. The burr formation process is completed in less than one low frequency vibration cycle, and therefore the low frequency vibration assistance has insignificant influence on burr height.

### **7.3 RECOMMENDATIONS FOR FUTURE WORK**

The following future work is suggested:

- Extend the current experimental investigations to 30 kHz and 0.010 mm amplitude to verify the presented model up to typical ultrasonic vibration frequency and amplitude range.
- Extend the CFVAD experiments to demonstrate the effect of combining two favourable vibration conditions on thrust force, and compare the results of CFVAD and VAD.
- Develop a CFVAD workpiece holder that generates larger low frequency vibration amplitude and investigate the potential benefit of CFVAD on burr height reduction.
- Extend the current thrust force and burr height model to include CFVAD.
- Extend the model to include the thermal aspects.

## REFERENCE

- [1] L. K. Gillespie, “Deburring precision miniature parts”, *Precision Engineering*, vol. 1, no. 4, pp. 189-198, 1979.
- [2] T. Kito, R. Tanaka, A. Hosokawa, T. Ueda, and T. Furumoto, “Prevention of burr formation in face milling of carbon steel by laser hardening”, *Key Engineering Materials*, vol. 407-408, pp. 672-675, 2009.
- [3] Z. Yang, Q. Tan, and L. Wang, “Principal of precision micro-drilling with axial vibration of low frequency”, *International Journal of Production Research*, vol. 40, no. 6, pp. 1421-1427, 2002.
- [4] X. Wang, L. J. Wang, and J. P. Tao, “Investigation on thrust in vibration drilling of fiber-reinforced plastics”, *Journal of Materials Processing Technology*, vol. 148, pp. 239-244, 2004.
- [5] O. Ohishi, H. Onikura, A. Hata, and K. Yamamoto, “Fabrication of micro flat drills by precision grinding and drilling into duralumin and stainless steel with ultrasonic vibration”, *International Journal of JSME*, vol. 47, no. 1, series C, pp. 117-122, 2004.
- [6] R. Neugebauer and A. Stoll, “Ultrasonic application in drilling”, *Journal of Materials Processing Technology*, vol. 149, pp. 633-639, 2004.
- [7] Y. Altintas, *Manufacturing Automation*, Cambridge: Cambridge University Press, 2000.

- [8] E. M. Trent and P. K. Wright, *Metal Cutting*, Oxford: Butterworth Heinemann, 2000.
- [9] S. Wiriycosol and E. J. A. Armarego, “Thrust and torque prediction in drilling from a cutting mechanics approach”, *Annals of CIRP*, vol. 28, no. 1, pp. 87-91, 1979.
- [10] E. J. A. Armarego and J. D. Wright, “Predictive models of drilling thrust and torque – a comparison of three flank configurations”, *Annals of CIRP*, vol. 33, no. 1, pp. 5-10, 1984.
- [11] A. R. Watson, “Geometry of drill elements”, *International Journal of Machine Tools Design and Research*, vol. 25, no. 3, pp. 209-227, 1985.
- [12] A. R. Watson, “Drilling model for cutting lip and chisel edge and comparison of experimental and predicted results. I – initial cutting lip model”, *International Journal of Machine Tools Design and Research*, vol. 25, no. 4, pp. 347-365, 1985.
- [13] M. Elhachimi, S. Torbaty, and P. Joyot, “Mechanical modeling of high speed drilling. 1: Predicting torque and thrust”, *International Journal of Machine Tools and Manufacture*, vo. 39, pp. 553-568, 1999.
- [14] M. Elhachimi, S. Torbaty, and P. Joyot, “Mechanical modeling of high speed drilling. 2: Predicted and experimental results”, *International Journal of Machine Tools and Manufacture*, vol. 39, pp. 569-581, 1999.
- [15] L. K. Gillespie and P. T. Blotter, “The formation and properties of machining burrs”, *Transactions of the ASME, Journal of Engineering for Industry*, pp. 66-74, February 1976.

- [16] D. A. Dornfeld and S. L. Ko, “A study on burr formation mechanism”, *Transactions of the ASME, Journal of Engineering Materials and Technology*, vol. 113, pp. 75-87, 1991.
- [17] D. A. Dornfeld, J. S. Kim, H. Dechow, J. Hewson, and L. J. Chen, “Drilling burr formation in titanium alloy Ti-6Al-4V”, *Annals of CIRP*, vol. 48, pp. 73-76, 1999.
- [18] D. A. Dornfeld and Y. B. Guo, “Finite element modeling of burr formation process in drilling 304 stainless steel”, *Transactions of the ASME, Journal of Manufacturing Science and Engineering*, vol. 122, pp. 612-619, 2000.
- [19] D. A. Dornfeld and Y. B. Guo, “Finite element analysis of drilling burr minimization with a backup material”, *Transactions of NAMRI/SME*, vol. XXVI, pp. 207-212, 1998.
- [20] D. A. Dornfeld and J. M. Stein, “Burr formation in drilling miniature holes”, *Annals of CIRP*, vol. 46, pp. 63-66, 1997.
- [21] K. L. Saunders Lauderbaugh and C. A. Mauch, “An exit burr model for drilling of metals”, *Transactions of ASME, Journal of Manufacturing Science and Engineering*, vol. 123, pp. 562-566, 2001.
- [22] J. Kim, D. A. Dornfeld, “Development of an analytical model for drilling burr formation in ductile materials”, *Transactions of ASME, Journal of Engineering Materials and Technology*, vol. 124, pp. 192-198, 2002.
- [23] J. Ramkumar, S. K. Malhotra, and R. Krishnamurthy, “Effect of workpiece vibration on drilling of GFRP laminates”, *Journal of Materials Processing Technology*, vol. 152, pp. 329-332, 2004.

- [24] L. Zhang, L. Wang, and X. Wang, “Study on vibration drilling of fiber reinforced plastics with hybrid variation parameters method”, *Composites: Part 1*, vol. 34, pp. 237-244, 2003.
- [25] Z. J. Li, M. S. Hong, L. J. Wang, H. W. Zhao, H. Su, and Y. L. Wei, “Machining accuracy analysis for step multi-element varying parameter vibration drilling of laminated composite materials”, *International Journal of Advance Manufacturing Technology*, vol. 21, pp. 760-768, 2003.
- [26] H. Weber, J. Herberger, R. Pilz, and T. H. Karl-Marx-Stadt T.H., “Turning of machinable glass ceramics with an ultrasonically vibrated tool”, *Annals of CIRP*, vol. 33, no. 1, pp. 85-87, 1984.
- [27] H. Takemaya and S. Kato, “Burrless drilling by means of ultrasonic assistance”, *Annals of CIRP*, vol. 40, no. 1, pp. 83-86, 1991.
- [28] T. Moriwaki, E. Shamoto, and K. Inoue, “Ultraprecision ductile cutting of glass by applying ultrasonic vibration”, *Annals of CIRP*, vol. 41, no. 1, pp. 141-144, 1992.
- [29] A. V. Mitrofanov, V. I. Babitsky, and V. V. Silberschmidt, “Finite element simulations of ultrasonically assisted turning”, *Computational Materials Science*, vol. 28, pp. 645-653, 2003.
- [30] A. V. Mitrofanov, V. I. Babitsky, and V. V. Silberschmidt, “Finite element analysis of ultrasonically assisted turning of Inconel 718”, *Journal of Materials Processing Technology*, vol. 153-154, pp. 233-239, 2004.

- [31] V. I. Babitsky, A. V. Mitrofanov, and V. V. Silberschmidt, “Ultrasonically assisted turning of aviation materials: simulations and experimental study”, *Ultrasonics*, vol. 42, pp. 81-86, 2004.
- [32] V. I. Babitsky, A. N. Kalashnikov, A. Meadows, and A. A. H. P. Wijesundara, “Ultrasonically assisted turning of aviation materials”, *Journal of Materials Processing Technology*, vol. 132, pp.157-167, 2003.
- [33] S. S. F. Chang, “Ultrasonic assisted drilling”, M.A.Sc. Thesis, McMaster University, Hamilton, ON, Canada, 2003.
- [34] S. S. F. Chang and G. M. Bone, “Ultrasonic assisted drilling”, in *FAIM Conference*, 2004, pp. 595-602.
- [35] S. S. F. Chang and G. M. Bone, “Burr size reduction in drilling by ultrasonic assistance”, *Robotics and Computer-Integrated Manufacturing*, vol. 21, pp. 442-450, 2005.
- [36] K. Ishikawa, H. Suwabe, T. Nishide and M. Uneda, “A study on combined vibration drilling by ultrasonic and low-frequency vibrations for hard and brittle materials”, *Precision Engineering*, vol. 22, pp. 196-205, 1998.
- [37] E. Shamoto and T. Moriwaki, “Study on elliptical vibration cutting”, *Annals of CIRP*, vol. 43, no. 1, pp. 35-38, 1994.
- [38] T. Moriwaki and E. Shamoto, “Ultrasonic elliptical vibration cutting”, *Annals of CIRP*, vol. 44, no. 1, pp. 31-34, 1995.
- [39] L. B. Zhang, L. J. Wang, X. Y. Liu, H. W. Zhao, X. Wang, and H. Y. Luo, “Mechanical model for predicting thrust and torque in vibration drilling fibre-

- reinforced composite materials”, *International Journal of Machine Tools and Manufacture*, vol. 41, pp. 641-657, 2001.
- [40] J. C. Roukema and Y. Altintas, “Generalized modeling of drilling vibrations. Part I: time domain model of drilling kinematics, dynamics and hole formation”, *International Journal of Machine Tools and Manufacture*, vol. 47 pp. 1455-1473, 2007.
- [41] J. C. Roukema and Y. Altintas, “Generalized modeling of drilling vibrations. Part II: chatter stability in frequency domain”, *International Journal of Machine Tools and Manufacture*, vol. 47 pp. 1474-1485, 2007.
- [42] L. P. Wang, L. J. Wang, and Z. J. Yang, “Prediction and computer simulation of dynamics thrust and torque in vibration drilling”, in *Proceedings of the Institution of Mechanical Engineer*, vol. 212B, pp. 489-497, 1998.
- [43] E. Budak and Y. Altintas, “Analytical prediction of chatter stability in milling – part 1: general formulation”, *Journal of Dynamic Systems, Measurements and Control*, vol. 120, pp. 22-30, 1998.
- [44] E. Budak and Y. Altintas, “Analytical prediction of chatter stability in milling – part 2: general formulation to common milling systems”, *Journal of Dynamic Systems, Measurements and Control*, vol. 120, pp. 31-36, 1998.
- [45] H. Li and X. Li, “Modeling and simulation of chatter in milling using a predictive force model”, *International Journal of Machine Tools and Manufacture*, vol. 40, pp. 2047-2071, 2000.

- [46] J. C. Roukema and Y. Altintas, “Time domain simulation of torsional-axial vibrations in drilling”, *International Journal of Machine Tools and Manufacture*, vol. 46, pp. 2073-2085, 2006.
- [47] D. W. Wu, “A new approach of formulating the transfer function for dynamic cutting process”, *Transactions of the ASME, Journal of Engineering for Industry*, vol. 111, pp. 37-47, 1989.
- [48] F. Ismail, M. A. Elbestawi, R. Du, and K. Urbasik, “Generation of milled surfaces including tool dynamics and wear”, *Transactions of the ASME, Journal of Engineering for Industry*, vol. 115, pp. 245-252, 1993.
- [49] N. K. Chandiramani and T. Pothala, “Dynamics of 2-dof regenerative chatter during turning”, *Journal of Sound and Vibration*, vol. 290, pp. 448-464, 2006.
- [50] A. Moufki, A. Devillez, M. Segreti, and D. Dudzinski, “A semi-analytical model of non-linear vibrations in orthogonal cutting and experimental validation”, *International Journal of Machine Tools and Manufacture*, vol. 46, pp. 436-449, 2006.
- [51] P. Lee and Y. Altintas, “Prediction of ball-end milling forces from orthogonal cutting data”, *International Journal of Machine Tools and Manufacture*, vol. 36, pp. 1059-1072, 1996.
- [52] J. Wang and C. M. Zheung, “An analytical force model with shearing and ploughing mechanisms for end milling”, *International Journal of Machine Tools and Manufacture*, vol. 42 pp. 761-771, 2002.

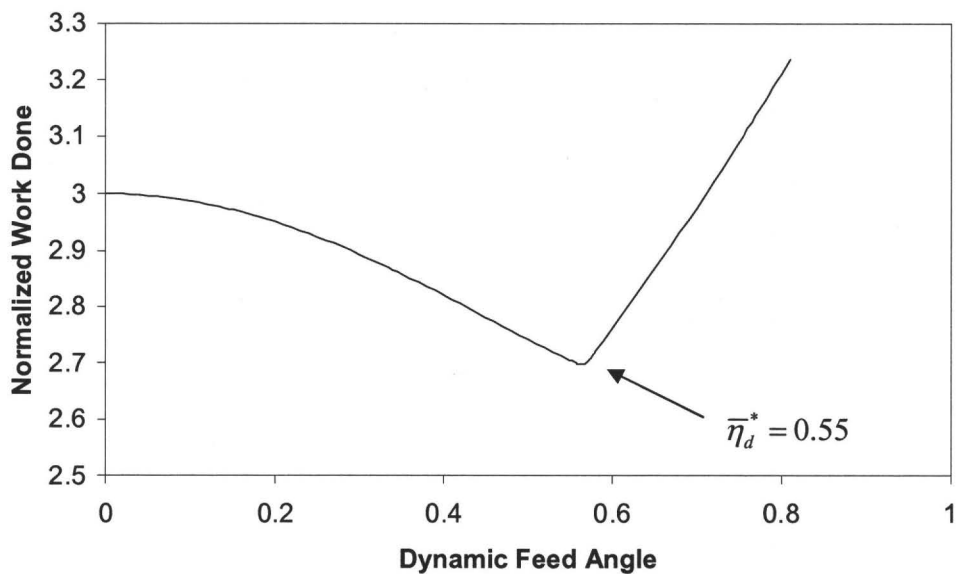
- [53] E. H. Lee and B. W. Shaffer, “The theory of plasticity applied to a problem of machining”, *Transactions of the ASME, Journal of Applied Mechanics*, vol. 18, pp. 405-413, 1951.
- [54] R. A. Williams, “A study of drilling process”, *Transactions of the ASME, Journal of Engineering for Industry*, vol. 96, pp. 1207-1215, 1974.
- [55] G. R. Johnson and W. H. Cook, “A constitutive model and data for metals subjected to large strains, high strain rates, and high temperature”, in *Proceedings of the 7<sup>th</sup> International Symposium on Ballistics*, Hague, Netherlands, 1983.
- [56] Y. B. Guo, “An integral method to determine the mechanical behavior of materials in metal cutting”, *Journal of Materials Processing Technology*, vol. 142, pp. 72-81, 2003.
- [57] A. Chamanfar and R. Mahumudi, “Compensation of elastic strains in the determination of plastic strain ratio (R) in sheet metals”, *Material Science and Engineering A*, vol. 397, pp. 153-156, 2005.
- [58] R. T. Coelho, A. Fagali de Souza, A. R. Roger, A. M. Y. Rigatti, and A. A. Ribeiro, “Mechanistic approach to predict real machining time for milling free-form geometries applying high feed rate”, *International Journal of Advanced Manufacturing Technology*, published online, July 2009.
- [59] S. S. F. Chang and G. M. Bone, “Thrust force model for vibration assisted drilling of aluminum 6061-T6”, accepted in final form for *International Journal of Machine Tools and Manufacture*, July 26, 2009.

- [60] S. S. F. Chang and G. M. Bone, “Burr height model for vibration assisted drilling of aluminum 6061-T6”, accepted in final form for *Precision Engineering*, Sept. 11, 2009.

## APPENDIX A

Figures of  $\bar{W}_{t,i}$  vs  $\eta_d$  for cutting conditions 2 to 4.

**Normalized Work Done for Condition 2**



**Normalized Work Done for Condition 3**

